INTERACTIONS OF RENAL CLEARABLE GOLD NANOPARTICLES WITH THE KIDNEYS *IN VITRO* AND *IN VIVO*

by

Jing Xu

APPROVED BY SUPERVISORY COMMITTEE:

_____

Dr. Jie Zheng, Chair

_____

Dr. Bruce E. Gnade

_____

Dr. Jiyong Lee

_____

Dr. Steven O. Nielsen

_____

Dr. Leonidas Bleris

This work is dedicated to my beloved family and friends

INTERACTIONS OF RENAL CLEARABLE GOLD NANOPARTICLES WITH THE KIDNEYS *IN VITRO* AND *IN VIVO*

by

JING XU, BS

DISSERTATION

Presented to the Faculty of

The University of Texas at Dallas

in Partial Fulfillment

of the Requirements

for the Degree of

DOCTOR OF PHILOSOPHY IN

CHEMISTRY

THE UNIVERSITY OF TEXAS AT DALLAS

August 2018

ACKNOWLEDGMENTS

I would like to express my sincere gratitude to my supervisor, Dr. Jie Zheng, for his support and guidance throughout the whole doctoral program. His extreme passion and dedication towards science as well as his knowledge of inorganic chemistry and nanoscience has always inspired me. Dr. Jie Zheng is also an amazing mentor in life. His continual encouragement has helped me overcome so many difficulties encountered in my graduate life. I would also like to express my sincere gratitude to Dr. Mengxiao Yu for her close advising on my research projects and writing skill. Her strictness, patience and passion for science has impacted me profoundly. Dr. Mengxiao Yu is also my mentor and best friend in life. Her caring and compassionate personality has always moved me. I am also grateful to Dr. Bruce E. Gnade, Dr. Steven O. Nielsen, Dr. Jiyong Lee and Dr. Leonidas Bleris for their advice and support in my committee meetings. Special thanks to the guidance and patience provided by Dr. Bruce E. Gnade, Dr. Steven O. Nielsen and Dr. Jiyong Lee in my first committee meeting.

I am very much indebted to the members of the Zheng Lab for creating such an inspiring and delightful environment. Special thanks to Xuhui (Louis) Ning who has been working with me for the longest time, for always offering me help unconditionally in work and in life. A lot of thanks to Dr. Shaoheng Tang, who is like a big brother taking good care of us. I am also very grateful to Chuanqi Peng whose insight and creativity has contributed remarkably to my research projects. I would also like to thank Yingyu Huang who has shared a lot of great ideas with me. Thanks to Bujie Du and Xingya Jiang for providing valuable suggestions on my research. I am also grateful to Qinhan Zhou for all the help during the teaching assignment. Thanks to Siqing Li for giving me a precious opportunity to be a graduate mentor. I am also very grateful to my former undergraduate

student Phoebe Carter who contributed tremendously to my research projects. I really miss the time we spent together working and chatting in the lab. Thanks to my former colleague Shasha Sun, who is also a good friend. I really appreciate the help you offered during the early years of my graduate life.

I want to thank Dr. Jer-Tsong Hsieh, Elizabeth Hernandez and Andrew Dang from the Department of Urology, The University of Texas Southwestern Medical Center, for their incredible work on tissue processing and biochemistry analysis. Thanks to Dr. Payal Kapur from the Department of Pathology, The University of Texas Southwestern Medical Center, for her histological analysis and detailed explanation. I would also like to thank Chance Nowak and Dr. Leonidas Bleris for their impressive work on *in vitro* apoptosis assay and data analysis.

I also want to send my deep gratitude to the faculty and staff in the Department of Chemistry and Biochemistry. Special thanks to Dr. Hien Nguyen, Betty Maldonado, Linda Heard and Kelli Lewis for being so helpful.

At the end, I would like to thank my husband, Jia Du. You are the best I can ask for. I sincerely thank my parents, Ruixia Wang and Ruiguo Xu, for their unconditional love and support.

June 2018

INTERACTIONS OF RENAL CLEARABLE GOLD NANOPARTICLES WITH THE KIDNEYS *IN VITRO* AND *IN VIVO*

Jing Xu, PhD
The University of Texas at Dallas, 2018

Supervising Professor: Dr. Jie Zheng

The emergence of renal clearable inorganic nanoparticles (NPs) offers a great opportunity to address the health concern raised by nonspecific accumulation of conventional inorganic NPs in the macrophage system, mostly in the liver and spleen. In recent decades, we have dedicated a remarkable amount of research in developing renal clearable gold nanoparticles (AuNPs) and investigating their biointeractions. Our group discovered that glutathione-coated renal clearable AuNPs (GS-AuNPs) can be efficiently excreted through the urinary system resulting in significantly reduced accumulation in the liver and spleen. By integrating the near-infrared fluorescence, GS-AuNPs can sensitively probe kidney clearance kinetics and indicate renal dysfunction. Future clinical translation requires a fundamental understanding of nano-bio interactions in the kidneys and the biocompatibility of GS-AuNPs.

In this dissertation, Chapter 1 covers the status of renal clearable inorganic NPs and the current understanding of their biointeractions in the kidneys. Chapter 2 describes using X-ray imaging to visualize the transport of GS-AuNPs in the kidney components under both normal and pathological conditions. The unique deposition of GS-AuNPs in the diseased kidney offers a great chance to

diagnose renal injury noninvasively. Chapter 3 focuses on the blood transport and biocompatibility of GS-AuNPs. The dose effect on the blood transport and renal clearance efficiency of GS-AuNPs is unraveled which results in high biocompatibility. Chapter 4 describes an *in vitro* study on the surface-ligand-density effect on interactions between GS-AuNPs and human kidney proximal tubular cells. The results demonstrate precise responses of proximal tubular cells to GS-AuNPs with different ligand densities in membrane affinity, cytotoxicity and the mechanism of cell death. Finally, a summary of the obtained understanding and future perspective are presented in Chapter 5.

TABLE OF CONTENTS

LIST OF FIGURES

LIST OF TABLES

LIST OF ABBREVIATIONS

AF	Alexa-fluor Annexin V
ALB	Albumin
ALP	Alkaline phosphates
ALT	Alanine transaminase
AST	Aspartate transaminase
AUC	Area under the curve
AuNPs	Gold nanoparticles
B	Bladder
BUN	Blood urea nitrogen
CHOL	Cholesterol
CL	Plasma clearance
C&M	Cortex and medulla
DM	Diatrizoate meglumine
EPR	Enhanced permeability and retention
FTIR	Fourier transform-infrared
GFM	Glomerular filtration membrane
GSH	L-reduced glutathione
GS-AgNPs	Glutathione-coated silver nanoparticles
GS-AuNPs	Glutathione-coated gold nanoparticles
$HAuCl_4$	Hydrogen tetrachloroaurate
HK-2	Human kidney proximal tubular cells

ICP-AES	Inductively coupled plasma atomic emission spectrocopy
ICP-MS	Inductively coupled plasma mass spectrometry
ID	Injection dose
KFT	Kidney filtration threshold
LK	Left kidney
LP	Long-pass
MRI	Magnetic resonance imaging
MTD	Maximal tolerated dose
MTT	(3-(4,5-Dimethylthiazol-2-yl)-2,5-Diphenyltetrazolium Bromide)
M ± SD	Mean ± standard deviation
NOAEL	No-observed-adverse-effect-level
NPs	Nanoparticles
ns	No significant difference
OATs	Organic anion transporters
P	Pelvis
PBS	Phosphate-buffered saline
PI	Propidium iodine
PK	Pharmacokinetics
PS	Phosphatidylserine
p.i.	Post injection
QDs	Quantum dots
RK	Right kidney

Rep	Representative
ROI	Region of interest
RPMI	Roswell Park Memorial Institute medium
sCr	Serum creatinine
TBIL	Total bilirubin
TEM	Transmission electron microscopy
TG	Triglycerides
TP	Total protein
TXDCs	Time-dependent X-ray density curves
UUO	Unilateral ureter obstruction
V_d	Volume of distribution
X.D.	X-ray Density
%ID	Percentage injection dose
%ID/g	Percentage injection dose per gram
%RRF	Relative renal function

CHAPTER 1

BIOINTERACTIONS OF RENAL CLEARABLE INORGANIC NANOPARTICLES IN THE KIDNEYS

Author - Jing Xu

Department of Chemistry and Biochemistry, BE 26

The University of Texas at Dallas

800 W. Campbell Rd., Richardson, TX 75080 (USA)

Abstract

The development of renal clearable inorganic nanoparticles (NPs) is believed to pave the way for future clinical translation of inorganic nanomedicine as it offers an opportunity to address the biosafety concern of nonbiodegradable NPs with long-term body accumulation. However, the dramatically increased exposure of the kidneys to NPs raises questions regarding the kidney processing and tolerance of renal clearable inorganic NPs, to which the answers would provide fundamental knowledge on the biological fate of renal clearable inorganic NPs and facilitate their safe clinical use. In this chapter, we summarize the findings on transport behavior, biocompatibility and cell-NP interactions of renal clearable inorganic NPs in the kidneys to offer a general picture on this research topic.

1.1 Introduction

Inorganic nanoparticles (NPs) have been discovered with remarkable biomedical potential owing to their tunable properties, strong signal output and long blood retention that small molecules cannot provide.[1] There are tremendous examples of inorganic NPs developed as imaging probes,[2] drug delivery systems[1c, 3] and even therapeutic agents.[4] However, their nonbiodegradable hard-material component and long-term accumulation in the macrophage system (e.g., the liver and spleen) raise a concern of biological safety for future clinical translation.[5] The development of renal clearable inorganic NPs offers a great opportunity to resolve this dilemma. By reducing the size below the kidney filtration threshold (<6 nm) and minimizing protein adsorption with antifouling coatings, the majority of the NPs can be excreted through the urinary system within a reasonable time-frame, instead of being retained in the macrophage system for months to years, or being slowly excreted through the hepatobiliary route for weeks to months.[6] So far, researchers have developed renal clearable quantum dots,[7] silica NPs,[8] gold NPs,[9] carbon dots,[10] etc. and explored their application in biomedical imaging and cancer targeting with enhanced biocompatibility. Furthermore, due to the exponentially increased clearance within a short time period, renal clearable gold NPs are capable of serving as contrast agents for kidney function evaluation with anatomical resolution, which further broadens the applications of inorganic nanomedicine.[11]

In addition to putting emphasis on developing applications, investigating the biointeractions of renal clearable NPs in the kidneys has attracted increasing attention. Generally, the kidneys process 50-75% of intravenously injected NPs within 24 h.[7-8, 9] This heavy workload demands a comprehensive investigation on the processing and tolerance of NPs in the kidneys so as to predict

and minimize the potential harm induced during the NP exposure. Besides, understanding cellular deposition and NP-cell interaction of renal clearable NPs is critical to address the long-term toxicity. In this chapter, we will summarize our most recent understanding of the transport behavior, biocompatibility and NP-cell interactions of renal clearable inorganic NPs.

1.2 Kidney anatomy and renal clearance of NPs

The kidneys, as one of the essential detoxification organs in the body system, regulate the plasma homeostasis by passively filtering out the waste products. Generally, a kidney is defined with three major regions, renal cortex, medulla and pelvis. Nephrons, the basic structural and functional units of a kidney, span the cortex and medulla. A nephron consists of a renal corpuscle and a renal tubule. The renal corpuscle is basically a capillary tuft, named glomerulus, incorporated by the beginning part of the renal tubule, Bowman's capsule.[12] The tubular segments extending from Bowman's capsule are proximal tubule, loop of Henle, distal tubule and collecting duct (Figure 1.1). Every heartbeat, 20% of the cardiac output reaches the kidneys and get processed in nephrons. Briefly, metabolic waste, some plasma solutes and excessive water are filtered from the glomeruli into the Bowman's capsules; the filtrate is further transported between tubular segments where reabsorption and secretion of specific solutes occur.

Kidney filtration, the dominant process in the renal excretion of nanostructures, is assisted by the glomerular filtration membrane (GFM) whose structures are adapted to the filtration function. The GFM consists of three layers, the endothelial monolayer, the basement membrane and the epithelial layer. Different from the small intracellular cleft (20 nm) in an ordinary capillary membrane, 70-90 nm fenestra are constructed on the glomerular endothelium. The basement

membrane has a pore size of 2-8 nm. The epithelial cells in the GFM are discontinuous and develop footlike extensions (podocyte) with 4-11 nm slit pores (Figure 1.2). These structural features facilitate the percolation of a tremendous amount of small molecule solutes, however, set a filtration size threshold of 6 nm for natural macromolecules and engineered NPs. On the other hand, the GFM is negatively charged owing to the presence of negatively charged components (e.g., heparan sulfate proteoglycan in the endothelial glycocalyx, the podocytes glycocalyx); therefore, glomerular filtration of negatively charged natural macromolecules is slower than that of their positively charged counterparts.[6a, 12-13]

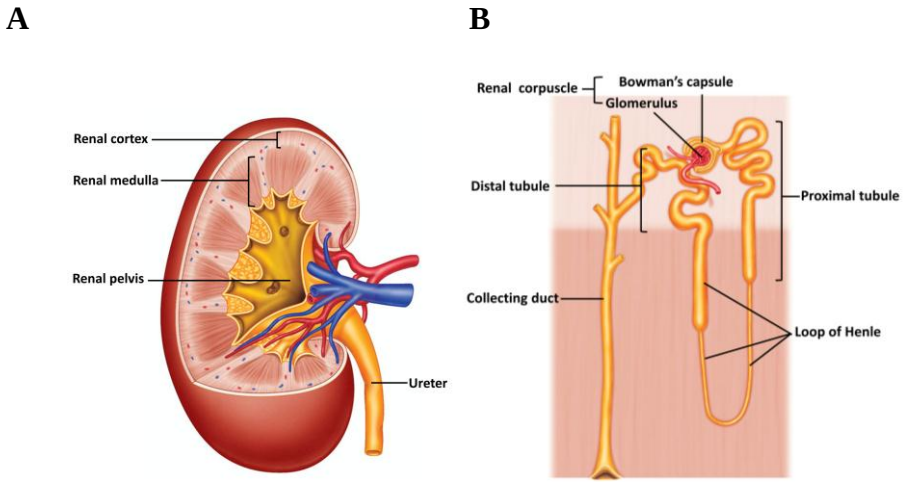

Figure 1.1. Anatomy of A) a kidney, and B) a nephron [12] *STANFIELD, CINDY L., PRINCIPLES OF HUMAN PHYSIOLOGY, 5th, ©2018. Reprinted by permission of Pearson Education, Inc., New York, New York.*

According to previous studies on the clearance pathway of inorganic NPs, renal excretion of a NP is dependent on its size, charge and shape in the bloodstream. In addition to core size, surface chemistry of NPs determines the actual size of NPs in the blood. A NP with surface chemistry having high affinity to proteins would form a protein “corona” during blood circulation, which leads to a dramatic size increase and uptake by the macrophage system. A negatively charged NP

can only be renally excreted with the size below kidney filtration threshold (KFT) while a positively charged one can be filtered with a size slightly larger than KFT. The effect of shape is reflected in the observation that a tube-shaped NP with length above KFT but width below it still passed by the GFM.[6a, 12]

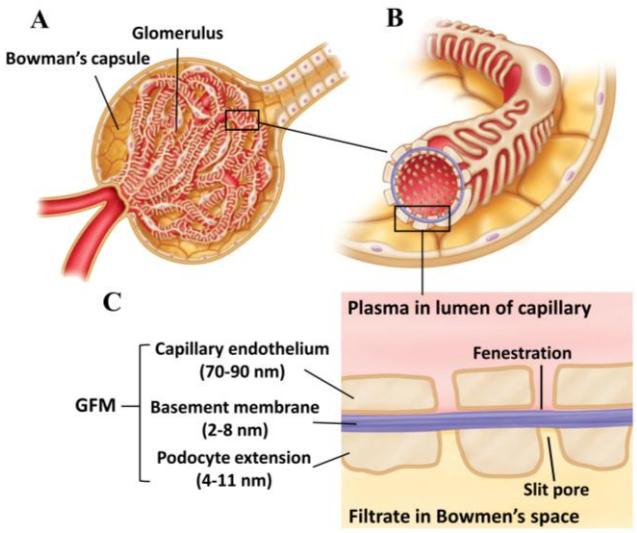

Figure 1.2. Anatomy of A) a renal corpuscle, and B,C) glomerular filtration membrane (GFM)[12] *STANFIELD, CINDY L., PRINCIPLES OF HUMAN PHYSIOLOGY, 5th, ©2018. Reprinted by permission of Pearson Education, Inc., New York, New York.*

1.3 Status of renal clearable inorganic NPs

In 2007, the first renal clearable inorganic NPs, cysteine-coated quantum dots (QDs), were created, whose renal clearance reached a maximum of 75% of the injection dose (ID) at 4 h post intravenous injection (p.i.). In the same study, the KFT for globular particles was determined to be 5.5 nm, based on the clearance profiles of different-sized QDs. This value has been recognized as the gold standard to predict the elimination pathway of a spherical NP.[7] Inspired by renal clearable QDs, silica NPs, gold NPs (AuNPs), carbon dots etc. with efficient renal excretion were developed. Core-shell fluorescent silica NPs, so-called Cornell dots, is the first renal clearable nanomedicine

that has been tested in a clinical trial. By conjugating ^{124}Iodine and active targeting ligands on the surface, Cornell dots are expected to be a highly biocompatible multimodal imaging probe for clinical cancer diagnosis.[8] The invention of renal clearable carbon dots was to alleviate nephropathy induced by Gd leakage from Gadolinium (Gd)-based contrast agents in magnetic resonance imaging (MRI). The Gd-incorporated carbon dots exhibited significantly increased stability and rapid renal elimination.[10] The renal clearable glutathione-coated AuNPs (GS-AuNPs) integrated with the fluorescence modality can sensitively detect kidney dysfunction and differentiate their stages based on altered kidney clearance kinetics, showing great potential as a high-sensitivity, low-cost kidney function indicator.[11b, 14] Many other renal clearable inorganic NPs have also been created, such as CuS nanodots,[15] Palladium nanosheets,[16] etc. with potential as agents for biomedical imaging and cancer photothermal therapy (Table 1.1).

Table 1.1. Characterization, renal clearance efficiency and application of selected renal clearable inorganic nanoparticles

	Core composition	**Core size, HD[a]** (nm)	**Surface chemistry**	**Renal clearance efficiency**	**Application**
Quantum Dots[7]	^{99m}Tc-CdSe/ZnS	2.85, 4.36	Cysteine	43.65% ID[d] at 4 h p.i.	--
		3.02, 4.99		62.18%ID at 4 h p.i.	
		3.30, 5.52		75.13% ID at 4 h p.i.	
Silica Nanoparticles[8a]	Silica, Cy5	--, 3.3	PEG$_{0.5kDa}$, ^{124}Iodine	70.55% ID at 24 h p.i.	Fluorescence/PET[e] imaging
		--, 6.0		58.82% ID at 4 h p.i.	
Gold Nanoparticles[9]	Au$_{640}$	2.6, 3.0	Glutathione	42% ID at 24 h p.i.	Fluorescence imaging
Carbon Nanodots[10]	C, Gd	12, 12	DTPA[b] residue	--	MRI[f]/Fluorescence imaging
CuS Nanodots[15]	^{64}Cu, CuS	4.3, 5.6	PVP[c]	95% ID at 24 h p.i.	PET, PTT[g]
Pd Nanosheets[16]	Pd	4.4, --	Glutathione	7.5 %ID at 24h p.i.	PTT

[a] HD, Hydrodynamic diameter; [b] DTPA, Diethylenetriamine pentaacetic acid; [c] PVP, Polyvinylpyrrolidone; [d] ID, Injection dose; [e] PET, Positron emission tomography; [f] MRI, Magnetic resonance imaging; [g] PTT, Photothermal therapy

1.4 Transport behavior of renal clearable inorganic NPs

The transport of renal clearable inorganic NPs within the kidneys includes two steps, filtration from the glomerulus into the Bowman's capsule and elimination through the tubular segments and pelvis into the ureter. The glomerular filtration occurs for NPs with size below KFT (6 nm) and the renal clearance efficiencies of NPs are influenced by multiple factors such as core density and injection dose. For example, 75 percent of the injected dose (%ID) of 3 nm QDs were cleared out from the kidneys within 4 h after intravenous injection.[7] The value was approximately 60% ID for 3.3 nm Cornell dots[8a] and only around 45% ID for 3 nm GS-AuNPs.[9] This core-material-dependent clearance efficiency was fundamentally attributed to the density effect on the margination of NPs in the blood flow. According to the study on clearance efficiency of several small metal NPs with different densities, as density increases the tendency of NPs to marginate to the blood vessel barrier increases. As a result, NPs with high density travel to the kidneys with a relatively slow rate compared to NPs with low density, leading to smaller renal clearance efficiency (Figure 1.3A).[17] Our most recent study on the dose influence on renal clearance of AuNPs showed that the clearance efficiency was also dose-related. In the CD-1 mouse model, above the dose of 15 mg/kg, a positive linear relationship was constructed between the dose and renal clearance at 2 h post injection (p.i.), whereas, doses below 15 mg/kg resulted in comparable clearance efficiency. This two-phase profile originated from the different propensity of NPs to extravasate from blood vessels and enter the extravascular space. Pharmacokinetics studies revealed that at 15 mg/kg and below, NPs could evenly distribute in the bloodstream and extravascular space at the initial time point, resulting in comparable blood concentration and renal clearance efficiency. As the dose increases, the extravasation of NPs from blood vessels decreases,

so the initial concentration of NPs in the blood increases and more NPs can be transported to the kidney and excreted in the urine.[18] These results indicated that the core density or injection dose could influence the renal filtration efficiency in an indirect way by altering the blood transport of NPs, where the kidneys passively received and filtered the NPs from the blood flow. However, when the size of the NPs is reduced to the sub-nanometer regime, the cellular interaction between the renal clearable NPs and the glomerulus occurs and dominates the filtration efficiency. For example, sub-nanometer glutathione-coated Au_{18}, Au_{15}, $Au_{10\text{-}11}$ can be trapped by glomerular endothelial glycocalyx; therefore, their renal clearance efficiencies were less than half of that of glutathione-coated Au_{25} (HD ≈ 1 nm) which was relatively inert to the glomerular endothelial glycocalyx (Figure 1.3B).[19]

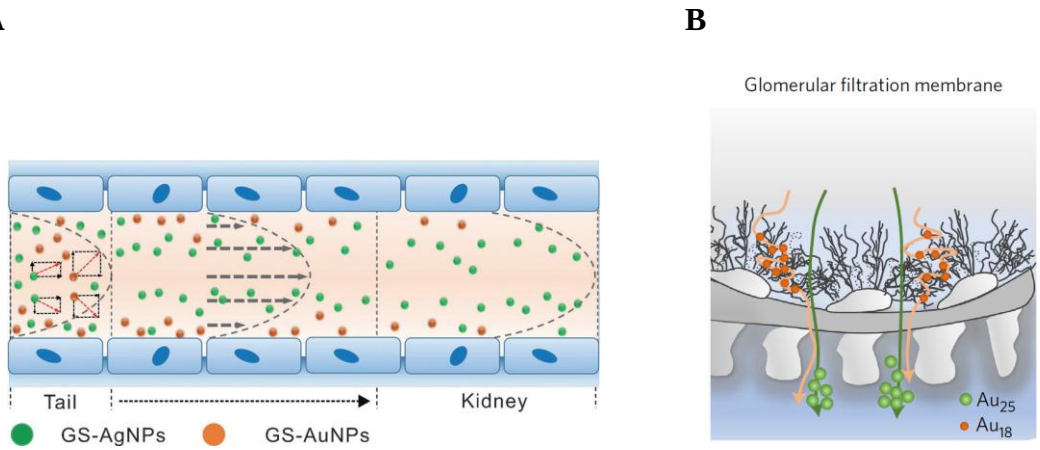

Figure 1.3. A) A scheme showing core density effect on magination of ultrasmall metal nanoparticles in the blood stream. Glutathione-coated gold nanoparticles (GS-AuNPs) tend to marginate to the blood vessel wall more than glutathione-coated silver nanoparticles (GS-AgNPs), resulting in smaller renal clearance efficiency. [17] (Reprinted with permission from Ref 17. Copyright 2016 Wiley-VCH Verlag GmbH & Co. KGaA, Weinheim B) A schematic showing Au_{18} are trapped by glomerular endothelial glycocalyx and Au_{25} easily pass through glomerular filtration membrane. As a consequence, Au_{25} exhibits larger renal clearance efficiency than that of Au_{18} within the same time.[19] (Reprinted by permission from Springer Nature: Nature Nanotechnology, "Glomerular barrier behaves as an atomically precise bandpass filter in a sub-nanometre regime", Du, B. et al., Copyright 2017)

The filtration efficiency of renal clearable inorganic NPs is a complex function of their blood transport and cellular interaction and can be influenced by multiple factors including core composition, injection dose and actual size *in vivo*. These observations highlight the importance of investigation of physiological responses to renal clearable NPs so as to precisely control the transport, clearance and targeting of renal clearable NPs in future clinical applications.

The renal-tubular processing of renal clearable inorganic NPs has not been well studied, as it requires a comprehensive investigation of the chemical interaction between tubular cells and NPs. As introduced earlier, after being filtered into Bowman's capsule, renal filtrate is transported through the proximal tubule, loop of Henle, distal tubule and collecting duct. The most intense NP-cell interaction is believed to occur in the proximal tubule where the epithelial cells constantly reabsorb vital solutes back into the blood stream through endocytosis. It is reported that GS-AuNPs are captured at microvilli formed on the tubular epithelia cells.[20] This might be a result of the glutathione reabsorption at the proximal tubules. The loop of Henle and distal tubule have much less interaction with filtered solutes than proximal tubules, but they facilitate water reabsorption, thereby concentrating NPs in this area. Eventually, the NPs are transported out of the tubular segments into the renal pelvis and pass through the ureters into the bladder. The tubular transport process could be altered under pathological conditions. We have demonstrated that glutathione-coated AuNPs were selectively accumulated in the interface of the renal medulla and the pelvis, where the loop of Henle and collecting ducts are located, after the ureter ligation. The intense and long-term accumulation of NPs further resulted in uptake of the particles by the tubular epithelial cells.[11a] Based on the above results, the tubular segments are more vulnerable to NPs than the

glomerulus. Future studies focusing on tubular interactions of renal clearable NPs would provide more fundamental understanding of the toxicity induced by renal clearable nanomedicine.

1.5 Biocompatibility of renal clearable inorganic NPs

The renal clearance of inorganic NPs has significantly reduced the exposure of the whole body to injected NPs because a large portion of them are rapidly excreted from the urinary system, instead of being trapped in the macrophage system and/or gradually processed by the liver. The liver and spleen are no longer primary targets for holding a large number of NPs, but receive significantly reduced NP accumulation. However, the workload of the kidneys dramatically increases. For example, at 24 h p.i., 1.3 ± 0.4 %ID, 40.5 ± 6.2%ID and 0.5 ± 0.1%ID of 13 nm non-renal clearable glutathione-coated AuNPs were found in the kidneys, liver and urine, while the values were 8.8 ± 2.0%ID, 3.7 ± 1.9%ID and 50.5 ± 7.1%ID for renal clearable 3 nm counterparts.[9] Therefore, the biocompatibility assessment of renal clearable inorganic NPs should emphasize the structural and functional changes of the kidneys after NP injection. To meet this requirement, the methods applied in the *in vivo* biocompatibility studies of renal clearable inorganic NPs include histological analysis of kidney tissues, measuring the levels of renal function biomarkers and hematological analysis, in addition to measurement of renal clearance and biodistribution. So far, among the reported renal clearable inorganic NPs, only GS-AuNPs, CuS nanodots and Cornell dots have been subjected to relatively comprehensive biocompatibility evaluation. CuS Nanodots were tested in mice at a dose of 80 mg/kg through intravenous administration.[15] GS-AuNPs were assessed after a single intravenous injection in a dose range of 15-1059 mg/kg in mice and at a dose of 250 mg/kg in non-human primates.[18]The ^{124}I-labeled Cornell dots have been evaluated in clinical trials at a

low dose for positron emission tomography imaging.[8b] None of the three NPs induced alteration of renal or hepatic function at their tested levels according to biochemical and histological analyses. Cornell dots were proved to be even safe for a patient with a history of compromised renal function. Histological analysis of mice receiving GS-AuNPs at a single dose of 1059 mg/kg suggested that both glomeruli and renal tubules remained intact. While residual NPs were spotted in the tubular lumen, they showed little damage to the adjacent renal tubular cells. These results indicated 1059 mg/kg of GS-AuNPs could be well tolerated in mice which was 2-35 times higher than the maximal tolerated dose (30-450 mg/kg) of a silica NPs in the same animal model.[21] These pilot studies have demonstrated the high tolerance of biological system to these renal clearable inorganic NPs. However, renal toxicity was observed from some ultrasmall metal NPs. 7.55 mg/kg glutathione-coated Au_{25} was found to cause acute immune responses and compromise of kidney function at 24 h post intraperitoneal injection, while these symptoms disappeared at 28 days p.i..[22] 15 mg/kg renal clearable platinum NPs with size less than 1 nm induced moderated cell necrosis at the tubular epithelium and urine cast in the kidneys at 24 h post intravenous injection.[23] These results imply the complexity of the kidney response to ultrasmall inorganic NPs, which demands future investigation on the influence of physicochemical properties of renal clearable NPs such as core composition, size and surface chemistry on the biocompatibility.

1.6 NP-cell interactions of renal clearable inorganic NPs

Understanding the NP-cell interactions is critical to safely using renal clearable inorganic NPs in the clinic, especially for patients with nephropathy, since prolonged retention of NPs could happen in diseased kidneys. Currently, the studies regarding this topic are limited. One pioneering work

illustrated that compared to rapid excretion of the cationic counterparts, 3.7 nm anionic QDots were largely kept within the glomerular capillary instead of being filtered. The QDots eventually passed the filtration membrane were gradually caught by mesangial cells, a type of phagocyte residing among glomerular capillaries.[24] This study was the first to provide knowledge on the cellular recognition of renal clearable inorganic NPs by a specific renal cell group. The previously discussed trapping of sub-nanometer glutathione-coated Au_{18}, Au_{15}, $Au_{10\text{-}11}$ by glomerular endothelial glycocalyx illustrated the non-specific interaction between NPs and membrane components.[19] Another group reported on the interactions between dendrimer-based and dextran-based organic renal clearable NPs and tubular epithelial cells *in vivo*.[25] Though the NP model was not inorganic, this work demonstrated the internalization of biologically-safe materials by tubular epithelial cells induced change in protein expression, which stressed on the necessity of investigation of NP-cell interactions of renal clearable inorganic NPs. All three studies are frameworks for future research on cell-NP interactions of renal clearable inorganic NPs. In addition, cellular deposition and interaction of renal clearable inorganic NPs under nephropathy also demands comprehensive investigation to assure their clinical safety.

1.7 Conclusion

In summary, the development of renal clearable inorganic NPs offers an opportunity to address the biosafety concerns of nonbiodegradable NPs with long-term body accumulation, which has been a long-term challenge for clinical translation of inorganic nanomedicine. To minimize nephrotoxicity of renal clearable NPs and maximize their diagnostic and therapeutic efficacy, it is necessary to (1) understand the biointeractions and transport of these NPs in the kidneys, (2)

evaluate the biocompatibility, and (3) study NP-cell interactions. Previous findings indicate the transport of these NPs in the kidneys is influenced by multiple factors under distinct mechanisms. For example, core density and injection dose change the renal clearance efficiency by altering the blood transport of the NPs. Scaling down the particle size to the sub-nanometer regime increases the affinity of the NPs to the glomerular endothelial glycocalyx, leading to reduced renal clearance efficiency. Ureter ligation induced nephropathy can cause selective deposition of the NPs in the renal tubular segments. Though only a limited number of renal clearable inorganic NPs received thorough biocompatibility assessment, high tolerance of the kidneys and the whole body to NP exposure was illustrated on all the tested NPs. Studies on NP-cell interactions are still at the initial stage, however, the findings on uptake of anionic NPs by mesangial cells and trapping of sub-nanometer NPs by membrane glycocalyx are insightful. Future research is expected to improve the fundamental understanding of the three discussed aspects, in addition to developing applications so as to translate the renal clearable nanomedicine into the clinic.

1.8 References

[1] a) N. Erathodiyil, J. Y. Ying, *Accounts of Chemical Research* **2011**, *44*, 925-935; b) S. E. Lohse, C. J. Murphy, *Journal of the American Chemical Society* **2012**, *134*, 15607-15620; c) M. C. Tan, G. M. Chow, L. Ren, Q. Zhang, in *NanoScience in Biomedicine* (Ed.: D. Shi), Springer Berlin Heidelberg, Berlin, Heidelberg, **2009**, pp. 272-289.

[2] M. Walling, J. Novak, J. R. E. Shepard, *International Journal of Molecular Sciences* **2009**, *10*, 441.

[3] C. K. Kim, P. Ghosh, C. Pagliuca, Z.-J. Zhu, S. Menichetti, V. M. Rotello, *Journal of the American Chemical Society* **2009**, *131*, 1360-1361.

[4] a) X. Huang, I. H. El-Sayed, W. Qian, M. A. El-Sayed, *Journal of the American Chemical Society* **2006**, *128*, 2115-2120; b) P. K. Jain, K. S. Lee, I. H. El-Sayed, M. A. El-Sayed, *The Journal of Physical Chemistry B* **2006**, *110*, 7238-7248.

[5] E. Blanco, H. Shen, M. Ferrari, *Nature Biotechnology* **2015**, *33*, 941.

[6] a) J. Liu, M. Yu, C. Zhou, J. Zheng, *Materials Today* **2013**, *16*, 477-486; b) M. Yu, J. Zheng, *ACS Nano* **2015**, *9*, 6655-6674.

[7] H. Soo Choi, W. Liu, P. Misra, E. Tanaka, J. P. Zimmer, B. Itty Ipe, M. G. Bawendi, J. V. Frangioni, *Nature Biotechnology* **2007**, *25*, 1165.

[8] a) A. A. Burns, J. Vider, H. Ow, E. Herz, O. Penate-Medina, M. Baumgart, S. M. Larson, U. Wiesner, M. Bradbury, *Nano Letters* **2009**, *9*, 442-448; b) E. Phillips, O. Penate-Medina, P. B. Zanzonico, R. D. Carvajal, P. Mohan, Y. Ye, J. Humm, M. Gönen, H. Kalaigian, H. Schöder, H. W. Strauss, S. M. Larson, U. Wiesner, M. S. Bradbury, *Science Translational Medicine* **2014**, *6*, 260ra149-260ra149.

[9] Z. Chen, L. Michael, Q. Yanping, S. Xiankai, Z. Jie, *Angewandte Chemie International Edition* **2011**, *50*, 3168-3172.

[10] C. Hongmin, W. G. D., T. Wei, T. Trever, Z. Zipeng, T. Chu, H. Khan, C. Taku, H. R. B., Z. Weizhong, S. John, S. Baozhong, X. Jin, *Advanced Materials* **2014**, *26*, 6761-6766.

[11] a) X. Jing, Y. Mengxiao, C. Phoebe, H. Elizabeth, D. Andrew, K. Payal, H. Jer‐Tsong, Z. Jie, *Angewandte Chemie International Edition* **2017**, *56*, 13356-13360; b) Y. Mengxiao, Z. Jiancheng, D. Bujie, N. Xuhui, A. Craig, G. Leah, K. Payal, H. Jer‐Tsong, Z. Jie, *Angewandte Chemie International Edition* **2016**, *55*, 2787-2791.

[12] C. Stanfield, *Principles of human physiology*, 12 ed., Pearson Higher Ed, **2012**.

[13] a) S. Chien, *Vascular Endothelium in Health and Disease*, Springer, Boston, MA, **1988**; b) A. Singh, S. C. Satchell, C. R. Neal, E. A. McKenzie, J. E. Tooke, P. W. Mathieson, *Journal of the American Society of Nephrology* **2007**, *18*, 2885-2893.

[14] Y. Mengxiao, L. Jinbin, N. Xuhui, Z. Jie, *Angewandte Chemie International Edition* **2015**, *54*, 15434-15438.

[15] M. Zhou, J. Li, S. Liang, A. K. Sood, D. Liang, C. Li, *ACS Nano* **2015**, *9*, 7085-7096.

[16] T. Shaoheng, C. Mei, Z. Nanfeng, *Small* **2014**, *10*, 3139-3144.

[17] T. Shaoheng, P. Chuanqi, X. Jing, D. Bujie, W. Qingxiao, V. R. D., Y. Mengxiao, K. M. J., Z. Jie, *Angewandte Chemie International Edition* **2016**, *55*, 16039-16043.

[18] X. Jing, Y. Mengxiao, P. Chuanqi, C. Phoebe, T. Jia, N. Xuhui, Z. Qinhan, T. Qiu, Z. Greg, D. Anthony, J. Xingya, K. Payal, H. Jer‐Tsong, Z. Xudong, L. Pengyu, Z. Jie, *Angewandte Chemie International Edition* **2018**, *57*, 266-271.

[19] B. Du, X. Jiang, A. Das, Q. Zhou, M. Yu, R. Jin, J. Zheng, *Nature Nanotechnology* **2017**, *12*, 1096.

[20] M. G. Lawrence, M. K. Altenburg, R. Sanford, J. D. Willett, B. Bleasdale, B. Ballou, J. Wilder, F. Li, J. H. Miner, U. B. Berg, O. Smithies, *Proceedings of the National Academy of Sciences* **2017**, *114*, 2958-2963.

[21] T. Yu, K. Greish, L. D. McGill, A. Ray, H. Ghandehari, *ACS Nano* **2012**, *6*, 2289-2301.

[22] X.-D. Zhang, D. Wu, X. Shen, P.-X. Liu, F.-Y. Fan, S.-J. Fan, *Biomaterials* **2012**, *33*, 4628-4638.

[23] Y. Yamagishi, A. Watari, Y. Hayata, X. Li, M. Kondoh, Y. Yoshioka, Y. Tsutsumi, K. Yagi, *Nanoscale Research Letters* **2013**, *8*, 395.

[24] X. Liang, H. Wang, Y. Zhu, R. Zhang, V. C. Cogger, X. Liu, Z. P. Xu, J. E. Grice, M. S. Roberts, *ACS Nano* **2016**, *10*, 387-395.

[25] A. V. Nair, E. J. Keliher, A. B. Core, D. Brown, R. Weissleder, *ACS Nano* **2015**, *9*, 3641-3653.

CHAPTER 2

IN VIVO X-RAY IMAGING OF TRANSPORT OF RENAL CLEARABLE GOLD NANOPARTICLES IN THE KIDNEYS

Authors - Jing Xu[†], Mengxiao Yu[†], Phoebe Carter[†], Elizabeth Hernandez[§], Andrew Dang[§], Payal Kapur[#], Jer-Tsong Hsieh[§] and Jie Zheng[†§*]

[†]Department of Chemistry and Biochemistry, BE 26

The University of Texas at Dallas

800 W. Campbell Rd., Richardson, TX 75080 (USA)

[§]Department of Urology

The University of Texas Southwestern Medical Center

5323 Harry Hines Blvd., Dallas, TX 75390 (USA)

[#]Department of Pathology

The University of Texas Southwestern Medical Center

5323 Harry Hines Blvd., Dallas, TX 75390 (USA)

Reprinted (adapted) with permission from J. Xu, et al., *Angewandte Chemie International Edition* **2017**, *56*, 13356–13360.

Abstract

With more and more engineered nanoparticles (NPs) being designed renal clearable for clinical translation, fundamental understanding of their transport in the different compartments of kidneys becomes increasingly important. Here, we report noninvasive X-ray imaging of renal clearable gold NPs (AuNPs) in normal and nephropathic kidneys. By quantifying the transport kinetics of the AuNPs in cortex, medulla and pelvis of the normal and injured kidneys, we found that ureteral obstruction not only blocked the NP elimination through the ureter but also slowed down their transport from the medulla to pelvis and enhanced the cellular uptake. Moreover, the transport kinetics of the NPs and renal anatomic details can be precisely correlated with local pathological lesion. These findings not only advance our understandings of nano-bio interactions in the kidneys but offer a new pathway to noninvasively image kidney dysfunction and local injuries at the anatomical level.

2.1 Introduction

Fundamental understandings of *in vivo* nano-bio interactions are key to future clinical translation of nanomedicines. In the past decades, significant progress has been made in quantitative understandings of nano-bio interactions in the liver[1] and tumor microenvironment.[2] However, there are still limited studies on how engineered NPs interact with the kidneys[3] even though more and more nanomedicines are designed renal clearable to expedite their clinical translation. For example, Choi et al. reported 3 nm cysteine-coated CdSe/ZnS quantum dots, 75% of which can be excreted in urine within 4 h after intravenous injection.[4] Furthermore, they also demonstrated their applications in cancer imaging in the preclinical settings.[5] Bradbury et al. developed 6-7 nm dye-doped silica NPs (Cornell dots) that have renal clearance efficiency of 73% at 48 h post intravenous injection in mice.[6] The whole body clearance of C dots was only 13~21 hours in humans.[7] We reported the first renal clearable luminescent AuNPs[8] and demonstrated their preclinical applications in cancer detection[9] and noninvasive fluorescence kidney functional imaging.[10] With the emergence of more and more renal clearable NPs,[11] it becomes urgent to fundamentally understand how these renal clearable NPs are transported in the different compartments of the kidneys with normal or injured functions at the anatomical level; so that their future promise can be fulfilled while their potential hazards, in particular, to the patients with kidney dysfunctions, can be minimized.

Herein, we report our pivotal studies on *in-vivo* X-ray imaging of interaction between renal clearable AuNPs and the kidneys with normal function and unilateral ureteral obstruction (UUO). Our results show that the accumulation and clearance of renal clearable AuNPs in normal and obstructed kidneys can be quantitatively and noninvasively evaluated with planar X-ray imaging

at contrast 6 times higher than iodine complexes. In the kidneys with normal function, transport kinetics of AuNPs in cortex, medulla and pelvis of kidney follow a simple one-component exponential decay with comparable half-lives. However, in the dysfunctional kidney with ureteral obstruction, the transport of the AuNPs from the cortex and medulla into the pelvis was significantly slowed down while the transport of the NPs into the cortex was not delayed. Moreover, high-penetration depth and high-spatial resolution of X-ray imaging allowed us to precisely identify the location of impairments, which caused significant alteration in the clearance kinetics of the AuNPs.

2.2 Experimental

2.2.1 Materials and equipment

Diatrizoate meglumine ($C_7H_{17}NO_5 \cdot C_{11}H_9I_3N_2O_4$), hydrogen tetrachloroaurate ($HAuCl_4$) and L-reduced glutathione (GSH) were purchased from Sigma-Aldrich. Harris hematoxylin and erosin-Y were from Fisher Scientific (Waltham, USA). *In-vivo* X-ray imaging was conducted using an In-Vivo Xtreme I system from Bruker.

2.2.2 Methods

GS-AuNPs synthesis

The near-infrared-emitting GS-AuNPs were synthesized using a previously reported method.[9c] Basically, 1 M $HAuCl_4$ aqueous solution was mixed with 2.4 mM glutathione aqueous solution. The mixture was vigorously stirred and heated at 95 ℃. The solution was then cooled down to room temperature and centrifuged to remove the aggregates. GS-AuNPs were further precipitated

by mixing with ethanol, followed by centrifugation. The pellet was suspended in deionized water and purified by being dialyzed using dialysis tubing. The solution was lyophilized to remove the water and the dry powder was redissolved in phosphate buffered solution (PBS) followed by centrifugation. The obtained supernatant was for animal studies.

Animal models

The animal experiments were conducted following the guidelines of the University of Texas System Institutional Animal Care and Use Committee. Female ICR (CD-1) outbred mice (8-24 weeks old, ~30 g) were obtained from Envigo and housed under standard environmental conditions with free access to water and food. Unilateral ureteral obstruction (UUO) models were prepared according to a published literature.[10b] Briefly, an incision was made at the left flank to expose the ureter and complete obstruction was performed at the site close to the renal pelvis. The sham group was prepared in the same procedure except that the ureter was only exposed not ligated.

In vitro contrast comparison between GS-AuNPs and diatrizoate meglumine

Diatrizoate meglumine (DM, 200 μL of 5 mM) in PBS and 2.5 nm GS-AuNPs ($Au_{640}SG_{183}$, 200 μL of 0.023 mM)[13] in PBS were prepared in one 96-well plate resulting in an equal amount (0.004 mmol) of Au and Iodine. X-ray attenuation of each solution was measured under 45 kvp potential, 0.8 mm beam filter and 15s exposure. The results were calculated as (X.D.GS-AuNPs – X.D.PBS) / (X.D. DM – X.D. PBS), where X.D. is X-ray density (a.u.).

Noninvasive X-ray imaging of urinary system after intravenous injection of GS-AuNPs

X-ray tube potential of In-Vivo Xtreme I was set at 45 kvp, 0.8 mm beam filter and exposure time was 15s for both static and continuous imaging. The ICR (CD-1) mouse was anesthetized by 3% isoflurane and a catheter was inserted into the tail vein before the mouse was transferred into the imaging chamber and placed in the supine position. A static X-ray image was taken before injection of GS-AuNPs as "Pre" image and 200 μL of 0.15 g/mL buffered GS-AuNPs was injected followed by consecutive imaging until 60 min post injection (p.i.).

Noninvasive X-ray kidney imaging was performed on normal mice (N=8), UUO (N = 8) and sham (N = 3) mice. For UUO and sham mice, there was a one-day interval between surgery operation and imaging.

Noninvasive X-ray kidney imaging using diatrizoate meglumine as contrast agent

Diatrizoate meglumine (200 μL of 135 mg/ml) in PBS was intravenously injected in the ICR (CD-1) mouse (N = 3) as a control to compare the kidney contrast generated by the same number of iodine atoms as gold atoms in GS-AuNPs. Diatrizoate meglumine (200 μL of 540 mg/ml) in PBS was intravenously injected in the ICR (CD-1) mouse (N = 3) to compare the kidney contrast provided by iodine which attenuated equal X-ray radiation as injected GS-AuNPs. Setting of X-ray tube potential and exposure time were same as above. The imaging process was conducted on normal mice (N = 3) and followed the same procedure to compare kidney contrast.

Image analysis

Image analysis was conducted using the bundled software of In-Vivo Xtreme I. The regions of interest (ROI) were selected based on the highest contrast X-ray image at the kidney area.

Preparation of kidney section and pathological analysis

Mice were euthanized once the imaging process was finished and kidneys were harvested and preserved in 10% buffered formalin solution for at least 24 h. The fixed kidneys were embedded in paraffin, sectioned at 4 μm and stained by Harris hematoxylin and erosin-Y. Pathological analysis of tissue deterioration was performed by the pathologist in blind.

Silver staining of kidney section

Paraffin was first removed from the sectioned kidney tissue, then 0.1 M silver nitrate aqueous solution and 0.2 mg/mL hydroquinone aqueous solution were added onto the kidney section at 1:1 (V/V) ratio. After 10-30 min incubation with the mixed solution, the kidney section was thoroughly rinsed using deionized water for several seconds and dried at room temperature.

Measurement of the limits of detection for renal clearable GS-AuNPs

(1) The limit of detection in PBS solution

We prepared a series of GS-AuNPs solutions which contained Au amounts of 22.9, 16.0, 11.5, 5.7, 2.9, 1.4, and 0.2 mg; the Au amounts were verified by inductively coupled plasma mass spectrometry (ICP-MS). Each sample was in 200 μl PBS and the same volume of PBS was used to measure the background signal. The X-ray image was obtained under the same imaging setting

as our non-invasive animal study. The number of GS-AuNPs is calculated according to previously obtained chemical formula of 2.5 nm NIR-emitting GS-AuNPs ($Au_{640}SG_{183}$ in average).[16]

(2) The limit of detection in kidney *in vivo*

We monitored the contrast of kidneys after intravenously injecting the GS-AuNPs and euthanized the animals when the contrast reached the maximum (the maximal contrast of kidneys was usually observed when GS-AuNPs largely accumulated in the renal pelvis and started to illuminate the ureters). The kidneys were collected in intact form and dissolved completely in aqua regia for Au quantification by ICP-MS.

Evaluation of the accuracy of planar X-ray imaging in quantifying %ID of GS-AuNPs

We compared the percentage of injected dose (%ID) of GS-AuNPs in the kidney and the bladder measured by X-ray imaging with the results obtained by ICP-MS. Briefly, three CD-1 mice were intravenously injected with 1 g/kg GS-AuNPs and imaged before and after injection under X-ray radiation. For X-ray imaging quantification, we first constructed a calibration curve between X-ray density (a.u.) of GS-AuNPs and gold amount *in vitro*, and then used this calibration curve to convert the total X-ray densities of the kidney area and bladder area to %ID of GS-AuNPs. We selected two time points, one is when the kidney contrast reached the maximum and the other is when the kidney contrast decreased to the minimum level. For ICP-MS measurements, the mice were euthanized when the contrast of the kidneys were the maximum or minimum. The kidneys and urine in the bladder were collected and prepared for Au quantification by ICP-MS.

2.3 Results and Discussion

2.3.1 Characterization of near-infrared-emitting GS-AuNPs

The near-infrared-emitting GS-AuNPs were synthesized using a previously reported method.[9c] The core size and hydrodynamic diameter (HD) of GS-AuNPs were characterized to be 2.5 ± 0.3 nm, and 3.1 ± 0.8 nm, respectively. GS-AuNPs exhibited a strong resistance to serum protein binding after 30 min incubation with 10% fetal bovine serum in biological buffer suggesting high physiological stability. According to elemental analysis, the chemical formula of the GS-AuNPs was confirmed to be $Au_{640}SG_{183}$.[9c,16]

2.3.2 GS-AuNPs enabled X-ray imaging of the kidneys

To test whether simple planar X-ray imaging can readily detect the accumulation and clearance of GS-AuNPs in kidneys, we intravenously injected the CD-1 mice with GS-AuNPs at a dose of 1g/kg body weight (corresponding to 0.69 g Au/kg). This dose was 3.9 times less than that used for commercially available AuNPs for X-ray imaging of mice (2.7 g Au/kg).[12] The histological study confirmed that the injected GS-AuNPs were well tolerated by CD-1 mice and no structural changes were found in major organs at Day 1 and Day 14 post injection (p.i.; Figure 2.1).

With planar X-ray imaging, the elimination of GS-AuNPs through the urinary system indeed can be noninvasively monitored at high contrast. The GS-AuNPs were clearly observed in the renal cortex, medulla and pelvis of the kidney at around 2 min p.i., followed by clearance through the pelvis into the ureter and then into the bladder during 2-5 min p.i.. The bladder became detectable at ~2 min p.i. and was gradually filled with AuNPs until 30 min p.i. (Figure 2.2A&2B).

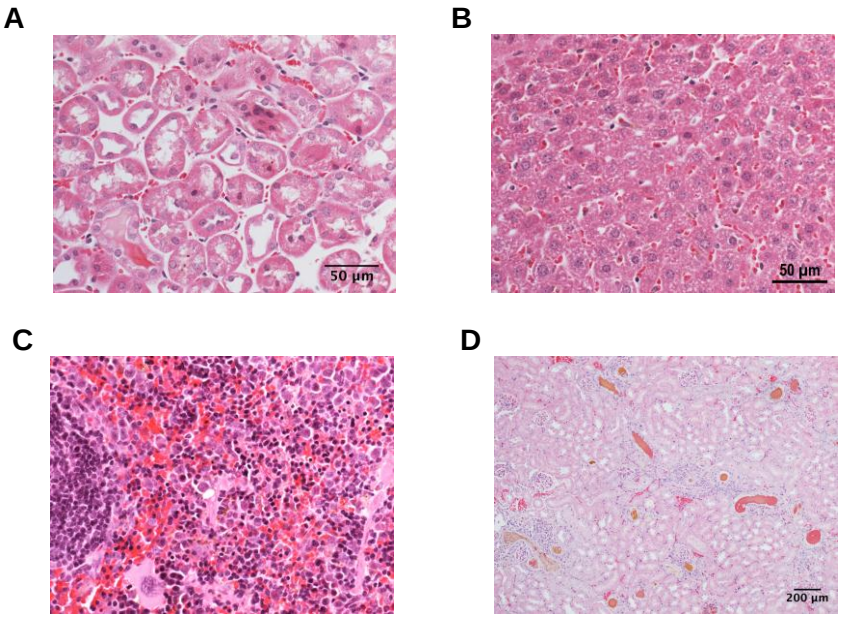

Figure 2.1. Histological analysis of (A) kidney, (B) liver and (C) spleen harvested on Day 1, and (D) kidney harvested on Day 14 after intravenous injection of 1g/kg of GS-AuNPs into CD-1 mice.

2.3.3 Detection limit and accuracy in quantification of GS-AuNPs using planar X-ray imaging

To optimize the dose selection of GS-AuNPs for X-ray kidney imaging and to quantitatively determine the Au amount in the kidneys, we investigated the detection limit of GS-AuNPs under our current experimental settings both *in vitro* and *in vivo*. A series of GS-AuNPs in PBS solution were prepared with Au amounts of 22.9, 16.0, 11.5, 5.7, 2.9, 1.4, and 0.2 mg and the X-ray attenuation of each was measured (Figure 2.3A). The results indicated the detection limit *in vitro* was approximately 0.2 mg Au whose X-ray attenuation was 1.05 times of background signal. According to the formula $Au_{640}SG_{183}$ of GS-AuNPs, 0.2 mg Au can be converted to approximately 9.6×10^{14} NPs. A calibration curve was also obtained based on this *in vitro* result as a quantification reference for *in vivo* detection (Figure 2.3B).

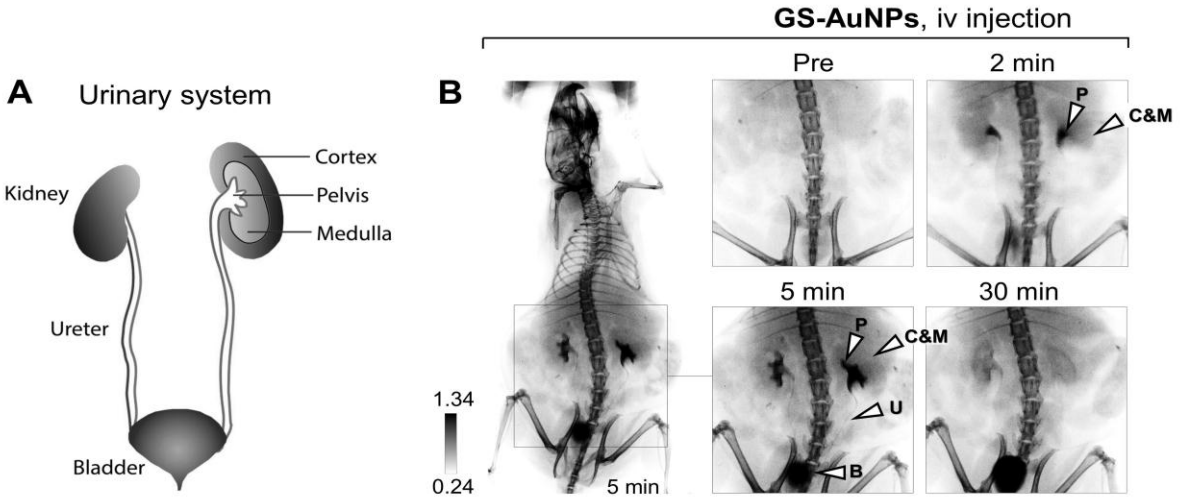

Figure 2.2. A) A scheme showing the urinary system that consists of the kidneys, ureters and bladder. B) Representative noninvasive X-ray images of CD-1 mice before (pre) and after intravenous injection of 1g/kg GS-AuNPs at 2, 5 and 30 min p.i. (arrows point to substructures of the kidney and components of the urinary system ("C & M", cortex and medulla; "P", pelvis; "B", bladder).

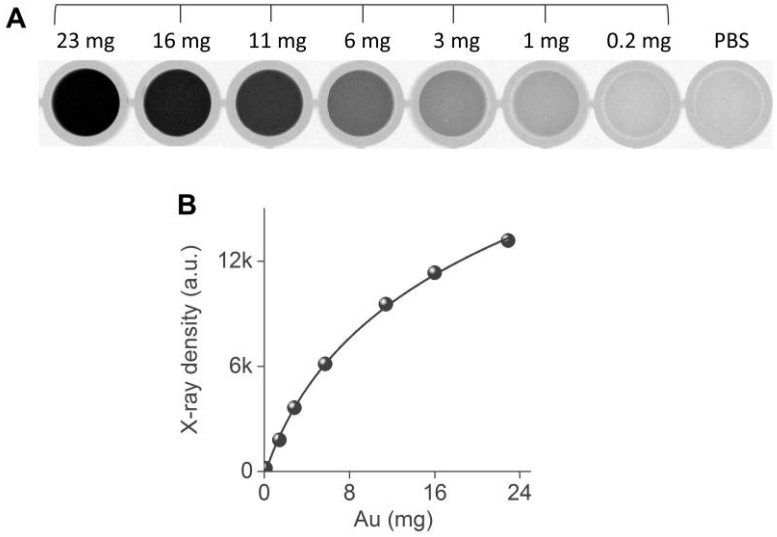

Figure 2.3. Quantification of the detection limit of GS-AuNPs in PBS solution. A) The X-ray image of GS-AuNPs solution in 200 µL PBS containing 22.9, 16.0, 11.5, 5.7, 2.9, 1.4, and 0.2 mg Au. Control sample was 200 µL PBS. B) Relationship between X-ray density generated by GS-AuNPs and the absolute Au amount. The fitted power function described by the equation y=246952.34887(x+3.82257)^0.02598-255594.14861 (R^2=0.9993). y=X-ray density, x=Au amount (mg)

However, it was harder to determine the *in vivo* detection limit due to the interference from background tissue, especially intestines and bones. We euthanized the mice when the contrast reached the maximum and minimum, respectively, and harvested the kidneys for Au quantification. The results indicated that the Au amount in kidneys generating maximal contrast was 5.4 ± 1.1 mg per gram of kidney tissue (N = 5, Table 2.1). According to Figure 2.4A, the maximum contrast was 1.28x of background signal (the maximal contrast enhancement was 27.9%). Since the contrast is proportional to the amount of Au distributed in kidney tissue, the detection limit is considered proximately the Au amount per tissue gram (mg/g) generating maximal contrast divided by 1.28. Therefore, the detection limit was calculated to be 4.2 ± 0.9 mg/g, corresponding to (2.0 ± 0.4) $\times 10^{16}$ GS-AuNPs per gram of kidney tissue. To confirm the accuracy of using kidney contrast to estimate the detection limit of GS-AuNPs, mice were euthanized when the kidney contrast almost dropped to the level comparable to background tissue (Figure 2.4B). The Au amount in the kidneys was 2.0 ± 1.1 mg/g (N = 6) (Table 2.1), corresponding to (9.4 ± 5.3) $\times 10^{15}$ GS-AuNPs per gram of kidney tissue, which is comparable to the amount determined by kidney contrast.

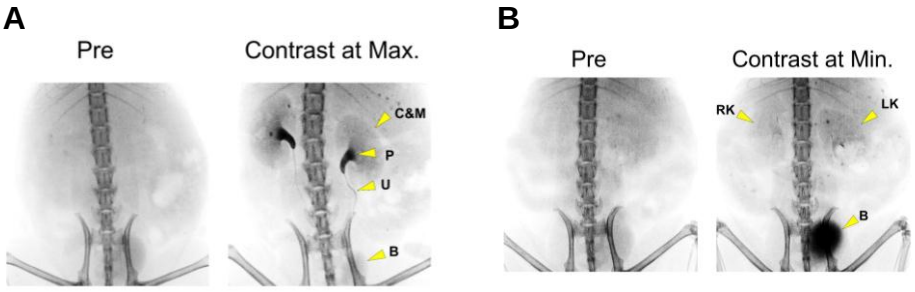

Figure 2.4. Representative noninvasive X-ray images of CD-1 mice before (Pre) and after injection of 1 g/kg GS-AuNPs when the kidney contrast reached the maximal value A), or minimal value B).

Table 2.1. Au amount per gram of kidney tissue (mg/g) quantified by ICP-MS when the kidney contrast reached the maximum or minimum

Kidney Contrast at Maximum #Kidney	Au amount per gram of kidney tissue (mg/g)
K1	6.5
K2	6.4
K3	4.6
K4	3.9
K5	5.4
Mean ± SD	5.4 ± 1.1
Kidney Contrast at Minimum **#Kidney**	**Au amount per gram of kidney tissue (mg/g)**
K1’	0.9
K2’	0.9
K3’	3.5
K4’	2.9
K5’	2.3
K6’	1.3
Mean ± SD	2.0 ± 1.1

Where “K” is kidney; “Mean ± SD” is mean value ± standard deviation

Meanwhile, we found the dose of 1 g/kg was about the minimal dose for imaging the NP transport in the kidneys as the 0.5 mg/kg could not render a contrast image showing kidney components. (Figure 2.5). On the other hand, it should be noted that background tissues indeed have interference on the accurate quantification of the percentage injected dose (%ID) of GS-AuNPs in the kidneys and bladder *in vivo* at low contrast (Figure 2.4 and Tables 2.2&2.3).

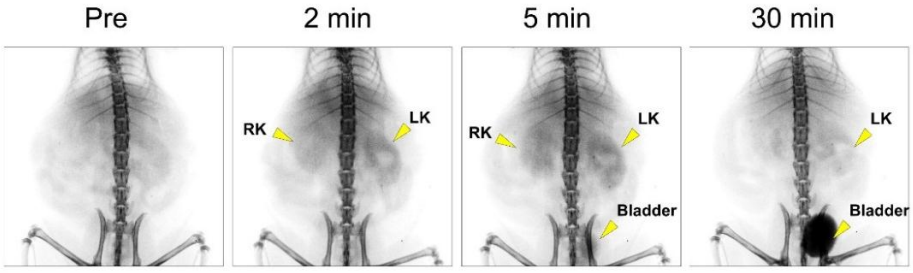

Figure 2.5. Representative noninvasive X-ray images of CD-1 mice before (Pre) and at 2 min, 5 min and 30 min post injection of 0.5 g/kg GS-AuNPs. Yellow arrows indicated right kidney (“RK”), left kidney (“LK”) and bladder.

Table 2.2. Comparison of the Au amounts in kidneys that were quantified by ICP-MS and planar X-ray imaging (Contrast at Maximum, N = 5; Contrast at Minimum, N = 6).

Au amount in kidney (mg), kidney contrast at maximum			
Kidney	ICP-MS	X-ray	Variation%
K1	2.10	1.74	17.16
K2	2.11	1.85	12.03
K3	1.08	0.95	12.37
K4	1.30	1.56	19.71
			M ± SD: 15.32 ± 3.75
Au amount in kidney (mg), kidney contrast at minimum			
Kidney	ICP-MS	X-ray	**Variation%**
K1’	0.27	0.19	30.24
K2’	1.01	0.54	47.07
K3’	0.87	1.28	47.24
K4’	0.58	0.43	25.21
K5’	0.37	0.45	22.52
			M ± SD: 34.46 ± 11.92

Where, “K” is kidney, “Variation%” = |“ICP-MS”-“X-ray” |/ “ICP-MS”×100%; “M ± SD” is mean value ± standard deviation.

Table 2.3. Comparison of the Au amounts in bladder that were quantified by ICP-MS and planar X-ray imaging. (Contrast at Maximum, N= 3, Contrast at Minimum, N = 3).

Au amount in bladder (mg), kidney contrast at maximum			
Bladder	ICP-MS	X-ray	**Variation%**
B1	0.13	-0.01	106.88
B2	4.87	0.70	85.56
B3	2.18	0.96	56.07
			M ± SD: 82.84 ± 25.51
Au amount in bladder (mg), kidney contrast at minimum			
Bladder	ICP-MS	X-ray	**Variation%**
B1’	3.87	5.61	44.85
B2’	7.40	3.66	50.63
B3’	5.01	3.53	29.58
			M ± SD: 41.69 ± 10.88

Where, “B” is bladder, “Variation%” = | “ICP-MS”-“X-ray” |/ “ICP-MS”×100%; “M ± SD” is mean value ± standard deviation.

The data showed that the two methods had a 34.46 ± 11.92% variation in determining Au amounts in kidneys at the minimum kidney contrast, but the variation decreased to 15.32 ± 3.75% at the

maximum kidney contrast. The variation of the results in kidneys was due to the X-ray absorption of soft tissues (stomach, intestine and liver) that changed as the mouse moved during the imaging process.

The variation between the two methods was 40-85% in measuring Au amounts in bladder. The inaccuracy in the Au measurement in the bladder originated from the significant X-ray attenuation of the spinal bone at the bladder area, which interfered with the AuNP signals in the bladder and could not be subtracted precisely. Therefore, the %ID of GS-AuNPs measured by X-ray imaging has a variation from those quantified by ICP-MS due to interference of background tissues. To improve the accuracy of X-ray imaging in quantifying %ID of AuNPs, we need to optimize the imaging conditions and methods to subtract the background signals from the tissues.

2.3.4 Comparison on the contrast enhancement of GS-AuNPs and diatrizoate meglumine (DM) for X-ray imaging

To determine if the contrast generated by GS-AuNPs was comparable to that of clinically used iodine-based contrast agents, we conducted a head-to-head comparison between GS-AuNPs and diatrizoate meglumine (DM), a clinically applied iodine-based contrast medium. The comparison was first conducted *in vitro*. Basically, we prepared GS-AuNPs and DM in biological buffered solution containing the same number of radiopaque atoms as the bulk X-ray attenuation is roughly the sum of the absorbed radiation by each of the radiopaque atoms (Figure 2.6A). Under the same instrumental setting as the one used for *in vivo* X-ray imaging, the GS-AuNPs solution exhibited approximately four times more X-ray absorption as that of DM (Figure 2.6B).

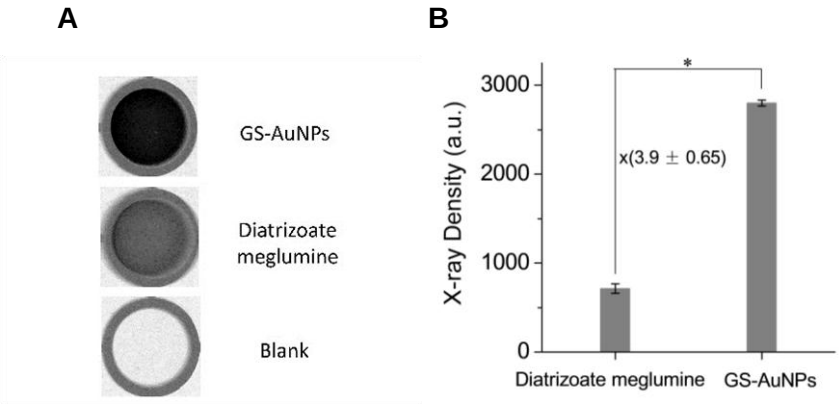

Figure 2.6. A) Representative X-ray image of GS-AuNPs and diatrizoate meglumine (DM) in buffered solution with equal amount of atoms of radiopaque elements. B) Quantitative analysis of X-ray attenuation of GS-AuNPs and DM with equal amount of radiopaque element atoms . (*P < 0.05).

The comparison was then performed at the *in vivo* level. The dynamic X-ray imaging of CD-1 mice after intravenously receiving GS-AuNPs and DM, respectively, indicated that the high-contrast X-ray images of the renal clearance process cannot be readily achieved with DM under the same imaging conditions. While the accumulation of DM in the bladder was observed, its clearance from the kidneys and ureters was barely detected during the entire imaging period. (Figure 2.7A&B).

Quantitative analysis showed that the percentage of kidney contrast enhancement by GS-AuNPs was nearly six times higher than that by DM at 4 min p.i. (27.9 % vs. 4.4%) (Figure 2.7B&Figure 2.8A). Since X-ray attenuation by gold is about 4x higher than of that by iodine (Figure 2.6B), we intravenously injected the mice with four-time concentrated DM (DM 4×), which has equal X-ray attenuation as GS-AuNPs. While the kidney contrast indeed increased (Figure 2.7C&D), the maximal percentage kidney contrast enhancement by DM was only 10.3%, still nearly three times less than that by GS-AuNPs (27.9%; Figure 2.7D&Figure 2.8A). These results clearly indicate that

high-contrast X-ray imaging of the kidneys enabled by GS-AuNPs *in vivo* is not only because of high X-ray attenuation of gold atoms but also due to longer retention of GS-AuNPs in the kidneys than DM, which allows us to further quantify the clearance kinetics of the NPs in the different kidney substructures.

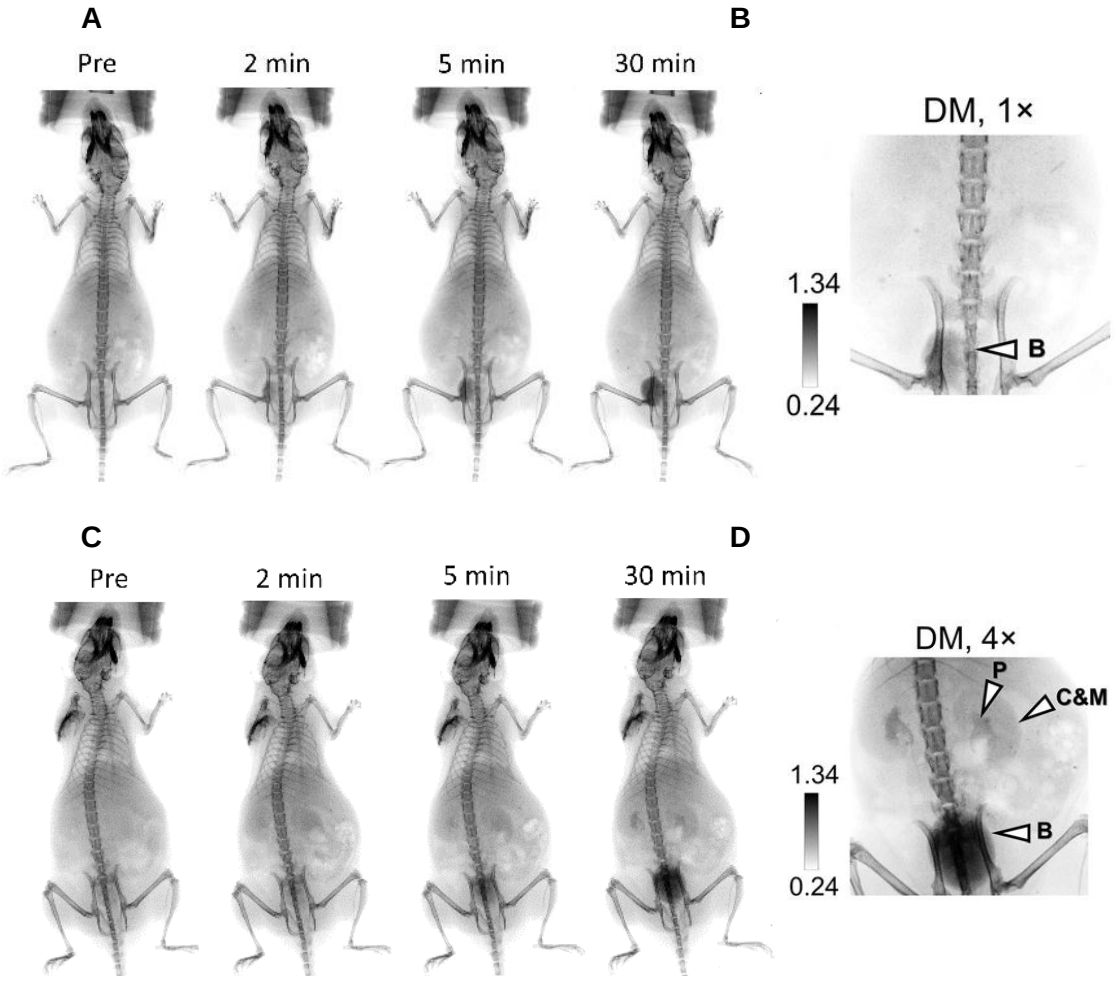

Figure 2.7. A) Representative X-ray images of mice before and after injection of diatrizoate meglumine (DM) at a dose containing the same amount of iodine atoms as gold atoms in the injected GS-AuNPs (200 µl, 135 mg/ml; DM, 1x). B) Most contrast image from A) magnified at the site of the urinary system. C) Representative X-ray images of mice before and after injection of 200 µl 540 mg/ml DM (DM, 4x). D) Most contrast image from C) magnified at the site of the urinary system.

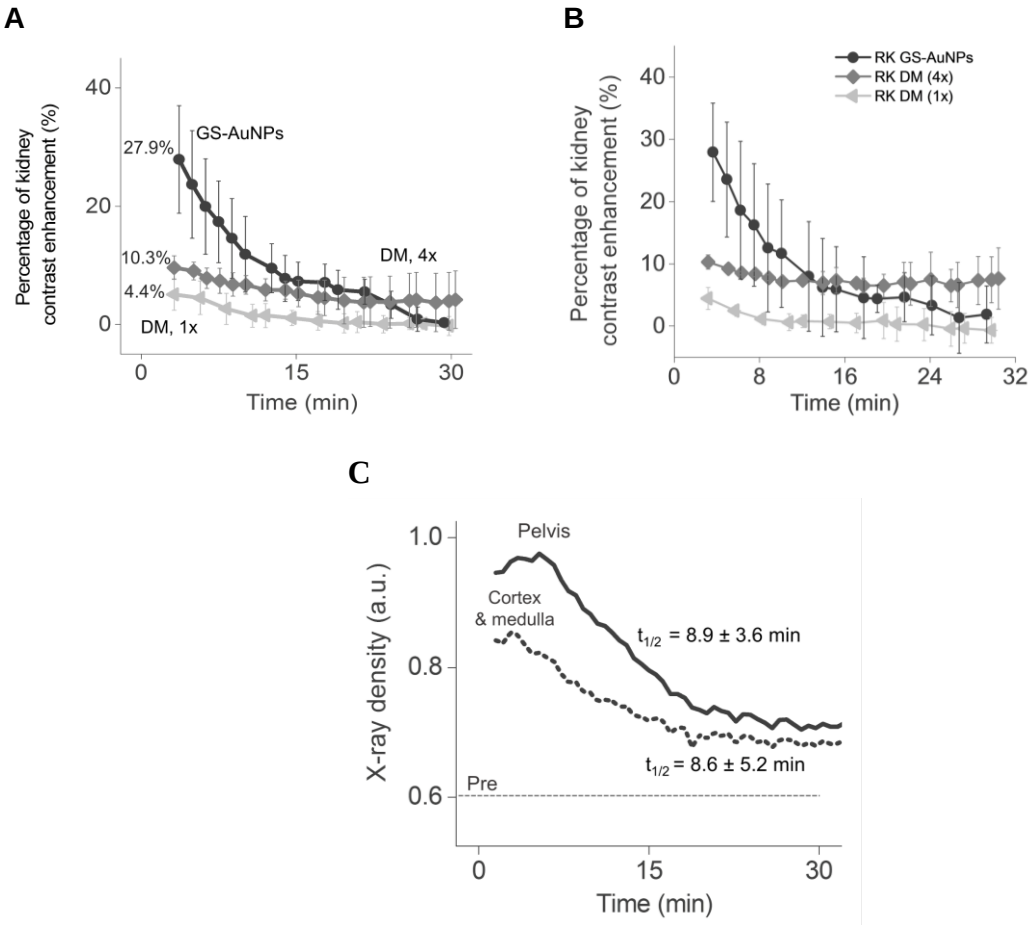

Figure 2.8. A) Percentage of contrast enhancement (%) of left kidney after intravenous injection of GS-AuNPs and DM. B) Right kidneys showed the same trend . C) Representative time-dependent X-ray density curves (TXDCs)

Table 2.4 Decay half-lives (min) of Time-dependent X-ray density curves (TXDCs) derived from the kidney area of normal CD-1 mice after receiving 1g/kg GS-AuNPs (N = 8).

Mouse #	M1	M2	M3	M4	M5	M6	M7	M8	M+SD[a]	$t_{1/2\text{-CM}}$[b]	$t_{1/2\text{-P}}$[c]
$t_{1/2\ RK\ CM}$	6.4	4.6	3	5.3	12.4	5.8	12.2	6.7	7.1 ± 3.3		
$t_{1/2\ LK\ CM}$	8.2	5.4	9.3	10.6	6.3	25.5	7.6	8.8	10.2 ± 6.4	8.6 ± 5.2	
$t_{1/2\ RK\ P}$	10.9	9.4	5.9	6.2	6.7	9.5	11.1	7.9	8.5 ± 2.1		8.9 ± 3.6
$t_{1/2\ LK\ P}$	10	7.4	8.9	5.6	4.1	19.9	11.2	8.2	9.4 ± 4.8		

RK, right kidney; LK, left kidney; CM, cortex and medulla; P, pelvis
[a] M ± SD: Mean ± Stand
[b] $t_{1/2\ CM}$: Average decay half-live of cortex and medulla in both left and right kidneys.
[c] $t_{1/2\ P}$: Average decay half-live of pelvis in both left and right kidneys.

2.3.5 Clearance kinetics of GS-AuNPs from kidney components in normal CD-1 mice

The clearance kinetics of GS-AuNPs from renal cortex and medulla to pelvis (nephrographic phase) and from pelvis to ureter (pyelographic phase)[13] were analyzed by comparing the decay half-lives of the time-dependent X-ray density curves (TXDCs) derived from both kidneys, which were 8.6 ± 5.2 min and 8.9 ± 3.6 min for corticomedullary area and pelvic area, respectively ($N=8$, $P>0.05$; Figure 2.8C and Table 2.4). No significant differences in the decay half-lives suggested that GS-AuNPs have no strong interactions with specific components of the urinary system in normal mice.[13-14]

2.3.6 Different clearance kinetics in diseased kidney induced by unilateral ureteral obstruction

To quantitatively understand how the renal disease affects the transport of GS-AuNPs through kidneys, we established a well-known kidney injury model, unilateral ureteral obstruction (UUO) model, where the left ureter was ligated and tubular injury was induced in the left kidney while the right kidney remained intact (Figure 2.9A).[10b] As control, the left ureter was exposed but not ligated in the sham-operated group. One day after operation, UUO and contralateral kidneys showed distinct accumulation and transport kinetics of GS-AuNPs (Figure 2.9B). The two elimination phases, nephrographic phase and pyelographic phase, were no longer distinguishable in the left UUO kidney while these two phases were still clearly visualized in the unobstructed right kidney (Figure 2.9B).

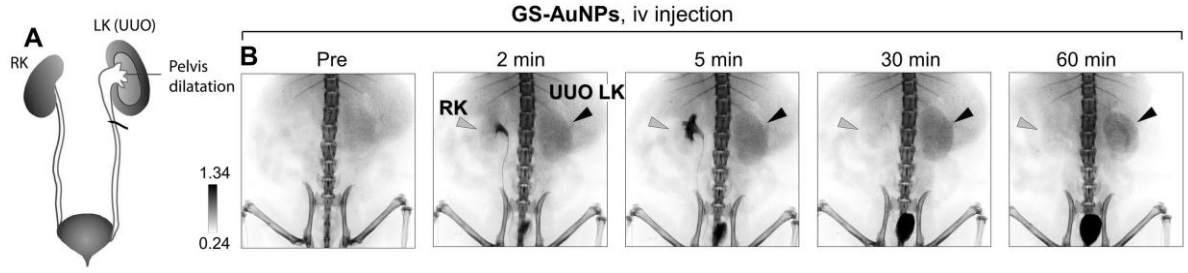

Figure 2.9. A) A scheme showing the unilateral ureteral obstruction (UUO) mice model by complete ligating of left ureter. RK, right kidney; LK, left kidney. B) Representative X-ray images of the urinary system in UUO mice before and after intravenous injection of GS-AuNPs.

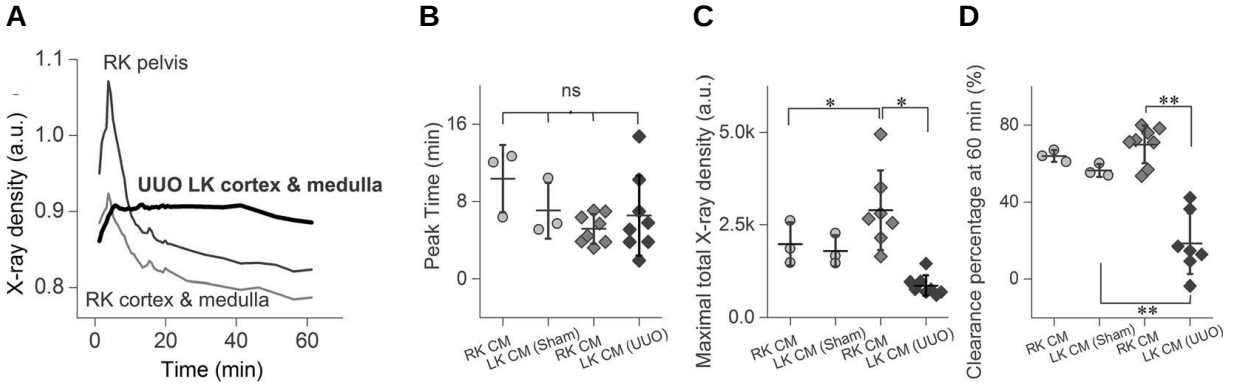

Figure 2.10. A) Representative TXDCs derived from cortex and medulla in obstructed left kidney (UUO LK), and cortex, medulla and pelvis in contralateral right kidney in UUO mice. B) Statistical analysis of peak time, C) maximal total X-ray density, and D) clearance percentage at 60 min of cortex and medulla (CM) in kidneys in UUO mice (diamond shape) and sham-operated mice (round shape). "ns", no significant difference; *P<0.05, **P<0.01.

For the UUO kidney, the accumulation of GS-AuNPs in the renal cortex and medulla reached the maximum at 6.5 ± 4.2 min (Figure 2.10A&B), statistically comparable to the time points in contralateral right kidneys (5.2 ± 1.5 min) and sham kidneys (8.7 ± 3.4 min) (P>0.05; Table 2.5). This indicated that the transport of GS-AuNPs from bloodstream to glomeruli in renal cortex was not significantly delayed in the obstructed kidney even though less GS-AuNPs entered into the diseased kidney due to reduced blood perfusion. The maximal total X-ray density (=average X-

ray density times area of kidney) of the UUO left kidney (859.0 ± 253.3) was significantly less than those of contralateral right kidney (2893.3 ± 1074.3) and left kidney (1795.0 ± 420.2) in sham mice ($P<0.05$; Figure 2.10C and Table 2.6). On the other hand, the elimination of GS-AuNPs from the renal cortex and medulla into the pelvis was significantly slowed down in the obstructed kidney.

Table 2.5. Decay half-lives (min) and peak time (min) of Time-dependent X-ray density curves derived from the kidney area of sham and UUO mice after receiving 1g/kg GS-AuNPs

Mouse #	**$t_{1/2\ RK\ CM}$**	**$t_{1/2\ LK\ (Sham)\ CM}$**	**$t_{1/2\ RK\ P}$**	**Peak time (RK)**	**Peak time (Sham LK)**
Sham 1	17.8	16.9	13.0	12.7	5.7
Sham 2	16.9	3.1	14.3	12.1	10.4
Sham 3	5.5	4.8	5.8	6.4	5.1
M ± SD	13.4 ± 6.9[a]	8.3 ± 7.5[a]	11.9 ± 5.6[a]	10.4 ± 3.4[a]	7.1 ± 2.9[a]
	Average of RK and LK: 10.8 ± 7.0			Average of RK and LK: 8.7 ± 3.4	
	$t_{1/2\ RK\ CM}$	**$t_{1/2\ LK\ (UUO)\ CM}$**	**$t_{1/2\ RK\ P}$**	**Peak time (RK)**	**Peak time (UUO LK)**
UUO (Rep) [b]	8.3		5.7	3.2	14.8
UUO 1	7.5		6.7	5.7	7.0
UUO 2[c]				3.4	5.8
UUO 3	10.5		15.2	7.1	10.3
UUO 4	20.6		14.1	6.3	3.8
UUO 5	20.8		16.2	3.8	5.1
UUO 6	7.8		3.0	7.0	3.8
UUO 7	7.9		8.5	4.4	1.9
M ± SD	11.9 ± 6.1[c]		9.9 ± 5.2[c]	5.2 ± 1.5	6.5 ± 4.2

(TXDCs) of UUO sham mice.

a] T-test was conducted between ″$t_{1/2\ RK\ CM}$″ and ″$t_{1/2\ LK\ (Sham)\ CM}$″ , ″Peak time (RK)″ and ″Peak time (LK)″, respectively. The results indicated no significant difference. ($P > 0.05$)

[b] UUO (Rep): Representative UUO mouse whose X-ray images and time-dependent X-ray density curves was presented in the manuscript

[c] Additional peak appeared in the time-dependent X-ray density curve of UUO 2.

Table 2.6. Two parameters, maximal total X-ray density and percentage (%) clearance at 60 min, extracted from time-dependent X-ray density curves of UUO group (N = 8) and sham group (N = 3). LK, left kidney; RK, right kidney; CM, cortex and medulla area; P, pelvic area. These data were used to plot Figure 2.10 C-D and Figure 2.15.

		Maximal total X-ray density (a.u.; CM)	% Clearance at 60 min[c] (CM)	%RRF[d]
Sham 1	RK	1467.76	72.03	55.50
	LK (Sham)	1653.98	66.91	44.50
Sham 2	RK	2614.96	73.30	51.83
	LK (Sham)	2267.54	63.92	48.17
Sham 3	RK	1852.83	59.14	54.90
	LK (Sham)	1463.472	60.90	45.10
M ± SD	RK	1978.52 ± 583.83	68.17 ± 7.84	54.08 ± 1.97
	LK (Sham)	1794.99 ± 420.17	63.91 ± 3.01	45.92 ± 1.97
UUO (Rep)	RK	3499.96	76.05	70.65
	LK (UUO)	1446.94	14.72	29.34
UUO 1	RK	4953.04	71.32	82.53
	LK[a] (UUO)	689.35	~~-40.87~~	17.47
UUO 2	RK	2144.65	56.78	70.65
	LK (UUO)	966.98	42.14	29.35
UUO 3	RK[b]	~~7645.55~~	79.99	88.65
	LK (UUO)	2802.96	9.30	11.35
UUO 4	RK	756.40	70.91	75.01
	LK (UUO)	685.96	-3.44	24.99
UUO 5	RK	2662.5	72.12	71.54
	LK (UUO)	764.63	17.09	28.46
UUO 6	RK	1638.31	53.50	67.71
	LK (UUO)	599.87	12.84	32.29
UUO 7	RK	2551.73	78.42	71.08
	LK (UUO)	961.79	36.34	28.91
M ± SD	RK	2893.31 ± 1074.26	69.89 ± 9.72	74.91 ± 7.07
	LK (UUO)	858.99 ± 253.28	18.43 ± 15.77 22.07 ± 13.66 (without UUO 4)	25.09 ± 7.07

[a] Maximal total X-ray density of cortex and medulla in contralateral right kidney in UUO 3 was determined to be an outlier according to Q-test.

[b] % Clearance at 60 min of cortex and medulla of left kidney in UUO 1 was determined to be an outlier according to Q-test.

[c] % Clearance at 60 min = [(maximal total X-ray density – total X-ray density at 60 min) / maximal total X-ray density] ×100%.[10b]

[d] % RRF: percentage of relative renal function = [maximal X-ray density of LK or RK / (maximal X-ray density of LK + maximal X-ray density of RK)] ×100%.[10b]

For normal kidneys in sham mice and UUO model (unobstructed right kidney), X-ray density of cortex and medulla exhibited a sharp decay after 5-9 min with half-lives of 11.0 ± 6.9 min and 10.8 ± 7.0 min, respectively, representing efficient clearance of the GS-AuNPs from the cortex and medulla into the pelvis (Table 2.5) and nearly 65-70% of GS-AuNPs cleared out of the kidneys at 60 min p.i. (Figure 2.10D and Table 2.5).In contrast, the UUO kidneys generally showed no obvious clearance of particles from the cortex and medulla despite variation among the mice. One UUO kidney exhibited no clearance at all during 0-60 min p.i., and only an average of 22.1 ±13.7% of GS-AuNPs was cleared out of the kidneys in the other seven UUO kidneys, just one third of the value of normal kidneys (Figure 2.10D and Table 2.6).

2.3.7 UUO induced retention and distribution of GS-AuNPs in kidney components

The delayed clearance of GS-AuNPs from the injured kidneys altered the interaction between NPs and kidney cells. As shown in the X-ray image of the UUO kidney at 60 min p.i., GS-AuNPs were selectively retained on the interface between the pelvis and medulla while the contralateral kidney showed very low X-ray density at the same time point (Figure 2.11A). To further understand this selective accumulation of GS-AuNPs in UUO kidney, we conducted histological studies on both normal and obstructed kidneys with H&E staining and silver staining (Figure 2.11B). In unobstructed contralateral kidneys, even though the kidneys have been exposed to a large amount of GS-AuNPs, the kidney tissue remained normal and GS-AuNPs were mainly accumulated in the cortex at 1 h p.i. (Figure 2.12A). For UUO mice on Day 1 post operation, while glomeruli and proximal tubules in the cortex remained normal and contained particles (Figure 2.11B&2.12B), extensive tubular dilatation and atrophy were found on the boundary of pelvis and medulla, where

transport of GS-AuNPs was interrupted and NPs were retained in the tubular lumen (1 h p.i.; Figure 2.13). These results indicated that the slow transport of GS-AuNPs within the damaged medulla caused the unique distribution of GS-AuNPs in the UUO kidney.

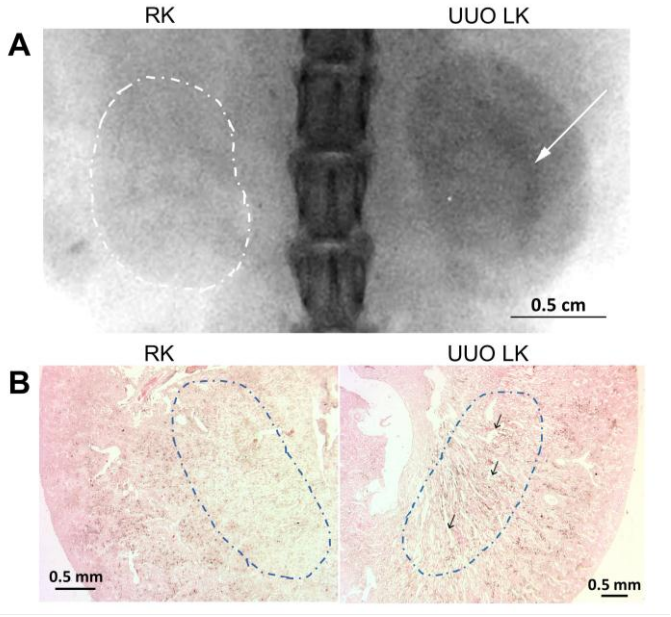

Figure 2.11. A) *In vivo* X-ray image of kidneys of 1 day UUO mouse taken at 60 min p.i. of GS-AuNPs zoomed in at kidney area. Arrow indicated the area where NPs were selectively retained, and dash line indicated contralateral kidney. B) H&E and silver-stained section from UUO kidney and contralateral kidney shown in panel *A* which were harvested right after 60-min dynamic X-ray imaging. Dash circles indicated medullary area; arrows pointed to the dilated tubules where large amount of GS-AuNPs were accumulated.

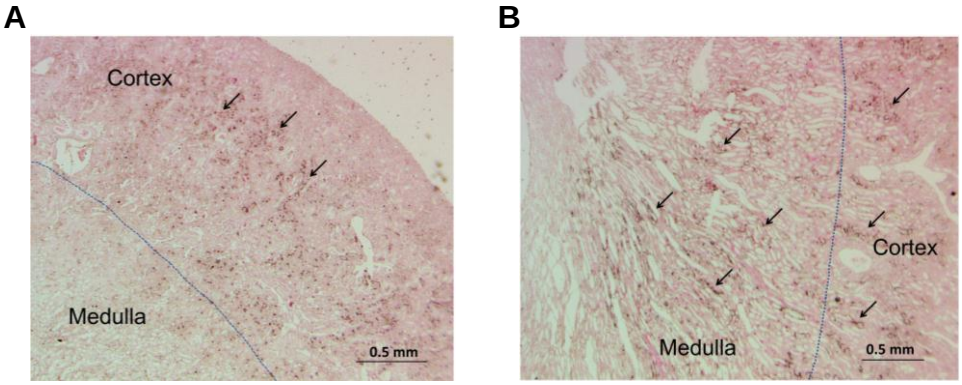

Figure 2.12. Zoomed-in images of Figure 2.11B. A) contralateral kidney, and B) UUO kidney. Arrow pointed to NPs accumulation; dash divided cortex and medulla in kidneys.

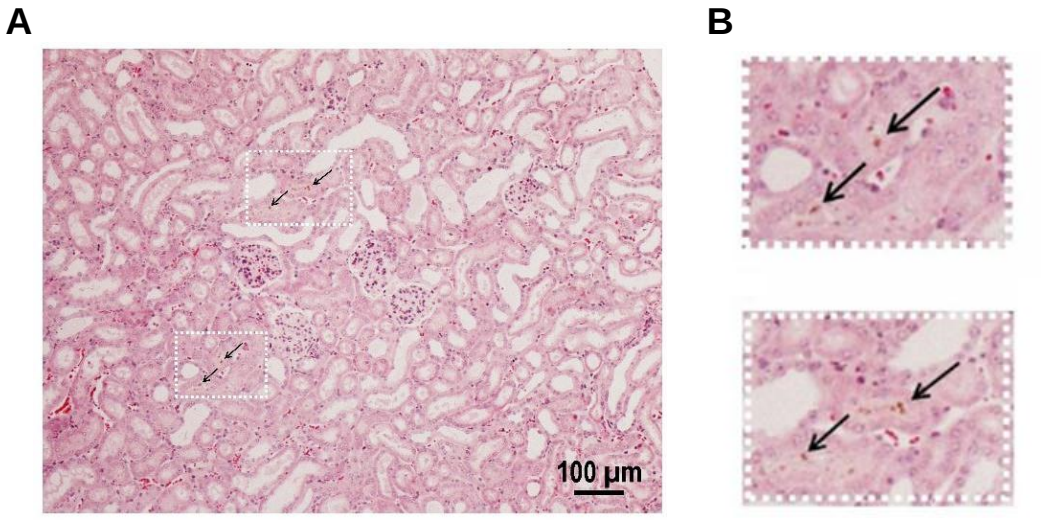

Figure 2.13. A) H&E stained tissue section from UUO kidneys at the first day post obstruction operation (dashed square indicates accumulation of GS-AuNPs in tubular lumen. B) Enlarged images showing GS-AuNPs in tubular lumen (arrows indicate GS-AuNPs).

On Day 8 post operation when tubular dilatation and atrophy were more pronounced (Figure 2.14A), some AuNPs appeared inside the normal tubular epithelial cells at the junction of the cortex and medulla, right below in medullary area where extensive tubular impairment was spotted (Figure 2.14B). These results indicate that the tubular cells started to internalize GS-AuNPs that could not be eliminated. Therefore, pathological change of kidneys not just altered the distribution pattern of GS-AuNPs but also changes their interaction with kidneys at the cellular level.

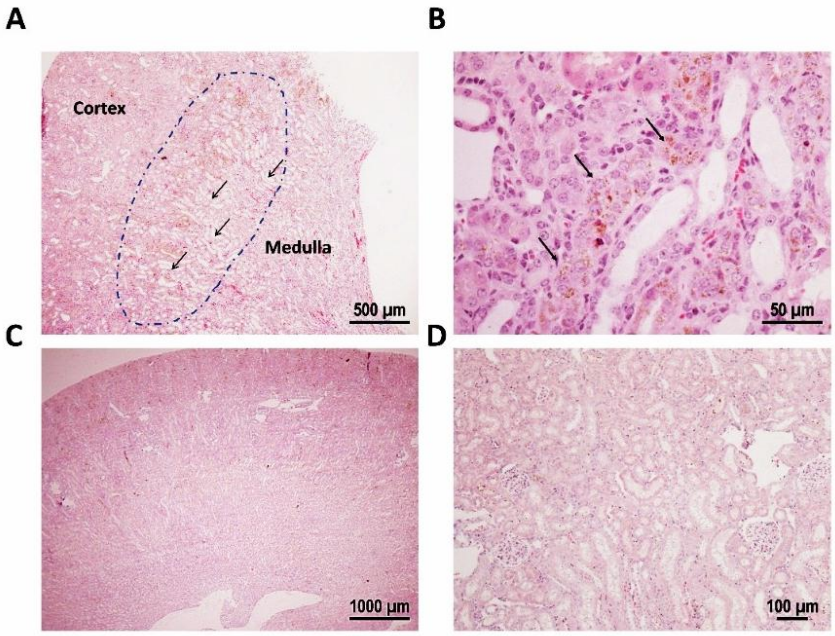

Figure 2.14. H&E stained tissue section from UUO and contralateral kidneys harvested on the eighth day post operation. A) UUO kidney (dash indicates accumulation of GS-AuNPs in medullary area; arrows indicate tubular dilatation and atrophy). B) Enlarged image of UUO kidney showing GS-AuNPs in tubular epithelial cells (arrows indicate GS-AuNPs). C, D) Images of contralateral kidney in the same mouse.

2.4 Conclusion

In summary, noninvasive dynamic X-ray imaging of renal clearance of GS-AuNPs allowed us to obtain quantitative understanding of NP transport and nano-bio interactions *in vivo* in normal and injured kidneys. High contrast in the X-ray imaging of GS-AuNPs is not just because gold atom has a large X-ray attenuation coefficient, but also because GS-AuNPs have longer retention in the kidneys compared to iodine agents. Assisted by X-ray imaging, we found that in normal mice renal clearable AuNPs had uninterrupted transport in different components of the urinary system, which all follows a simple one-component exponential decay with comparable kinetics. However, in the kidney with unilateral ureteral obstruction, the transport of renal clearable AuNPs from the cortex

and medulla into the pelvis was significantly slowed down because of the dilatation and atrophy in the medulla. Moreover, high-penetration depth and high-spatial resolution of X-ray imaging allowed us to precisely locate impairments noninvasively and correlate the injury with the changes in peak time, maximum total X-ray density, clearance percentage at 60 min and relative renal function (%RRF) (Figure 2.15).

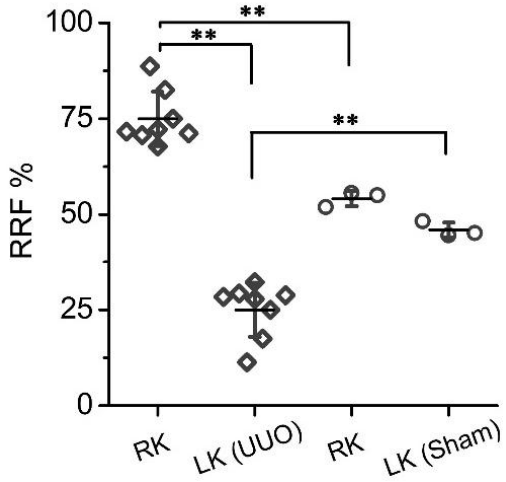

Figure 2.15. Relative renal function (%RRF) for the cortex and medulla in kidneys in UUO mice and sham-operated mice (N = 8 for the UUO group and N = 3 for the sham group.) %RRF = [peak value of LK or RK / (peak value of LK + peak value of RK)] ×100%).

Together with our ongoing studies on the correlation of kidney clearance kinetics of GS-AuNPs with glomerular filtration rate,[15] these new findings not only advance our fundamental understandings of NP transport in normal and injured kidneys but also further broaden renal clearable AuNPs in the kidney functional evaluation at an anatomical level.

2.5 Acknowledgements

This work was supported by the NIH (1R01DK103363), CPRIT (RP140544 and RP160866), and a start-up fund from The University of Texas at Dallas (J.Z.).

2.6 Authors Contributions

Jing Xu performed all the *in vitro* and *in vivo* experiments. Phoebe Carter synthesized the GS-AuNPs. Elizabeth Hernandez and Andrew Dang constructed the unilateral ureteral obstruction models. Jing Xu, Mengxiao Yu, Payal Kapur, Jer-Tsong Hsieh and Jie Zheng reviewed, analyzed and interpreted the data. Jing Xu, Mengxiao Yu and Jie Zheng wrote the paper. All authors discussed the results and commented on the manuscript.

2.7 References

[1] K. M. Tsoi, S. A. MacParland, X.-Z. Ma, V. N. Spetzler, J. Echeverri, B. Ouyang, S. M. Fadel, E. A. Sykes, N. Goldaracena, J. M. Kaths, J. B. Conneely, B. A. Alman, M. Selzner, M. A. Ostrowski, O. A. Adeyi, A. Zilman, I. D. McGilvray, W. C. W. Chan, *Nature Materials* **2016**, *15*, 1212-1221.

[2] a) S. Wilhelm, A. J. Tavares, Q. Dai, S. Ohta, J. Audet, H. F. Dvorak, W. C. Chan, *Nature Reviews Materials* **2016**, *1*, 16014; b) D. Dehaini, R. H. Fang, B. T. Luk, Z. Pang, C.-M. J. Hu, A. V. Kroll, C. L. Yu, W. Gao, L. Zhang, *Nanoscale* **2016**, *8*, 14411-14419; c) R. Mo, Z. Gu, Materials Today 2016, 19, 274-283; d) M. Yu, C. Zhou, L. Liu, S. Zhang, S. Sun, J. D. Hankins, X. Sun, J. Zheng, *Angewandte Chemie International Edition* **2017**, *56*, 4314-4319.

[3] a) N. Kamaly, J. C. He, D. A. Ausiello, O. C. Farokhzad, *Nature Reviews Nephrology* **2016**, *12*, 738-753; b) D. A. Jasim, S. Murphy, L. Newman, A. Mironov, E. Prestat, J. McCaffrey, C. Ménard-Moyon, A. F. Rodrigues, A. Bianco, S. Haigh, R. Lennon, K. Kostarelos, *ACS Nano* **2016**, *10*, 10753-10767; c) X. Liang, H. Wang, Y. Zhu, R. Zhang, V. C. Cogger, X. Liu, Z. P. Xu, J. E. Grice, M. S. Roberts, *ACS Nano* **2016**, *10*, 387-395; d) A. V. Nair, E. J. Keliher, A. B. Core, D. Brown, R. Weissleder, *ACS Nano* **2015**, *9*, 3641-3653.

[4] H. Soo Choi, W. Liu, P. Misra, E. Tanaka, J. P. Zimmer, B. Itty Ipe, M. G. Bawendi, J. V. Frangioni, *Nature Biotechnology* **2007**, *25*, 1165-1170.

[5] H. S. Choi, W. Liu, F. Liu, K. Nasr, P. Misra, M. G. Bawendi, J. V. Frangioni, *Nature Nanotechnology* **2010**, *5*, 42-47.

[6] A. A. Burns, J. Vider, H. Ow, E. Herz, O. Penate-Medina, M. Baumgart, S. M. Larson, U. Wiesner, M. Bradbury, *Nano letters* **2008**, *9*, 442-448.

[7] E. Phillips, O. Penate-Medina, P. B. Zanzonico, R. D. Carvajal, P. Mohan, Y. Ye, J. Humm, M. Gönen, H. Kalaigian, H. Schöder, H. W. Strauss, S. M. Larson, U. Wiesner, M. S. Bradbury, *Science Translational Medicine* **2014**, *6*, 260ra149-260ra149.

[8] C. Zhou, M. Long, Y. Qin, X. Sun, J. Zheng, *Angewandte Chemie International Edition* **2011**, *50*, 3168-3172.

[9] a) M. Yu, J. Zheng, ACS Nano 2015, 9, 6655-6674; b) C. Peng, X. Gao, J. Xu, B. Du, X. Ning, S. Tang, R. M. Bachoo, M. Yu, W.-P. Ge, J. Zheng, *Nano Research* **2017**, *10*, 1366-1376; c) J. Liu, M. Yu, C. Zhou, S. Yang, X. Ning, J. Zheng, *Journal of the American Chemical Society* **2013**, *135*, 4978-4981.

[10] a) M. Yu, J. Liu, X. Ning, J. Zheng, *Angewandte Chemie International Edition* **2015**, *54*, 15434-15438; b) M. Yu, J. Zhou, B. Du, X. Ning, C. Authement, L. Gandee, P. Kapur, J.-T. Hsieh, J. Zheng, *Angewandte Chemie International Edition* **2016**, *55*, 2787-2791.

[11] a) H. Chen, G. D. Wang, W. Tang, T. Todd, Z. Zhen, C. Tsang, K. Hekmatyar, T. Cowger, R. B. Hubbard, W. Zhang, J. Stickney, B. Shen, J. Xie, *Advanced Materials* **2014**, *26*, 6761-6766; b) J. Huang, L. Wang, X. Zhong, Y. Li, L. Yang, H. Mao, *Journal of Materials Chemistry B* **2014**, *2*, 5344-5351.

[12] J. Hainfeld, D. Slatkin, T. Focella, H. Smilowitz, *The British journal of radiology* **2006**, *79*, 248-253

[13] E. A. Wolin, D. S. Hartman, J. R. Olson, *American Journal of Roentgenology* **2013**, *200*, 1210-1214.

[14] R. B. Dyer, M. Y. Chen, R. J. Zagoria, *Radiographics* **2001**, *21*, 799-824.

[15] M. Ikeda, R. Wakasaki, K. J. Schenning, T. Swide, J. H. Lee,M. B. Miller, H. S. Choi, S. Anderson, M. P. Hutchens *American Journal of Physiology-Renal Physiology*, **2017**, *312*: F629–F639.

[16] J. Liu, P. N. Duchesne, M. Yu, X. Jiang, X. Ning, R. D. Vinluan, P. Zhang, J. Zheng, *Angewandte Chemie International Edition* **2016**, *55*, 8894-8898.

CHAPTER 3

DOSE DEPENDENCIES AND BIOCOMPATIBILITY OF RENAL CLEARABLE GOLD NANOPARTICLES: FROM MICE TO NON-HUMAN PRIMATES

Authors-Jing Xu[+†], Mengxiao Yu[+†], Chuanqi Peng[†], Phoebe Carter[†], Jia Tian[‡], Xuhui Ning[†], Qinhan Zhou[†], Qiu Tu[ł], Greg Zhang[†], Anthony Dao[†], Xingya Jiang[†], Payal Kapur[#], Jer-Tsong[§] Hsieh, Xudong Zhao[ł], Pengyu Liu[‡], and Jie Zheng[†]*

[†]Department of Chemistry and Biochemistry, BE 26

The University of Texas at Dallas

800 West Campbell Road, Richardson, Texas USA 75080

·[§]Department of Urology and [#]Department of Pathology

The University of Texas Southwestern Medical Center

5323 Harry Hines Blvd., Dallas, TX 75390 (USA)

[‡]General Research Institute for Nonferrous Metals

2 Xinjiekou Outer St., Beijing, 100088 (China)

[ł]Kunming Institute of Zoology, Chinese Academy of Sciences

32 Jiaochang Donglu, Kunming, 650223 (China)

"+" These authors contributed equally

Reprinted (adapted) with permission from J. Xu, and M. Yu, et al., *Angewandte Chemie International Edition* **2018**, *57*, 266-271.

Abstract

While dose dependencies in pharmacokinetics and clearance are often observed in clinically used small molecules, very few studies have been dedicated to the understandings of potential dose-dependent *in vivo* transport of nanomedicines. Here we report that the pharmacokinetics and clearance of renal clearable gold nanoparticles (GS-AuNPs) are strongly dose-dependent once injection doses are above 15 mg/kg: high dose expedited the renal excretion and shortened the blood retention. As a result, the no-observed-adverse-effect-level (NOAEL) of GS-AuNPs was >1000 mg/kg in CD-1 mice. The efficient renal clearance and high compatibility can be translated to non-human primates: no adverse effects were observed within 90 days after intravenous injection of 250 mg/kg GS-AuNPs. These fundamental understandings of dose effect on the *in vivo* transport of ultrasmall AuNPs open up a pathway to maximize their biomedical potential and minimize their toxicity in future clinical translation.

3.1 Introduction

Fundamental understandings of dose-dependencies in pharmacokinetics (PK) and clearance of imaging agents[1] and therapeutic drugs[2] are key to maximizing their potential and minimizing their toxicity in the clinic.[3] Many small molecules have shown strong dose-dependent PK and clearance in both animal models and patients.[4] For example, increasing dose of mezlocillin from 20 mg/kg to 200 mg/kg resulted in a 50% decrease in plasma clearance due to saturation of both biliary and renal excretion pathway.[4b] In contrast, MK-826, another small-molecule drug, exhibited 5-times faster plasma clearance when dose increased from 10 to 180 mg/kg because of concentration-dependent protein binding.[4a] Dose-dependent clearance was also observed from large PEGylated liposomal doxorubicin (Doxil): an 8-fold enhancement in dose from 2.5 to 20 mg/kg led to a 15-fold increase in plasma concentration, suggesting prolonged blood circulation at high doses.[5] Although dose-dependencies have been well recognized in small drug molecules, they are still largely unknown for engineered nanoparticles (NPs), which is partially because engineered NPs often severely accumulate in the reticuloendothelial system, limiting their clinical translation.[5,6] However, with the emergence of more and more renal clearable NPs that can behave like small drug molecules and be rapidly removed from the body through the urinary system[6c,7], systematic investigations of whether and how injection doses affect their pharmacokinetics and clearance become extremely critical to both fundamental understanding of their *in vivo* transport and future clinical translation.

Unlike many renal-clearable engineered NPs such as quantum dots[6c] and silica NPs[7b], which are rapidly eliminated out of the body within a few hours, renal clearable gold nanoparticles (AuNPs) exhibit relatively slower elimination and have much longer blood retention. Within 24 h, only 50%

of the 2 nm glutathione-coated AuNPs (GS-AuNPs) were excreted in the urine.[7c] The slow clearance of the AuNPs fundamentally originates from the density-dependent margination of engineered NPs in the laminar blood flow: the high-density AuNPs tend to marginate toward the blood vessel walls more quickly and be transported in the laminar blood flow more slowly than similar-sized low-density NPs.[8] While the slow clearance renders the AuNPs unique capabilities of passive tumor targeting through the enhanced permeability and retention (EPR) effect[9] and noninvasive fluorescence imaging of kidney dysfunction for a long period of time,[10] some critical questions regarding their future clinical translation are also naturally raised: (1) whether margination effect of the renal clearable AuNPs will result in any dose-dependent PK and clearance in the laminar blood flow; (2) whether the prolonged blood retention will induce any toxicity, in particular, any damage to the kidneys at high doses; and (3) whether efficient renal clearance of the AuNPs observed in mice can be translated to non-human primates, the first step towards the clinical translation of renal clearable AuNPs.

Herein, we report that strong dose-dependent PK and renal clearance of GS-AuNPs were observed once the doses was above 15 mg/kg: the higher dose resulted in more rapid renal clearance. Owing to the unique dose-dependent transport and clearance, no damage was observed on the glomerular filtration barrier of CD-1 mice even at a dose of 1059 mg/kg, higher than the maximum tolerated dose (MTD) of the highly biocompatible silica NPs (450 mg/kg, core size of 115 nm).[11] Furthermore, the efficient renal clearance and high biocompatibility of GS-AuNPs observed in mice can also be translated to monkeys, indicating a great potential in translating renal clearable AuNPs into the clinic.

3.2 Materials and Methods

3.2.1 Materials and equipment

Hydrogen tetrachloroaurate ($HAuCl_4$) was purchased from Fisher Scientific (Waltham, MA, USA). All the other chemicals were purchased from Sigma-Aldrich.

Absorption spectra were collected using a Varian 50 Bio UV-Vis spectrophotometer. Luminescence spectra were collected using a PTI QuantaMasterTM 30 Fluorescence Spectrophotometer (Birmingham, NJ, USA). Gold concentrations in mouse samples were measured by ICP-MS (Agilent 7900). TEM images of kidney tissues were obtained using a Tecnai™ G2 Spirit transmission electron microscope at The Electron Microscopy Core Facility at the University of Texas Southwestern Medical Center (UTSW). Transmission electron microscopy (TEM) images of gold nanoparticles were obtained with JEM-2010 transmission electron microscope. Gold concentrations in monkey samples were measured by inductively coupled plasma atomic emission spectroscopy (ICP-AES, Agilent 725) and ICP-MS (Agilent 7700). Fourier transform-infrared (FTIR) spectra were obtained from an Agilent Cary 660 FTIR Spectrometer. The complete blood count of monkey samples was performed using an automated hematology analyzer HEMAVET 950 (Drew Scientific, Inc.) Serum biochemistry of monkey samples was performed using an automated biochemistry analyzer Dimension EXL 200 (Siemens Healthcare Diagnostics, Inc.). Urinary analysis results of the monkey samples were obtained from urine analyzer Uritest-200B (Guilin Medical Electronic Instrument Factory).

3.2.2 Methods

GS-AuNPs Synthesis

The near-infrared-emitting GS-AuNPs were synthesized according to our previous work.[9c] Basically, 1 M HAuCl4 solution was added to 2.4 mM glutathione aqueous solution at a molar ratio 1:0.8. The mixture was then heated at 95 ℃ in an oil both. The resulting solution was cooled down to room temperature and centrifuged to remove the aggregates, followed by adding ethanol to precipitate GS-AuNPs. The pellet of GS-AuNPs was then suspended in PBS solution which was further centrifuged. The supernatant was then purified by dialysis. For monkey study, ~2.5 gram of GS-AuNPs were synthesized by repeating the above procedure, and all the obtained samples were mixed, freeze dried and kept at -20 ^{o}C.

Mouse studies.

All mouse studies were performed according to the guidelines of the University of Texas System Institutional Animal Care and Use Committee. The mouse models were female CD-1 mice (8-10 weeks old, ~26 g) that were purchased from Envigo Corporation. The animals were housed in ventilated cages under standard environmental conditions (23 ± 1 ^{o}C, 50 ± 5 % humidity and a 12/12 h light/dark cycle) with free access to water and standard laboratory food.

Renal clearance of GS-AuNPs: Twenty-seven CD-1 mice were divided into nine groups (N = 3 for each group) and intravenously injected with 200 μL PBS containing GS-AuNPs at nine different doses (0.15, 1.5, 5.8, 10.2, 15, 183, 365, 693 and 1059 mg/kg), respectively. Urine was collected at 2 h and 24 h post injection. Au amount in urine was quantified by ICP-MS.

The dose range of 0.15~1059 mg/kg was selected based on the minimum detection limit of ICP-MS and maximum solubility of GS-AuNPs in PBS. We used 200 μl PBS solution containing

different amounts of GS-AuNPs (different doses) for injection so as to rule out the effect of injection volume. The maximum dose at 1059 mg/kg corresponds to a concentration at 145 mg/ml. The concentration of GS-AuNPs at 145 mg/ml approaches their maximum solubility in PBS, as suggested by that after staying at room temperature for 2 h, a very small amount of NPs precipitated from the solution at high-speed centrifugation. This indicated that 1059 mg/kg was the maximum dose we can investigate currently without increasing the injection volume.

Measurement of renal function markers (BUN and sCr), biodistribution study of GS-AuNPs and pathological analysis: Twenty-four CD-1 mice were divided into six groups (N=4 for each group) and intravenously injected with 200 μL PBS or 200 μL PBS containing GS-AuNPs at five different doses (15, 183, 365, 693 and 1059 mg/kg), respectively. Renal function biomarkers, blood urea nitrogen (BUN) and serum creatinine (sCr), were measured on 1, 4, 7, 10 and 14 days post injection. Body weight of each mouse was monitored daily as an indicator of systemic toxicity. Mice were sacrificed at the 14th day post injection; organs were harvested and prepared for both histopathological examination and Au amount quantification. Organs (kidneys, liver, spleen and lung) for histopathological examination were fixed and preserved using 10% formaldehyde neutral buffered solution. The tissue sections were stained by Harris hematoxylin and erosin and analyzed by the pathologist in blind. Au amount in each organ was quantified after the organ was weighed. Inductively coupled plasma mass spectrometry (ICP-MS) was used to measure Au amount and results were presented in two ways, percentage of injected dose per gram of tissue (% ID/g) and Au amount per gram of tissue [Au (mg/g)].

Renal clearance of 70 kD dextran: Measurement of renal clearance of FITC-70 kD dextran followed a four-day procedure. On Day 1, each mouse (N = 3) was injected with 200 μL phosphate

buffered solution and urine was collected from each of them to measure the "Autofluorescence of urine". On Day 2, each mouse received 100 μL 2 mg/ml 70 FITC-kD dextran buffered solution through intravenous injection and urine was collected at 2, 5 and 8 h p.i. ("Control" with injection of PBS). On Day 3, 1059 mg/kg GS-AuNPs were intravenously injected into each mouse. At 24 h post injection (on Day 4), 100 μL 2 mg/ml 70 FITC-kD dextran was injected into each mouse in the same way as Day 2 and urine was collected at 2, 5 and 8 h p.i. ("GS-AuNPs"). All the samples was kept in dark at 4°C. Before measurement, each of the urine samples was diluted 10x by phosphate buffered solution and added into 96-well plate (200 μL for each well). The fluorescence intensity of wells were measured using a FLUOstar filter-based multi-mode microplate reader with excitation filters set as 485/12 nm and emission filter as 520 nm. The signals detected from urine collected at day one was used as the baseline signal.

Transmission electron microscopy (TEM) imaging of kidney: Two mice were used for the TEM study on integrity of glomerular filtration membranes. Both mice were injected with 1059 mg/kg GS-AuNPs and one was euthanized at 24 h post injection, the other was euthanized at 14 days post injection for short-term and long-term injury examination, respectively. Blood removal and fixative immersion were performed right after euthanizing in the UTSW molecular pathology core. Perfusant preparation and tissue sectioning were conducted by UTSW electron microscopy (EM) core facility. Four grids were prepared for one tissue block that contained tissues sectioned from different layers. The tissue grids were evaluated using a Tecnai™ G2 Spirit transmission electron microscope in the UTSW EM core facility. Approximately 5-6 areas were examined for each tissue grid and 3-4 glomeruli were imaged in each area.

Pharmacokinetics study: Nine mice were divided into three groups (N = 3 for each group) and intravenously injected with 15, 183 and 1059 mg/kg GS-AuNPs, respectively. Blood was collected from retro-orbital of each mouse at 2, 5, 10, 30 min, 1, 3, 5, 8, 12 and 24 h and the Au amount in each blood sample was quantified using ICP-MS. The Au amount was presented as percentage of injected dose per gram of blood (%ID/g). The pharmacokinetics (PK) parameters were calculated as follows, where V_d is volume of distribution, $t_{1/2\alpha}$ is distribution half-live, $t_{1/2\beta}$ is elimination half-life, CL is plasma clearance, C_0 is initial concentration, AUC is the area under the curve. (1) Au amount at each time point was plotted using OriginLab, where x was time and y was Au amount in blood (% ID/g), and fitted using two-compartment exponential decay ("ExpDec2", $y = A_1 * \exp(-x/t_1) + A_2 * \exp(-x/t_2) + y_0$).

(2) V_d, $t_{1/2\alpha}$, $t_{1/2\beta}$ and CL were calculated based on the following equations: [3c]

a. $C_0 = A_1 + A_2 + y_0$;

b. $V_d = 100/C0$;

c. $t_{1/2\,\alpha} = t1$

d. $t_{1/2\,\beta} = 0.693AUC/C_0$

e. $CL = 100/AUC$

24 h Biodistribution study: Fifteen mice were divided into five groups (N = 3 for each group) and intravenously injected with GS-AuNPs at five different doses (15, 183, 365, 693 and 1059 mg/kg), respectively. Mice were sacrificed at 24 h post injection; organs were harvested and prepared for Au amount quantification.

Monkey studies: All monkey studies were conducted at Kunming Institute of Zoology, Chinese Academy of Sciences, under a protocol approved by the Ethics Committee of Kunming Institute

of Zoology, Chinese Academy of Sciences. Six male cynomolgus monkeys (3 years old, 3~4 kg) were divided to two group (N=3 for each group): one group received single-dose injection of GS-AuNPs at 250 mg/kg body weight through intravenous drip; the other group without any treatment served as control. Urine and feces were collected from monkeys receiving GS-AuNPs at 3, 5, 8, 12, and 24 h after intravenous injection. Amounts of AuNPs in urine and feces were quantified by ICP-AES and ICP-MS. To study pharmacokinetics of GS-AuNPs, blood was collected at 2, 5, 10, 30 min, 1, 3, 5, 8, 12 and 24 h p.i. and Au concentration in blood was measured by ICP-AES and ICP-MS.

Extracting GS-AuNPs from urine: GS-AuNPs were extracted from urine collected at an early time point (<30 min post injection) that contained high-concentration AuNPs. Urine samples were centrifuged at 4500 RPM for 10 min, and then supernatant was purified using 10kD MW centrifugal filter unit. After centrifugation at 4500 RPM for 15 min, the AuNPs were kept inside the tube (MW > 10kD) and water can be filtered out. The AuNPs were washed with DI water for 3 times (centrifuged at 4500 RPM for 15 min). The solution inside the tube contained GS-AuNPs and was used for TEM imaging and measurement of absorption, emission and excitation spectra.

Biosafety assessment for 90 days: Body weights, temperatures and behaviors of all six animals were recorded once a week. At the same time, urine and fasting blood samples were collected and subjected to complete blood count, blood clotting tests, serum biochemistry analysis, and urine analysis.

3.3 Results and discussion

3.3.1 Dose-dependent renal clearance of GS-AuNPs

Near-infrared-emitting 2.5 nm GS-AuNPs were chosen for this study because of their great potential in cancer imaging[8,9,12] and kidney functional imaging.[10, 13] The synthesis and characterization of GS-AuNPs has been reported in our previous work.[9] We first intravenously injected GS-AuNPs into the CD-1 mice at nine doses ranging from 0.15 to 1059 mg/kg and measured the renal clearance efficiency in the early elimination stage (2 h p.i.). The renal clearance of GS-AuNPs was dose-independent at low doses from 0.15 to 15 mg/kg: the 2-h renal clearance efficiency remains constant at ~35 %ID (Figure 3.1A). However, with a dose increase from 15 to 183, 365, 693 and 1059 mg/kg, the 2-h renal clearance became linearly increased from 34.6 to 41.0, 47.9, 52.7 and 69.0 %ID (Figure 3.1B). The 24-h renal clearance showed the same trend as the results obtained at 2 h p.i. (Figure 3.2).

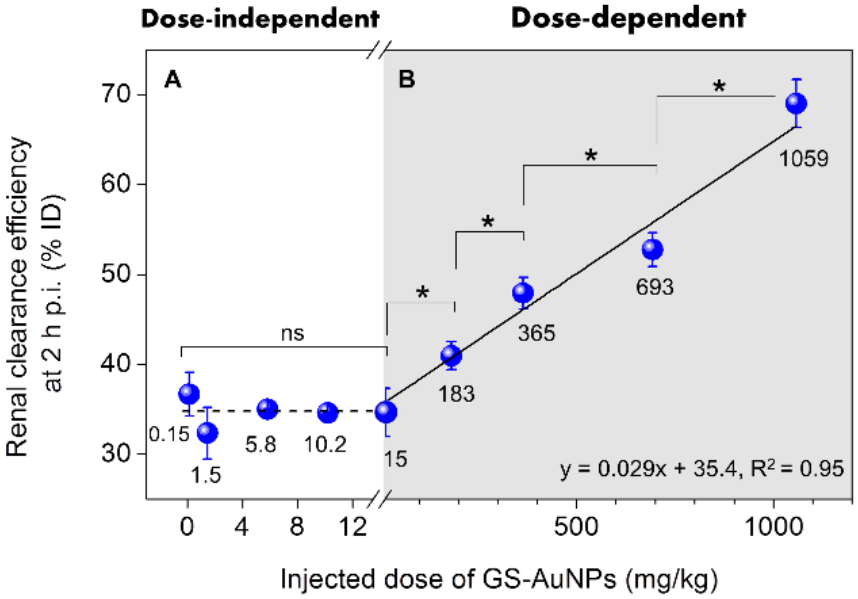

Figure 3.1. Dose effect on renal clearance of 2.5 nm glutathione-coated gold nanoparticles (GS-AuNPs) after intravenous injection in CD-1 mice. (A) The renal clearance efficiency at 2 h post injection was independent of injected dose at a low-dose range from 0.15 to 15 mg/kg, (B) but it

linearly increased from 34.6 to 69.0 % of injected dose (%ID) as dose increased from 15 to 1059 mg/kg (200 µL PBS solutions containing different amounts of NPs were injected; N = 3 for each group; *P < 0.05; ns, no significant difference, P > 0.05). For the injection doses at 5.8 and 10.2 mg/kg, the standard deviations of renal clearance efficiencies are too small to be seen clearly. The dose range of 0.15~1059 mg/kg was selected based on the minimum detection limit of ICP-MS and maximum solubility of GS-AuNPs in PBS.

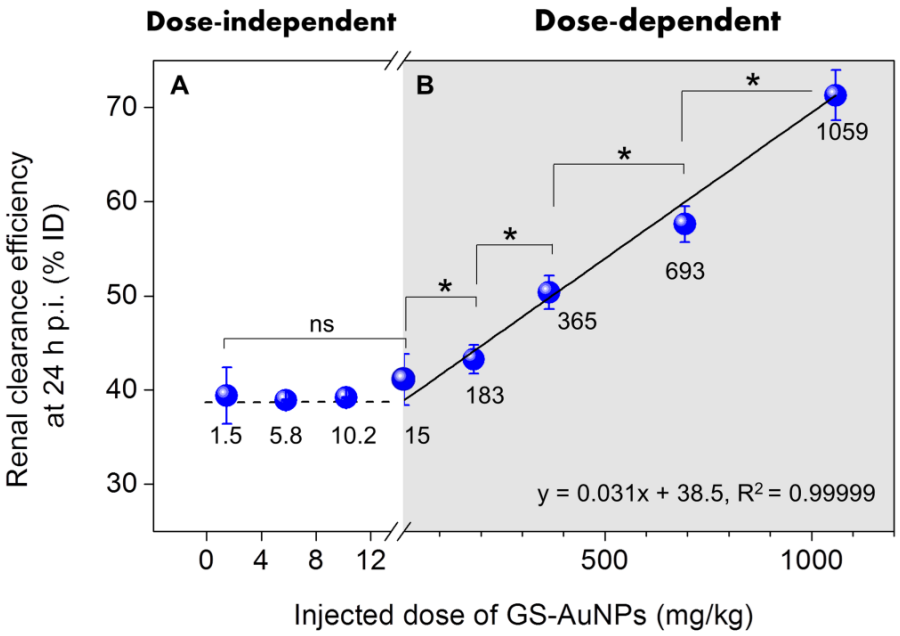

Figure 3.2. Dose effect on renal clearance of 2.5 nm glutathione-coated gold nanoparticles (GS-AuNPs) at 24 hours after intravenous injection. (A) The renal clearance efficiency at 24 h post injection was independent of injected dose at a low-dose range below 15 mg/k and remained constant of ~39 percentage of injected dose (%ID), (B) but it linearly increased from 38.9 to 43.3, 50.4, 57.6 and 71.3 %ID as dose increased from 15 to 183, 365, 693 and 1059 mg/kg (N = 3 for each group; *P < 0.05; ns, no significant difference, P > 0.05). The 24-h renal clearance efficiency at 0.15 mg/kg cannot be accurately measured because the Au concentrations in urine (collected after 2 h p.i.) are approaching the limit of detection for Au using ICP-MS. For the injection doses at 5.8 and 10.2 mg/kg, the standard deviations of renal clearance efficiencies are too small to be seen clearly.

3.3.2 Evaluation of kidney function and structure after exposing to GS-AuNPs

To unravel whether the enhanced clearance is due to kidney damage, we investigated kidney function and kidney structure of the mice after being exposure to GS-AuNPs. We monitored the

two renal function markers, blood urea nitrogen (BUN) and serum creatinine (sCr), following 14 days after intravenously injecting 15-1059 mg/kg GS-AuNPs into the mice. No significant changes in BUN and sCr levels were found from Day 1 to Day 14, compared to control mice injected with phosphate buffered saline (PBS). The sCr levels were normal for almost all the doses, except for a slight decrease in the group of 365 mg/kg at Day 1 (Figure 3.3A; $P<0.05$). Although transient decrease was also observed in BUN for doses at 15, 183, and 693 mg/kg at Day 7 (Figure 3.3B; $P<0.05$), BUN levels were normal at Day 1, 4, 10 and 14.

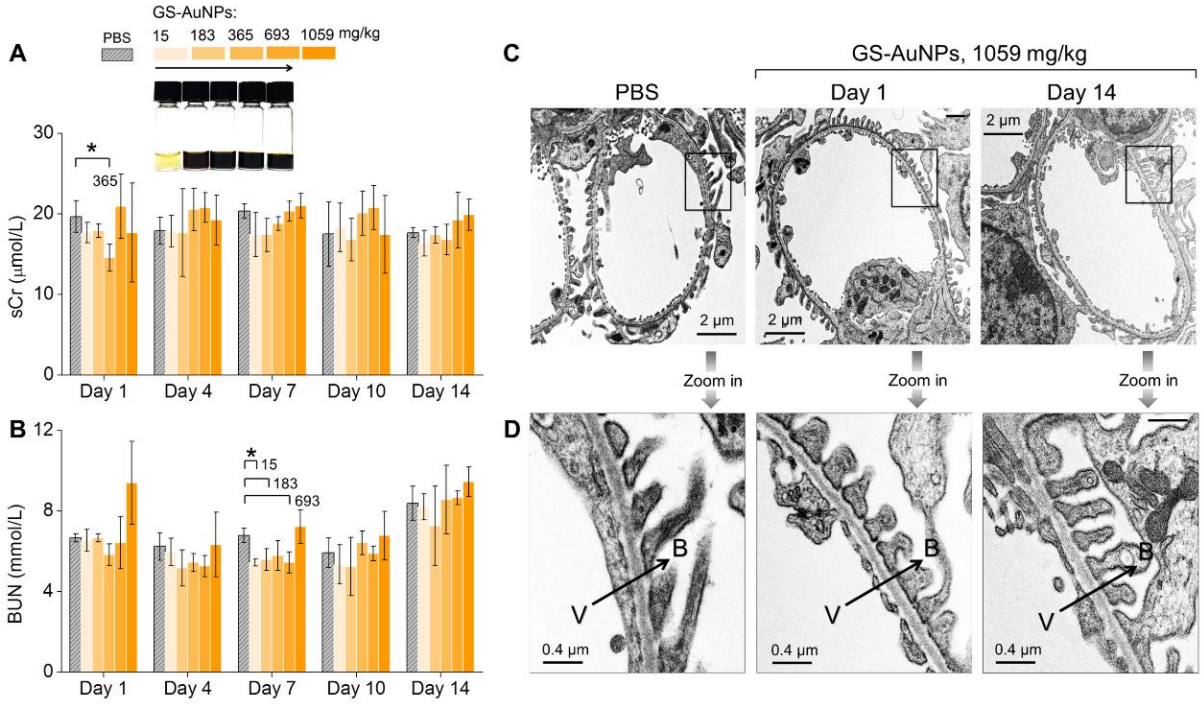

Figure 3.3. Evaluation of renal function and structure of kidney filtration barrier of CD-1 mice after intravenous injection of renal clearable GS-AuNPs at doses from 15 to 183, 365, 693 and 1059 mg/kg. (A) Levels of serum creatinine (sCr) and (B) blood urea nitrogen (BUN) were monitored within 14 days after NP injection. Mice receiving PBS served as control. N = 4 for each group. *P < 0.05. (C, D) Representative transmission electron microscopy (TEM) images of (C) glomeruli and (D) glomerular filtration membranes were taken from mice injected with 1059 mg/kg GS-AuNPs at Day 1 and Day 14. V, vascular lumen; B, Bowman's space; arrows point the direction of filtration.

Using 70 kD dextran, of which the size is slightly larger than the kidney filtration threshold (~6 nm) as a marker[14], we found that there was no leakage of 70 kD dextran into urine after the mice receiving 1059 mg/kg GS-AuNPs (Figure 3.4), indicating that the glomerular barrier remains intact. In addition, as shown by transmission electron microscopy (TEM) imaging, the glomeruli (Figure 3.3C) and glomerular filtration membranes (Figure 3.3D) remained normal at Day 1 and Day 14 after injection of 1059 mg/kg GS-AuNPs. Moreover, no structural changes were found in both renal glomeruli and tubules at the histological level at Day 1, while some AuNPs accumulated in the lumen of the renal tubule (Figure 3.5). At Day 14, the glomeruli were still normal; no tubular damage was found in two mice. For the other two mice, only 5-10% of kidney tissue showed minor interstitial fibrosis and inflammation, tubular atrophy with few intratubular casts with entrapped NPs (Figure 3.6). These results clearly indicate that the observed enhancement in renal clearance of GS-AuNPs at high dose is a normal physiological response of the body rather than caused by damage of the kidneys.

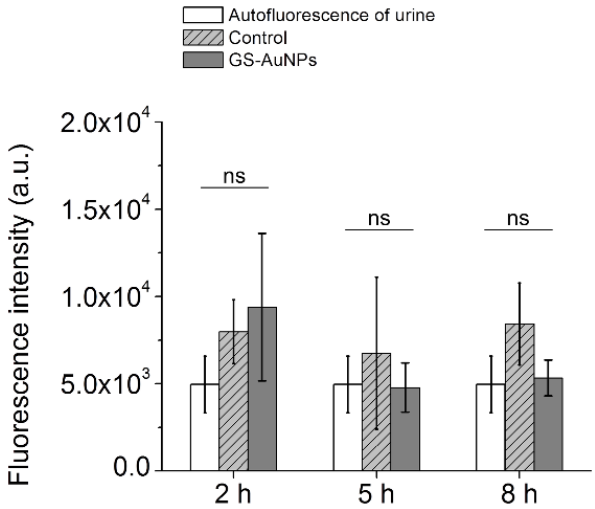

Figure 3.4. Fluorescence intensities of urine samples collected from CD-1 mice at 2, 5 and 8 h post-intravenous injection of FITC-70kD dextran. For "GS-AuNPs" group, 1059 mg/kg GS-AuNPs were intravenously injected into mice at 24 h prior to injection of dextran. For "Control" group, 200 µl PBS was injected at 24 h prior to injection of dextran. Urine samples for

"Autofluorescence" were obtained from mice injected with 200 µl PBS. N=3 for each group. "ns", no significant difference, P>0.05. To avoid variation in urine fluorescence, we used the same group of 3 mice to collect all the data and the procedure was described in the "Materials and Methods".

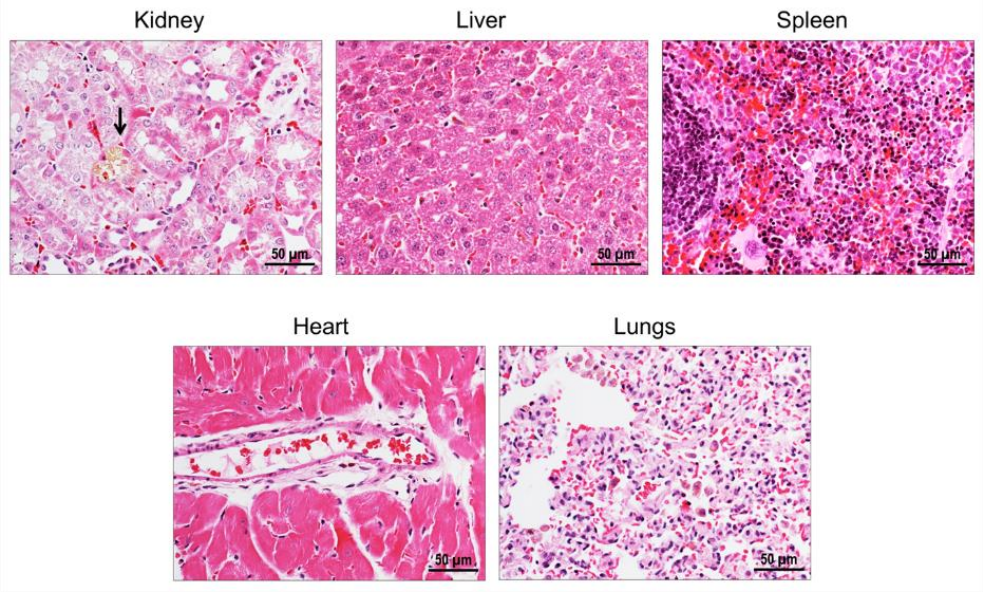

Figure 3.5. Pathological analysis of vital organs (kidneys, liver, spleen, heart and lungs) at 24 h post-intravenous injection of 1059 mg/kg GS-AuNPs. Arrow indicated NPs in the tubular lumen of the kidneys.

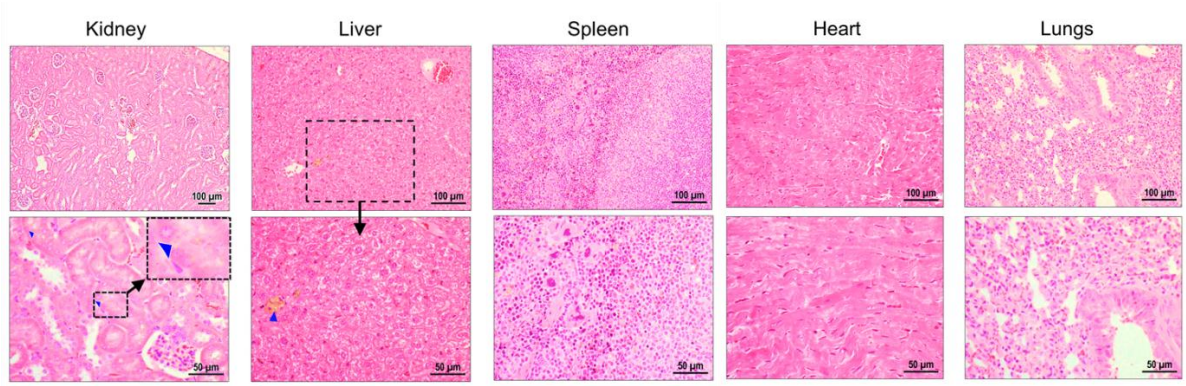

Figure 3.6. Pathological analysis of vital organs (kidneys, liver, spleen, heart and lungs) on the 14th day post-intravenous injection of 1059 mg/kg GS-AuNPs. Blue arrows indicated NPs in kidneys and liver. The zoom-in image of kidney tissue showed that NPs remained in kidney tubular lumen. The zoom-in image of liver tissue at a high magnification showed NPs in the Kuffer cells.

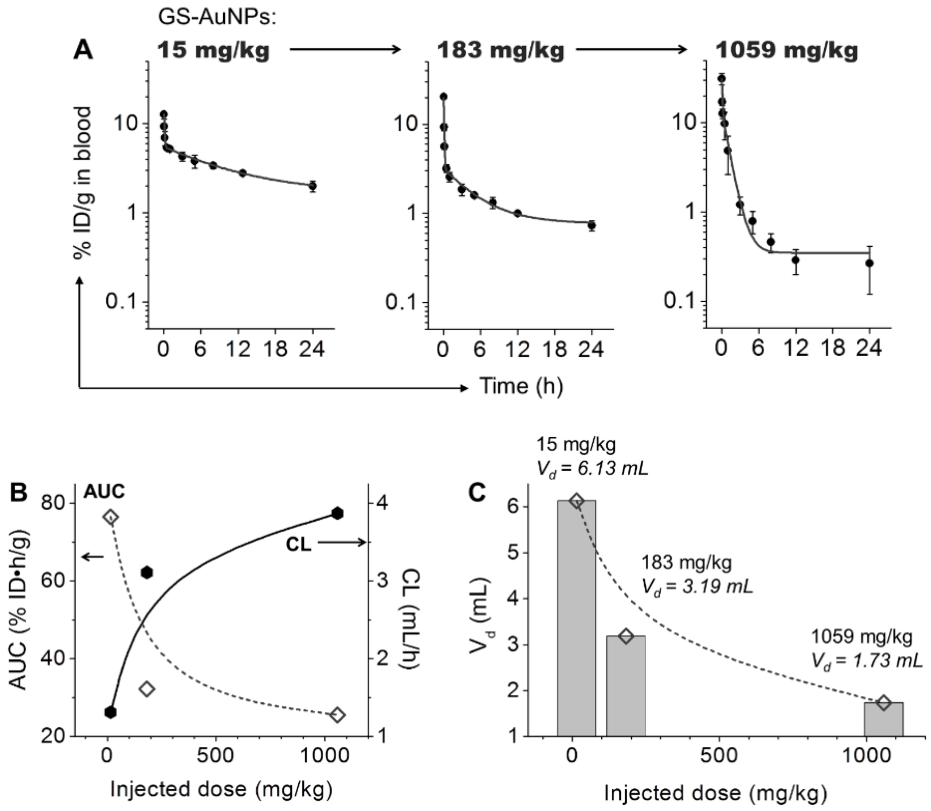

Figure 3.7. Dose dependency in pharmacokinetics of renal clearable GS-AuNPs after intravenous injection. (A) Blood pharmacokinetics at doses of 15, 183 and 1059 mg/kg. N = 3 for each group. (B,C) Changes of pharmacokinetics parameters with dose increased from 15 to 183 and 1059 mg/kg. AUC, the area under curve; CL, plasma clearance; V_d, volume of distribution.

3.3.3 Dose-dependent blood transport process of GS-AuNPs

To further unravel the origin of the dose-dependent renal clearance of GS-AuNPs, we investigated the pharmacokinetics of GS-AuNPs at three doses (15, 183 to 1059 mg/kg) (Figure 3.7A). The analysis of pharmacokinetics parameters revealed that plasma clearance (CL) of GS-AuNPs was increased from 1.31, 3.11 to 3.87 mL/h when the dose increased, corresponding to a decline of the area under the curve (AUC) from 76.5, 32.2 to 25.5 %ID•h/g (Figure 3.7B and Table 3.1). These results suggested an enhanced plasma clearance of GS-AuNPs as dose increased, which in in contrast to Doxil and mezlocillin that shows decreased plasma clearance as dose increases.[4b,5] It

would be interesting to investigate renal clearance of GS-AuNPs at an even higher dose (>1059 mg/kg); however, limited by the solubility of GS-AuNPs in PBS, it is hard to study their renal clearance at even higher doses, which demands the development of more water-soluble renal clearable engineered nanoparticles in the future.

Table 3.1. Pharmacokinetics parameters of GS-AuNPs at three different doses.

Parameters	**Mouse, 15 mg/kg, iv bolus**	**Mouse, 183 mg/kg, iv bolus**	**Mouse, 1059 mg/kg, iv bolus**
Initial concentration (C_0, %ID/g)	16.32	31.30	57.83
Distribution half-life ($t_{1/2\alpha}$, min)	5.0	3.8	2.2
Elimination half-life ($t_{1/2\beta}$, h)	3.25	0.71	0.31
Area under the curve (AUC, %ID•h/g)	76.46	32.24	25.54
Plasma clearance (CL, mL/h)	1.31	3.11	3.87
Volume of distribution (V_d, mL)	6.13	3.19	1.73

The enhanced plasma clearance of GS-AuNPs at higher doses originated from dose-dependent transport of NPs in blood flow. The volume of distribution (V_d) was decreased from 6.13, 3.19 to 1.73 mL as the dose increased from 15, 183 to 1059 mg/kg (Figure 3.7C). The V_d of 6.13 mL (at 15 mg/kg) is comparable to the extracellular fluid volume of mice (~6 mL),[15] and the V_d of 1.73 mL (at 1059 mg/kg) becomes as small as the total plasma volume of mice (~1.56 mL; Table 3.2).[16] These data suggest that at low doses, GS-AuNPs could easily marginate and cross the blood vessel wall and enter into the extravascular space (large V_d), thereby dramatically reducing the blood concentration and slowing down the renal clearance process (Figure 3.8A). At high doses more GS-AuNPs were confined in the blood vessels (small V_d) rather than marginating to the blood vessel wall and diffusing into the background tissues; as a result, they were transported in the blood flow more rapidly and more efficiently eliminated through the kidney (Figure 3.8B).

Table 3.2. Calculation of total plasma volume of mice.

Species	Plasma volume (mL/kg) [a]	Body weight (kg)	Total plasma volume (mL) = Blood volume (mL/kg) x Body weight (kg)
Mice	60	0.026 [b]	1.56

[a] The values of plasma volume (mL/kg) of mice were measured to be ~65.5 mL/kg for female CBA mice and ~56.1 mL/kg for male CBA mice (***J. Phygiol.,*** *1973, 228, 279-284*). An average value of 60 mg/kg was used here.
[b] Body weight of CD-1 mice used in our studies.

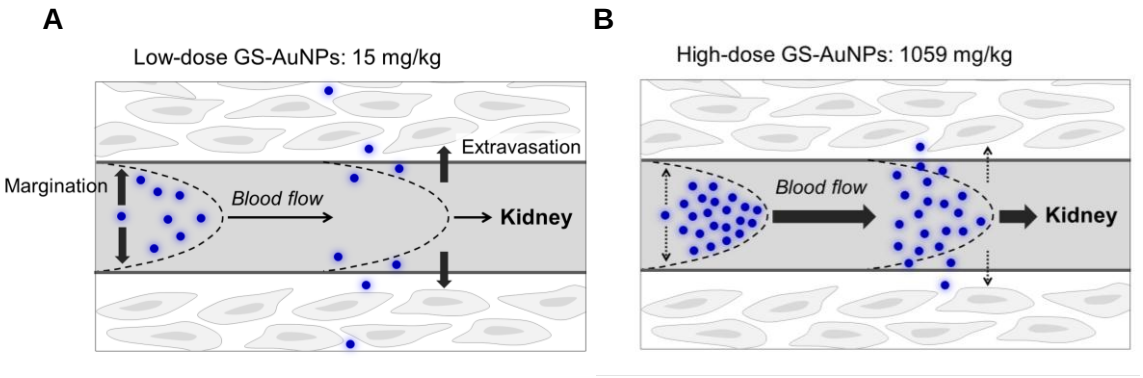

Figure 3.8. Proposed transport behaviours of GS-AuNPs at high and low dose in blood flow, respectively, (A) At low doses, GS-AuNPs could easily marginate toward and then cross the blood vessel wall and enter into the extravascular space, resulting in large V_d and relatively slow clearance. (B) At high doses, rather than marginating toward the blood vessel wall and diffusing into the background tissues, GS-AuNPs tend to be confined in the blood vessels (small V_d); as a result, they were transported in the blood flow more rapidly and more efficiently eliminated through the kidney.

3.3.4 Biocompatibility of GS-AuNPs in mice

Such unique dose-dependent transport and clearance of renal clearable AuNPs significantly reduced their toxicity in mice. The 24-h biodistribution study showed that the accumulation of GS-AuNPs in the kidney was 2-5 %ID per gram of tissue (%ID/g) at all doses; less than 2 %ID/g remained in other vital organs (liver, spleen, bone, lungs, heart and brain) (Figure 3.9). Histological analysis of liver, spleen, heart and lungs at Day 1 and Day 14 revealed no abnormalities after injection of 1059 mg/kg NPs (Figure 3.5&6). Total accumulation of Au in major organs was less

than 5 %ID at 14 days p.i. for all five doses from 15 to 1059 mg/kg (Figure 3.10). During 1~14 days post injection, body weights of mice injected with 15~1059 mg/kg GS-AuNPs were similar to the control mice that received PBS (Figure 3.11). All these results suggest that the no-observed-adverse-effect-level (NOAEL) of GS-AuNPs is larger than 1000 mg/kg in CD-1 mice, 2~35 times higher than the maximal tolerated doses (MTDs) of the highly biocompatible silica NPs in CD-1 mice (30~450 mg/kg).[11]

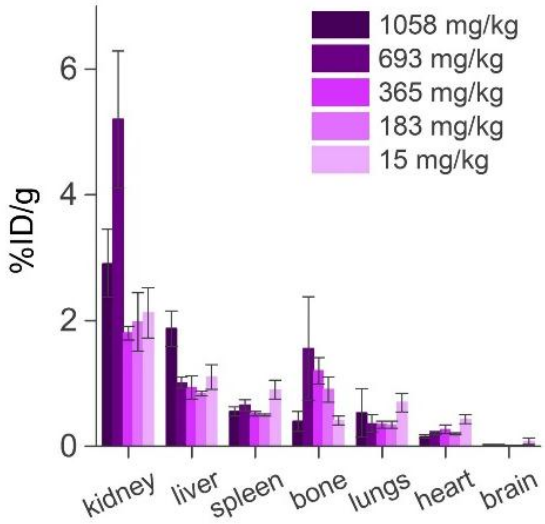

Figure 3.9. Biodistribution of GS-AuNPs at doses of 15, 183, 365, 693 and 1059 mg/kg at 24 h post intravenous injection. The results were obtained by measuring Au amount in organs/tissues with ICP-MS and presented percentage of injected dose per gram of tissue (% ID/g) N=3 for each group.

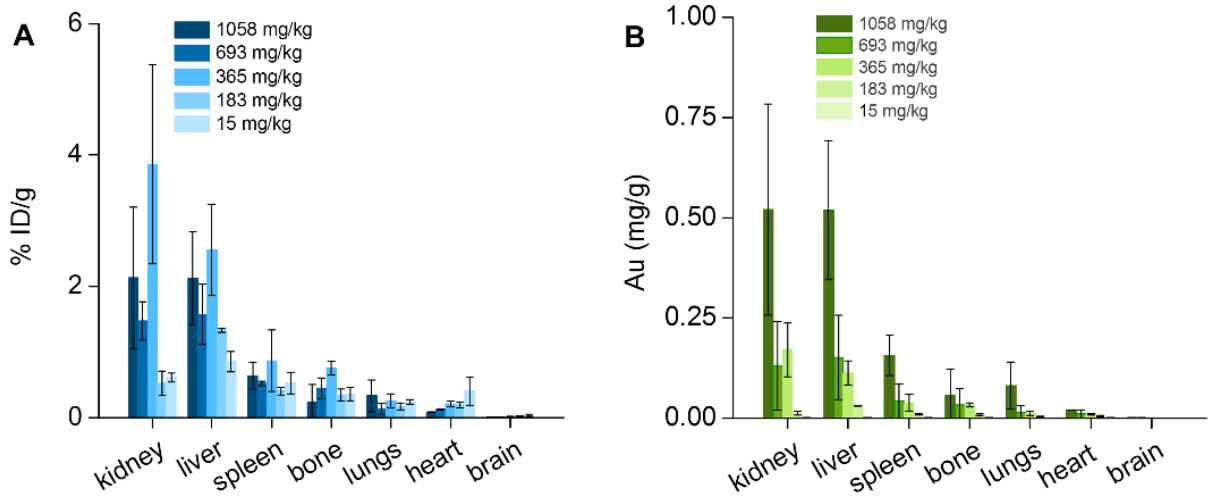

Figure 3.10. Biodistribution of GS-AuNPs at doses of 15, 183, 365, 693 and 1059 mg/kg at 14 days post intravenous injection. The results were obtained by measuring Au amount in organs/tissues with ICP-MS and presented in two ways: (A) Percentage of injected dose per gram of tissue (% ID/g) and (B) Au amount per gram of tissue [Au (mg)/g]. The total accumulation of Au in major organs (heart, liver, spleen, lungs and kidneys) was less than 5 %ID at 14 days p.i. for all the five doses from 15 to 1059 mg/kg. N=4 for each group.

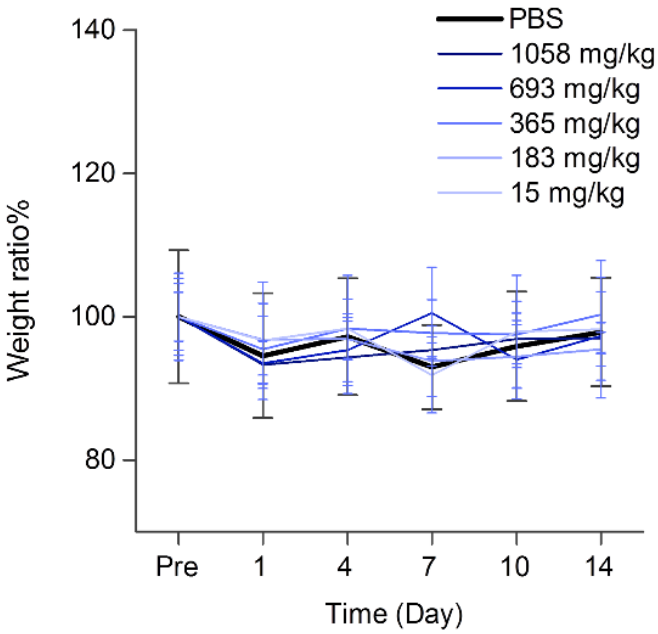

Figure 3.11. Body weights of mice before and during 0-14 days after intravenously injected with 200 µl PBS or 200 µl PBS containing 15, 183, 365, 693 and 1058 mg/kg GS-AuNPs. Results were presented in the form of percentage of the values measured before PBS or NP injection. N=4 for each group.

3.3.5 Biocompatibility of GS-AuNPs in non-human primates

The NOAEL of GS-AuNPs at >1000 mg/kg in mice suggests a NOAEL value of >250 mg/kg for monkeys (to convert mouse dose to monkey dose, the mouse dose is divided by 4.0).[17] We chose cynomolgus monkeys, a species often used in toxicity assessments of nanomedicines,[18] to study renal clearance and biocompatibility of GS-AuNPs. Three monkeys received a single injection of GS-AuNPs at 250 mg/kg body weight through intravenous drip. Consistent with the results in mice, we observed two-compartment blood pharmacokinetics of GS-AuNPs in monkeys after intravenous injection (Figure 3.12A). By measuring the amount of gold in urine and feces with ICP-AES and ICP-MS, we found that only 1.1 %ID was excreted in feces at 24 h p.i., and urine contained 48.6~65.4 %ID (varied among the three monkeys, Figure 3.12B), comparable to the renal clearance efficiency in CD-1 mice (43.3~71.3 %ID for 365~1059 mg/kg, 24 h p.i.). After circulating in the body and being excreted into the urine, GS-AuNPs maintained the same core size (2.5 ± 0.4 nm) as pre-injection samples (2.3 ± 0.3 nm; Figure 3.13), and Fourier transform infrared spectroscopy confirmed that glutathione remained on the particle surface (Figure 3.14). The GS-AuNPs excreted into urine also exhibited little change in the absorption, excitation and emission spectra except for a slight increase of 600 nm emission (Figure 3.15), indicating the surface ligand orientation might be slightly altered during the circulation in the physiological environment.[19]

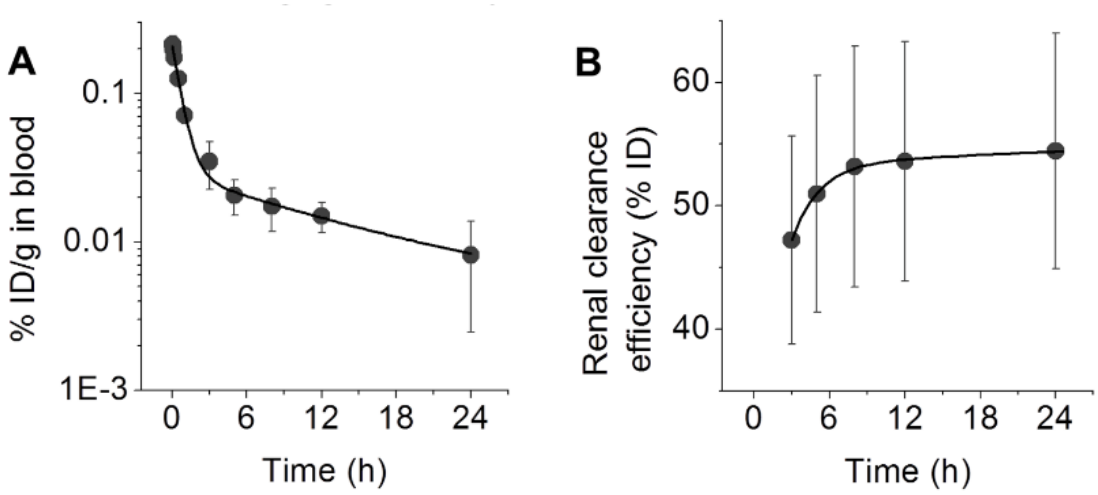

Figure 3.12. (A) Blood pharmacokinetics and (B) renal clearance of intravenously injected GS-AuNPs (250 mg/kg) in cynomolgus monkeys.

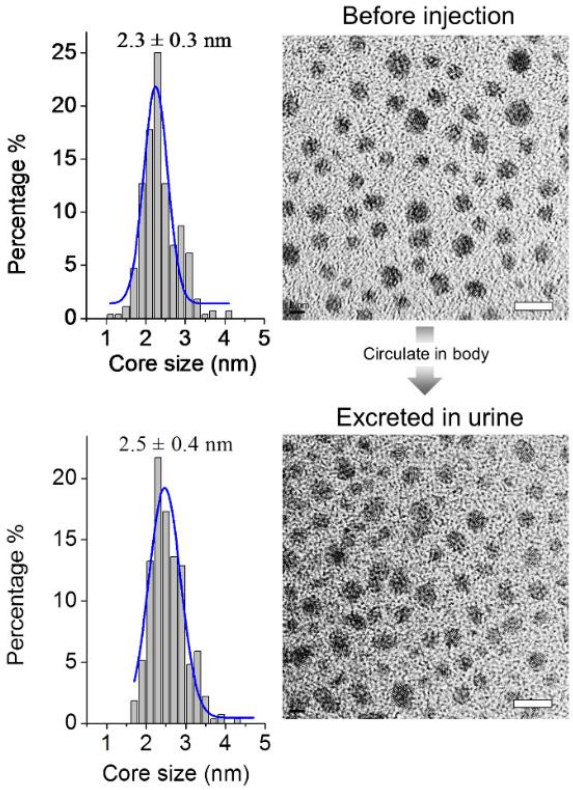

Figure 3.13. Representative TEM images of GS-AuNPs before injection and GS-AuNPs extracted from monkey urine. The analysis of core size distribution was also presented. Scale bar, 5 nm.

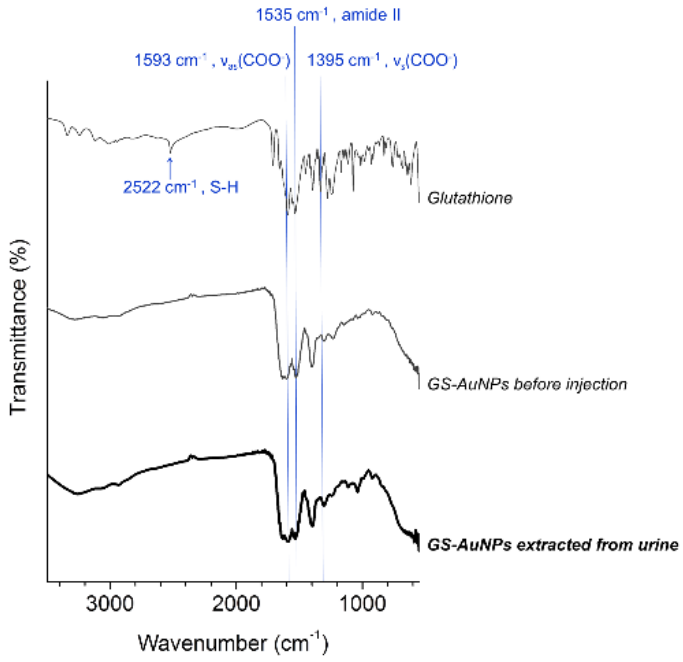

Figure 3.14. FTIR spectra of L-glutathione (GSH), GS-AuNPs before injection, and GS-AuNPs extracted from monkey urine.

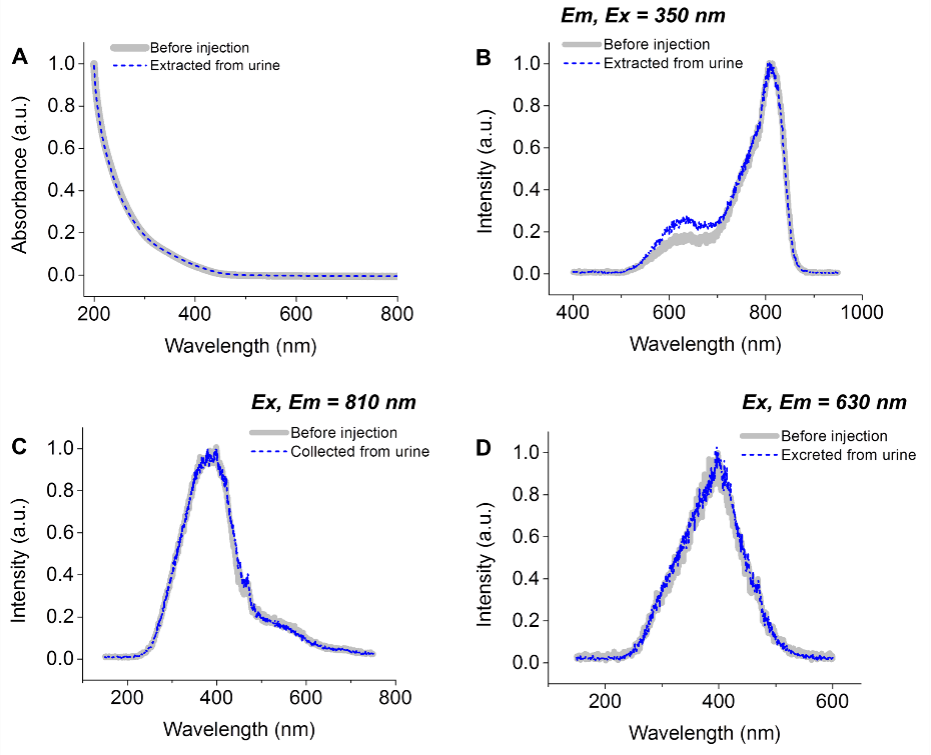

Figure 3.15. (A) Absorption, (B) emission and (C,D) excitation spectra of GS-AuNPs before injection and GS-AuNPs extracted from monkey urine.

We then conducted a preliminary 90-day safety assessment of GS-AuNPs by performing serum biochemistry analysis, urinalysis, complete blood count and blood clotting tests every week. The results were compared with those of three monkeys without any treatment. No evidence of kidney damage was observed after exposure to 250 mg/kg GS-AuNPs. In the case of renal function biomarker sCr, we found no difference between NP-injected group and pre-injection level of the same monkeys at Day1, 3 and 7 (Figure 3.16A) as well as control group during 7-90 days (Figure 3.16B). The relatively large variation in sCr levels at pre-injection, Day 1 and Day 3 could be due to that the sCr is also affected by many other factors such as food intake and muscle mass.[20] While BUN transiently increased at Day 3 relative to pre-injection value ($P<0.05$; Figure 3.16C), it was normal at Day 1 and returned to a level comparable to pre-injection value at Day 7 (Figure 3.16C) and those of the control group during 7~90 days (Figure 3.16D). No abnormalities were detected in urinalysis parameters (urine specific gravity, urine pH, urine protein and number of blood cells) during 90 days (Figure 3.17).

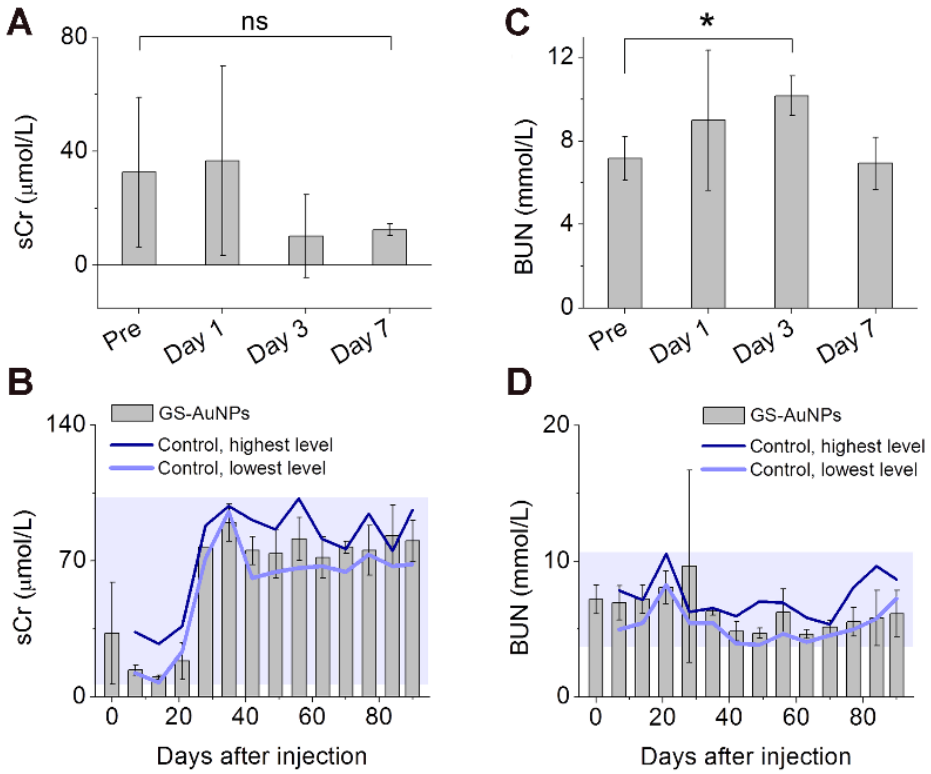

Figure 3.16. (A,B) serum creatinine (sCr) and (C,D) blood urea nitrogen (BUN) were monitored for 90 days after intravenous injection of GS-AuNPs (250 mg/kg). Monkeys without any treatment served as control. N = 3 for each group. *P < 0.05.

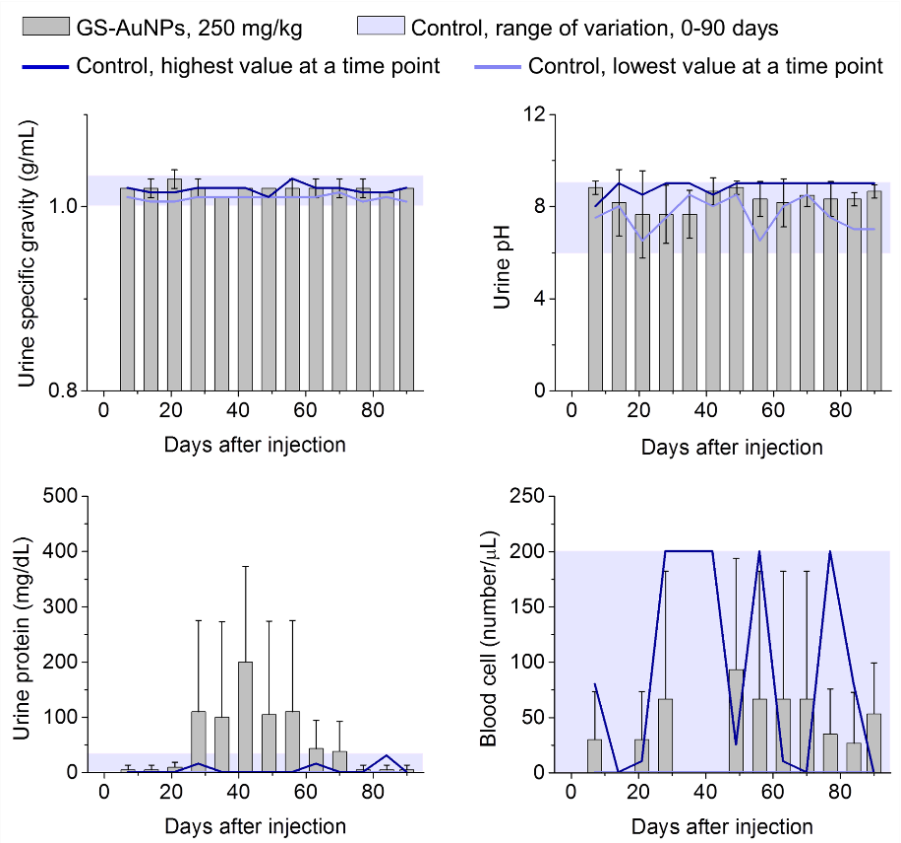

Figure 3.17. Urinalysis results of cynomolgus monkeys during 0-90 days after receiving a single-injection of 250 mg/kg GS-AuNPs. Monkeys without any treatment served as control. N = 3 for each group.

The liver function biomarkers—alanine transaminase (ALT), aspartate transaminase (AST), total bilirubin (TBIL), triglycerides (TG), cholesterol (CHOL), total protein (TP), albumin (ALB), total protein (TP) and albumin (ALB)—were also in a normal range after NP injection relative to control group during 90 days p.i. (Figure 3.18&3.19). While a lower level of alkaline phosphatase (ALP) was found in NP-injected monkeys during 7-90 days p.i., ALP is a less specific indicator of liver function[18b] and elevated ALP level is often observed after injection of NPs.[21] Parameters of complete blood count remained in a normal range, suggesting that GS-AuNPs did not induce systemic inflammation (Figure 3.20). Results of blood clotting tests confirmed that GS-AuNPs did

not affect the coagulation system (Figure 3.21). Body weights and body temperatures were also monitored every week and no differences were found between NP-injected group and the control, implying minimal systemic toxicity of 250 mg/kg GS-AuNPs (Figure 3.22). No abnormal behaviors were observed after receiving GS-AuNPs. All these results indicated that GS-AuNPs were well tolerated by monkeys and did not induce adverse effects within 90 days following the single injection at 250 mg/kg. Therefore, the no-observed-adverse-effect-level (NOAEL) of GS-AuNPs should be larger than 250 mg/kg in cynomolgus monkeys.

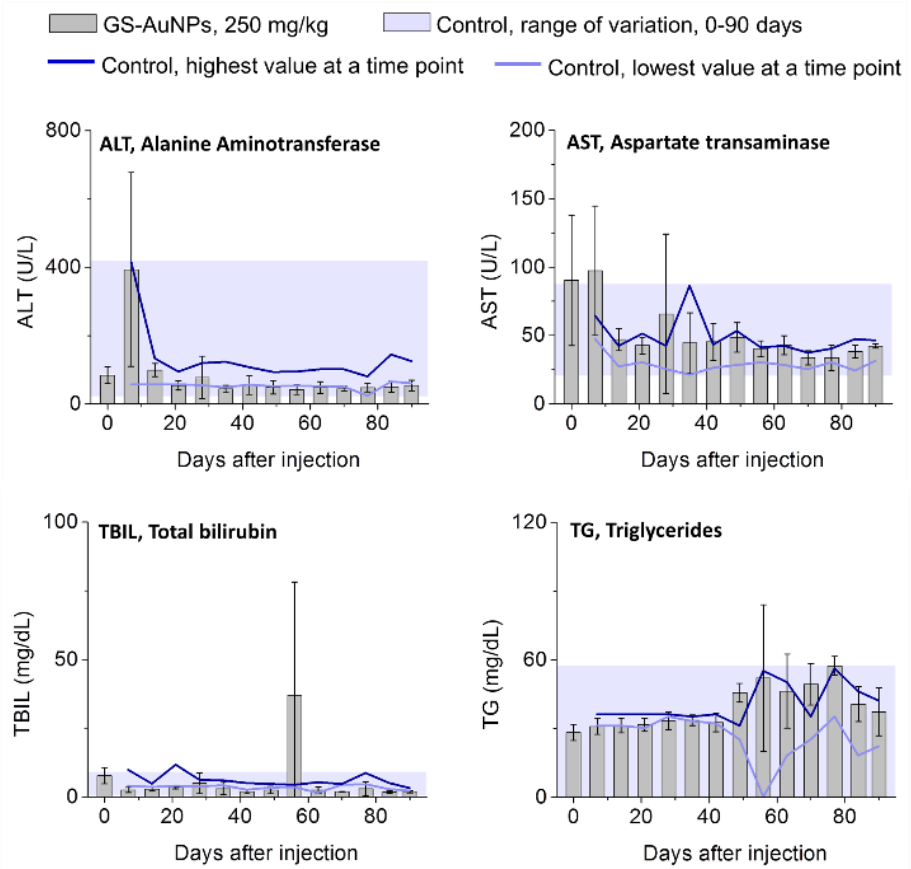

Figure 3.18. Liver function markers in serum of cynomolgus monkeys during 0-90 days after receiving a single-injection of 250 mg/kg GS-AuNPs. Monkeys without any treatment served as control. N = 3 for each group.

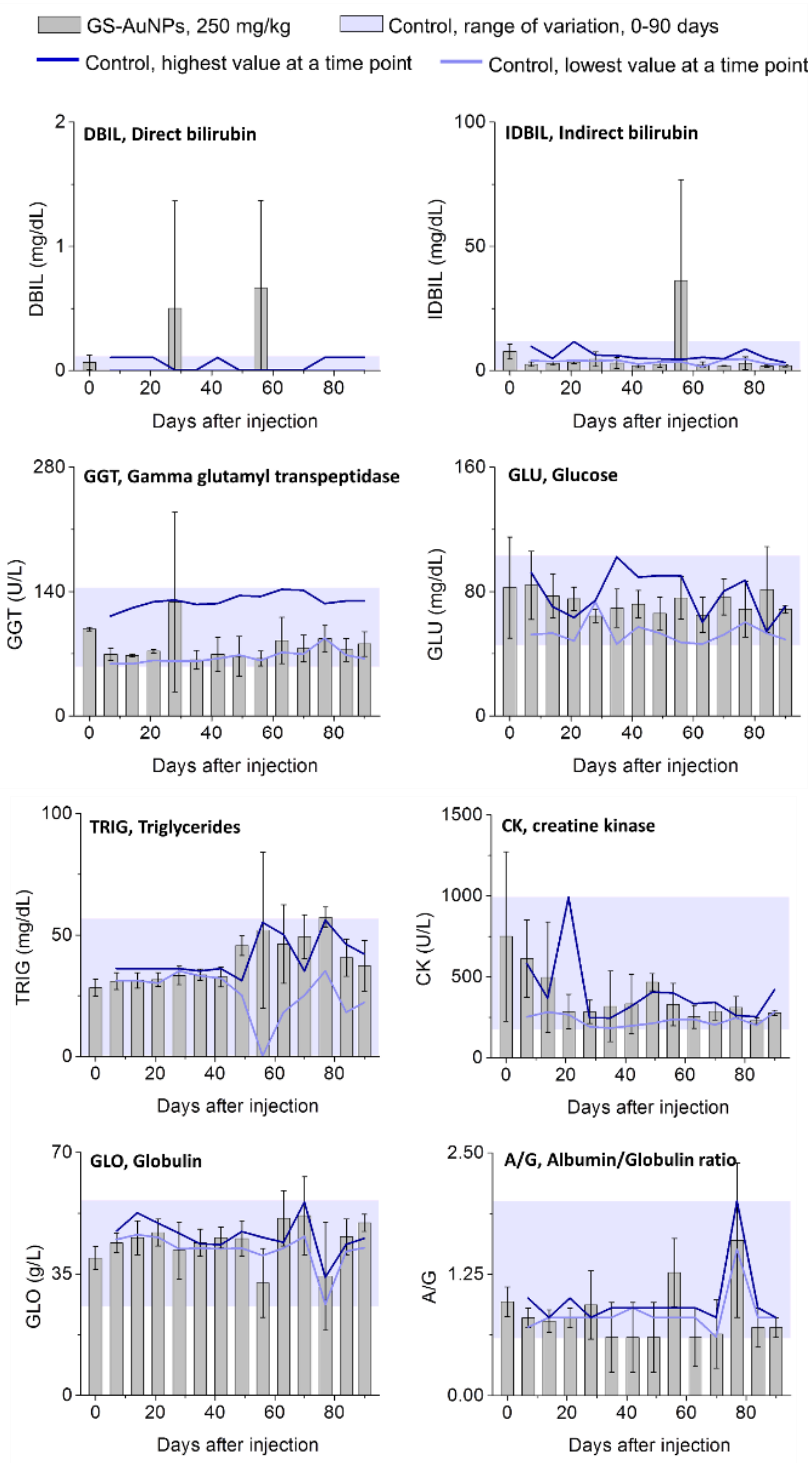

Figure 3.19. Other biomarkers in serum of cynomolgus monkeys during 0-90 days after receiving a single-injection of 250 mg/kg GS-AuNPs. Monkeys without any treatment served as control. N = 3 for each group.

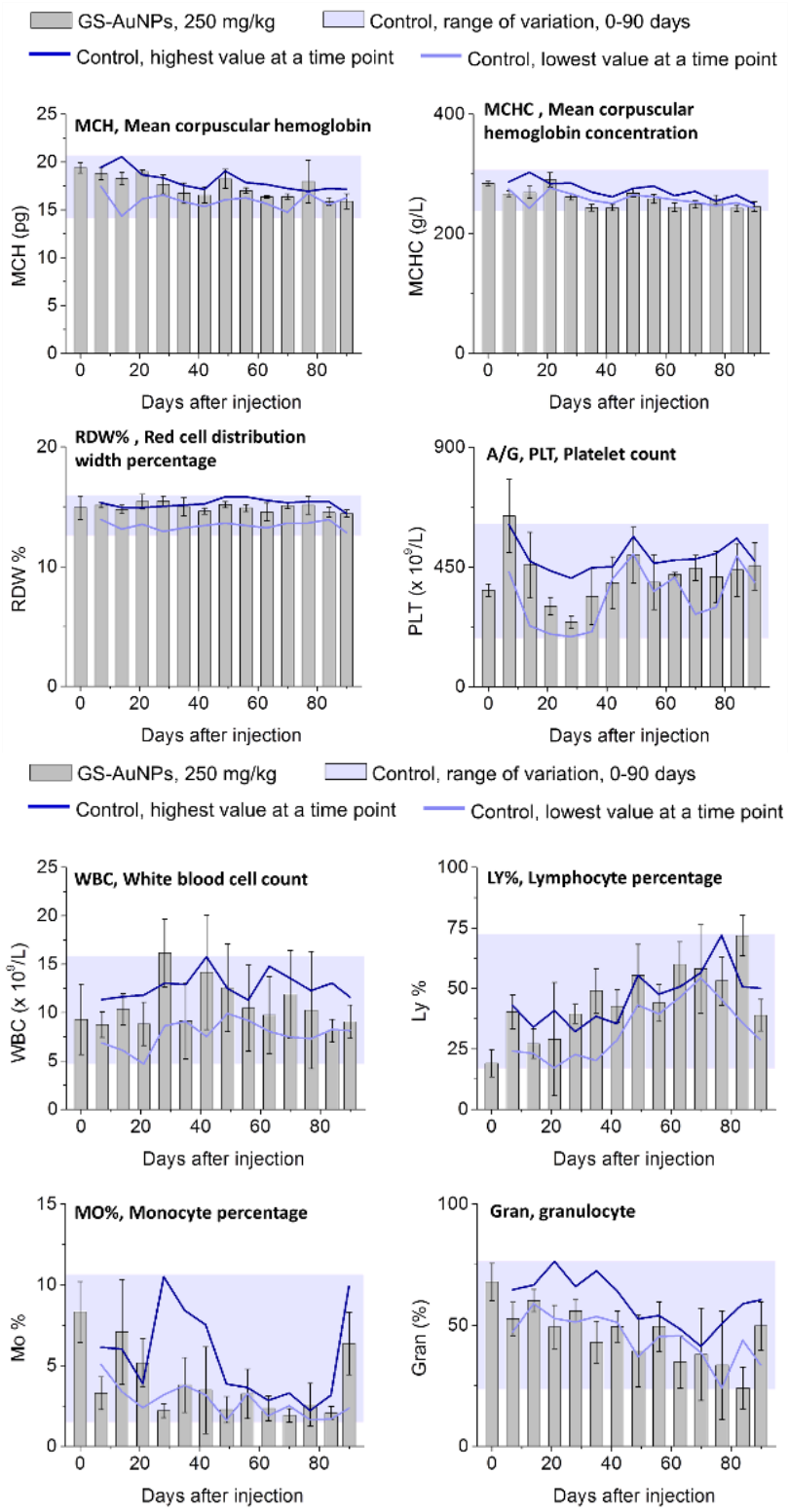
GS-AuNPs, 250 mg/kg
Control, range of variation, 0-90 days
Control, highest value at a time point
Control, lowest value at a time point
MCH, Mean corpuscular hemoglobin
MCH (pg)
MCHC , Mean corpuscular hemoglobin concentration
MCHC (g/L)
RDW% , Red cell distribution width percentage
RDW %
A/G, PLT, Platelet count
PLT (x 10⁹/L)
Days after injection
GS-AuNPs, 250 mg/kg
Control, range of variation, 0-90 days
Control, highest value at a time point
Control, lowest value at a time point
WBC, White blood cell count
WBC (x 10⁹/L)
LY%, Lymphocyte percentage
Ly %
MO%, Monocyte percentage
Mo %
Gran, granulocyte
Gran (%)
Days after injection

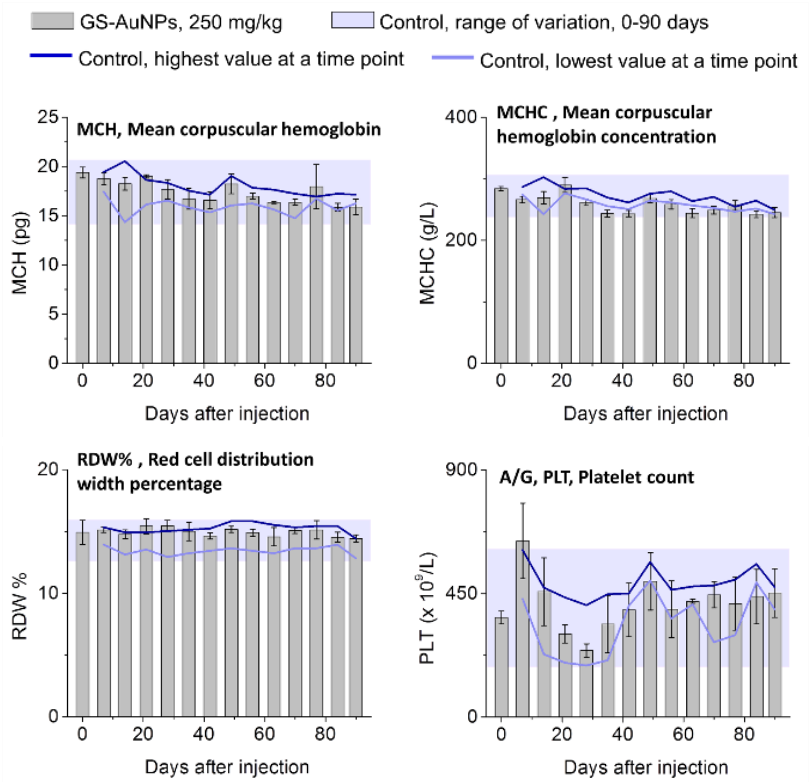

Figure 3.20. Complete blood count of cynomolgus monkeys during 0-90 days after receiving a single-injection of 250 mg/kg GS-AuNPs. Monkeys without any treatment served as control. N = 3 for each group.

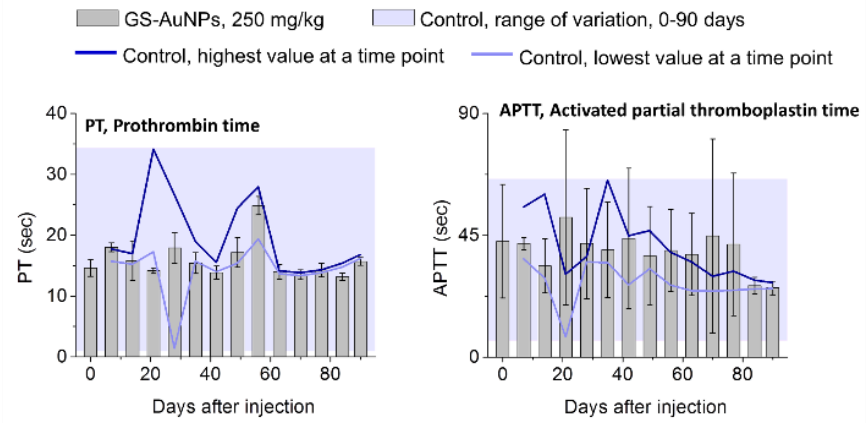

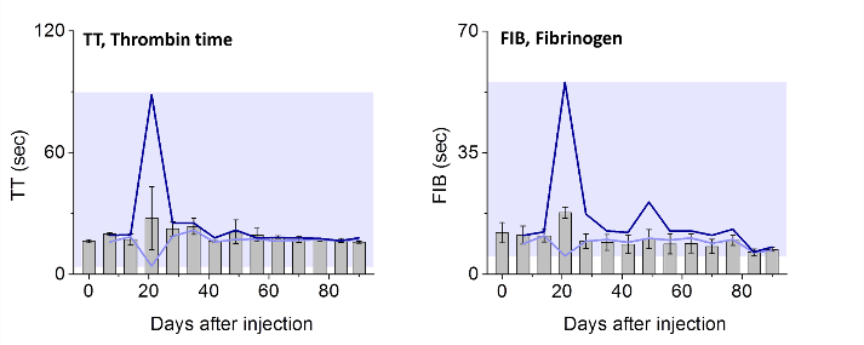

Figure 3.21. Blood clotting tests of cynomolgus monkeys during 0-90 days after receiving a single-injection of 250 mg/kg GS-AuNPs. Monkeys without any treatment served as control. N = 3 for each group.

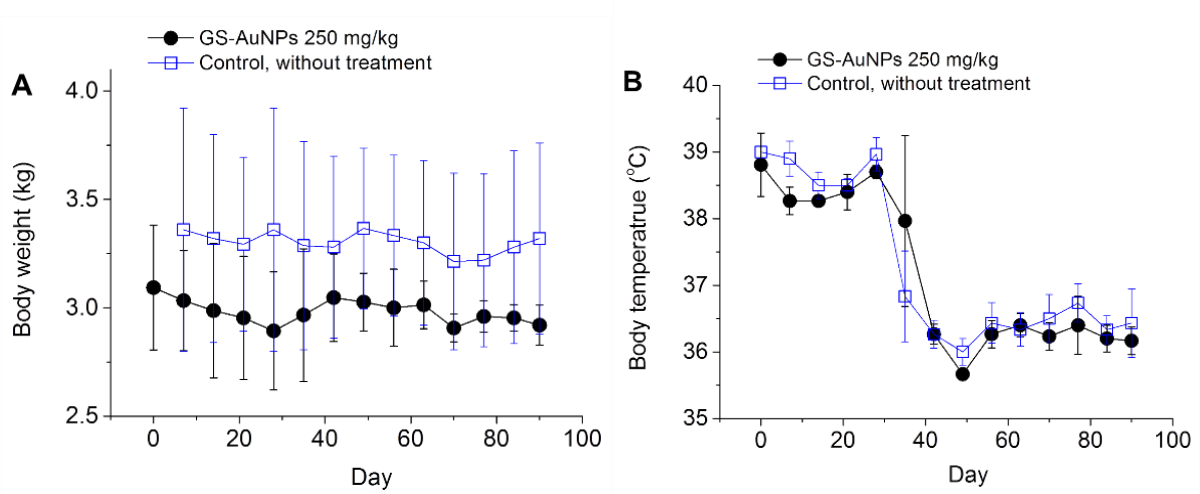

Figure 3.22. Body weights and body temperatures of cynomolgus monkeys during 0-90 days after receiving a single-injection of 250 mg/kg GS-AuNPs. Monkeys without any treatment served as control. N = 3 for each group.

3.4 Conclusion

In summary, using CD-1 mice as a model, we studied the dose effect on pharmacokinetics and clearance of renal clearable AuNPs in the range of 0.15-1059 mg/kg. The renal clearance efficiency remained at a constant level (~35 %ID) at doses ranging from 0.15 to 15 mg/kg. Taking advantage of this dose-independent renal clearance at low doses, we ruled out the dose effect when studying

how particle size impacted the glomerular filtration of gold nanoclusters (100 μL, 100 μmol/L, 2~6 mg/kg) in a sub-nanometer regime.[7d] On the other hand, we observed a strong dose dependencies in PK and renal clearance at doses from 15-1059 mg/kg: As dose increased, renal clearance efficiency at 2 h p.i. linearly increased from 34.6 to 69.0 %ID, since more AuNPs were confined in the blood vessels and rapidly eliminated into the urine. The unique responses of the body to high doses of renal clearable AuNPs significantly reduce their toxicity: no structural changes in renal glomeruli and tubules of mice as well as low systematic toxicity were observed even at the dose of 1059 mg/kg AuNPs, which are higher than the MTD value of the highly biocompatible silica NPs (450 mg/kg). This efficient renal clearance and high biocompatibility of the GS-AuNPs were also confirmed in non-human primates. These results significantly advance our fundamental understanding of *in vivo* transport of NPs at the different doses, and lay down a foundation for optimizing the injected dose to maximize their potential in future clinical practices.

3.5 Acknowledgements

The mouse studies were supported in part by the NIH (R01DK103363), CPRIT (140544 and 160866) and the start-up fund from the University of Texas at Dallas. The monkey studies were supported by the start-up fund from the University of Texas at Dallas. J.Z. would also like to thank Prof. Hua Shen, associate director of Kunming Institute of Zoology, Chinese Academy of Sciences and Prof. Shuo Shi, associate director of National Astronomical Observatories, Chinese Academy of Sciences for their help on the monkey studies.

3.6 Authors Contributions

Jing Xu, Chuanqi Peng, Phoebe Carter, Xuhui Ning, Qinhan Zhou, Greg Zhang performed the experiments on mice; Mengxiao Yu, Qiu Tu, Anthony Dao, Jia Tian and Xingya Jiang performed the experiments on Monkeys. Jing Xu, Mengxiao Yu, Jie Zheng, Payal Kapur, Jer-Tsong Hsieh, Xudong Zhao and Pengyu Liu reviewed, analysed and interpreted the data. Jing Xu, Mengxiao Yu and Jie Zheng wrote the paper. All authors discussed the results and commented on the manuscript.

3.7 References

[1] a) B. Hamm, T. Staks, A. Mühler, M. Bollow, M. Taupitz, T. Frenzel, K. J. Wolf, H. J. Weinmann, L. Lange, *Radiology* **1995**, *195*, 785-792; b) K. Shamsi, T. Balzer, S. Saini, P. R. Ros, R. C. Nelson, E. C. Carter, S. Tollerfield, H. P. Niendorf, *Radiology* **1998**, *206*, 365-371.

[2] a) M. M. Reidenberg, M. Levy, H. Warner, C. B. Coutinho, M. A. Schwartz, G. Yu, J. Cheripko, *Clin. Pharmacol. Ther.* **1978**, *23*, 371-374; b) H. J. Johnson, S. K. Swan, K. L. Heim-Duthoy, A. J. Nicholls, I. Tsina, T. Tarnowski, *Clinical Pharmacology & Therapeutics* **1998**, *63*, 512-518.

[3] a) R. Tallarida, L. S. Jacob, *The Dose—Response Relation in Pharmacology*, *Springer Science & Business Media*, **2012**; b) B. G. Katzung, S. B. Masters, A. J. Trevor, *Basic & clinical pharmacology*, 12 ed., **2004**; c) H. Nicholas, G. Holford, L. B. Sheiner, *Clinical Pharmacokinetics* **1981**, *6*, 429-453.

[4] a) B. K. Wong, P. J. Bruhin, J. H. Lin, *Journal of Pharmaceutical Sciences* **1999**, *88*, 277-280; b) G. L. Jungbluth, W. J. Jusko, *Antimicrobial Agents and Chemotherapy* **1989**, *33*, 839-843; c) I. Bernus, R. G. Dickinson, W. D. Hooper, M. J. Eadie, *Epilepsy research* **1996**, *24*, 163-172; d) P. A. Cleveland, S. Teller, V. Kachevsky, E. Pinili, R. Evans, M. W. Modi, *Drug Metabolism and Disposition* **1991**, *19*, 245-250.

[5] A. Gabizon, D. Tzemach, L. Mak, M. Bronstein, A. T. Horowitz, *Journal of Drug Targeting* **2002**, *10*, 539-548.

[6] a) M. Baek, H.-E. Chung, J. Yu, J.-A. Lee, T.-H. Kim, J.-M. Oh, W.-J. Lee, S.-M. Paek, J. K. Lee, J. Jeong, *International Journal of Nanomedicien* **2012**, *7*, 3081-3097; b) N. Shinohara, Y. Oshima, T. Kobayashi, N. Imatanaka, M. Nakai, T. Ichinose, T. Sasaki, G. Zhang, H. Fukui, M. Gamo, *Toxicology* **2014**, *325*, 1-11; c) H. Soo Choi, W. Liu, P. Misra,

E. Tanaka, J. P. Zimmer, B. Itty Ipe, M. G. Bawendi, J. V. Frangioni, *Nature Biotechnology* **2007**, *25*, 1165-1170; d) M. Yu, J. Zheng, *ACS Nano* **2015**, *9*, 6655-6674; e) M. *Longmire*, P. L. Choyke, H. Kobayashi, *Nanomedicine (Lond.)* **2008**, *3*, 703-717

[7] a) H. Kang, J. Gravier, K. Bao, H. Wada, J. H. Lee, Y. Baek, G. El Fakhri, S. Gioux, B. P. Rubin, J.-L. Coll, H. S. Choi, *Advanced Materials* **2016**, *28*, 8162-8168; b) A. A. Burns, J. Vider, H. Ow, E. Herz, O. Penate-Medina, M. Baumgart, S. M. Larson, U. Wiesner, M. Bradbury, *Nano Letters* **2008**, *9*, 442-448; c) C. Zhou, M. Long, Y. Qin, X. Sun, J. Zheng, *Angewandte Chemie International Edition* **2011**, *50*, 3168-3172; d) B. Du, X. Jiang, A. Das, Q. Zhou, M. Yu, R. Jin, J. Zheng, *Nature Nanotechnology* **2017**, *12*, 1096-1102.

[8] S. Tang, C. Peng, J. Xu, B. Du, Q. Wang, R. D. Vinluan, M. Yu, M. J. Kim, J. Zheng, *Angewandte Chemie International Edition* **2016**, *55*, 16039-16043.

[9] J. Liu, M. Yu, C. Zhou, S. Yang, X. Ning, J. Zheng, *Journal of American Chemistry Society* **2013**, *135*, 4978-4981.

[10] a) M. Yu, J. Liu, X. Ning, J. Zheng, *Angewandte Chemie International Edition* **2015**, *54*, 15434-15438; b) M. Yu, J. Zhou, B. Du, X. Ning, C. Authement, L. Gandee, P. Kapur, J.-T. Hsieh, J. Zheng, *Angewandte Chemie International Edition* **2016**, *55*, 2787-2791.

[11] T. Yu, K. Greish, L. D. McGill, A. Ray, H. Ghandehari, *ACS Nano* **2012**, *6*, 2289-2301.

[12] a) M. Yu, C. Zhou, L. Liu, S. Zhang, S. Sun, J. D. Hankins, X. Sun, J. Zheng, *Angewandte Chemie International Edition* **2017**, *56*, 4314-4319; b) J. Liu, M. Yu, X. Ning, C. Zhou, S. Yang, J. Zheng, *Angewandte Chemie International Edition* **2013**, *52*, 12572-12576; c) C. Peng, X. Gao, J. Xu, B. Du, X. Ning, S. Tang, R. M. Bachoo, M. Yu, W.-P. Ge, J. Zheng, *Nano Research* **2017**, *10*, 1366-1376.

[13] J. Xu, M. Yu, P. Carter, E. Hernandez, A. Dang, P. Kapur, J.-T. Hsieh, J. Zheng, *Angewandte Chemie International Edition* **2017**, *56*, 13356 – 13360

[14] Y. S. Long, S. Zheng, P. M. Kralik, F. W. Benz, P. N. Epstein, *Journal of Diabetes Research* **2016**, 2016, doi:10.1155/2016/8749417

[15] M. E. Chapman, L. Hu, C. F. Plato, D. E. Kohan, *American Journal of Physiolology-Renal Physiology* **2010**, *299*, F280-F283.

[16] A. C. Riches, J. G. Sharp, D. B. Thomas, S. V. Smith, *The Journal of Physiology* **1973**, *228*, 279-284.

[17] A. B. Nair, S. Jacob, *Journal of Basic and Clinical Pharmacy* **2016**, *7*, 27-31.

[18] a) S. Kotb, J. Piraquive, F. Lamberton, F. Lux, M. Verset, V. Di Cataldo, H. Contamin, O. Tillement, E. Canet-Soulas, L. Sancey, *Scientific Reports* **2016**, *6*, 35053; b) L. Moore, J. Yang, T. T. H. Lan, E. Osawa, D.-K. Lee, W. D. Johnson, J. Xi, E. K.-H. Chow, D. Ho, *ACS Nano* **2016,** *10*, 7385-7400.

[19] J. Liu, P. N. Duchesne, M. Yu, X. Jiang, X. Ning, R. D. Vinluan, P. Zhang, J. Zheng, *Angewandte Chemie International Edition* **2016,** *55*, 8894-8898

.

[20] V. R. Dharnidharka, C. Kwon, G. Stevens, *American Journal of Kidney Diseases* **2002**, *40*, 221-226

[21] a) K. Parivar, F. Malekvand Fard, M. Bayat, S. M. Alavian, M. Motavaf, *Iranian Red Crescent Medical Journal* **2016**, *18*, e28939; b) J. Wang, L. Wang, Y. Fan, *International Journal of Molecular Sciences* **2016**, *17*, 798.

CHAPTER 4

LIGAND-DENSITY EFFECT ON *IN VITRO* INTERACTION OF RENAL CLEARABLE GOLD NANOPARTICLES WITH RENAL TUBULAR CELLS

Authors- Jing Xu[§], Linxi Shi[#], Chance Nowak[†], Xuhui Ning[§], Yingyu Huang[§], Mengxiao Yu[§], Leonidas Bleris[†] and Jie Zheng[§]

[§]Department of Chemistry and Biochemistry, BE 26

The University of Texas at Dallas

800 West Campbell Road

Richardson, Texas USA 75080

[†] Department of Bioengineering, BSB 11

The University of Texas at Dallas

800 West Campbell Road

Richardson, Texas USA 75080

[#]Department of Microbiology and Immunology

Kunming Medical University

191 Renmin W Rd, Xishan Qu, Kunming Shi, Yunnan Sheng, China, 650221

Abstract

Numerous studies have established the importance of physicochemical properties in cellular responses to nanoparticles, however, the effect of surface ligand density is understood poorly. Here we examined the interactions between human kidney proximal tubular (HK-2) cells and glutathione-coated renal clearable gold nanoparticles (GS-AuNPs) with difference in surface ligand density. We observed low ligand density resulted in high binding affinity of GS-AuNPs to the plasma membrane of HK-2 cells. The binding activity further induced membrane breakage and cell necrosis. GS-AuNPs with high ligand density exhibited weak interaction with HK-2 cells and facilitated the cell apoptosis. Glutathione was found only mediating the cellular interactions of GS-AuNPs with low ligand density. These findings not only advanced our understanding of ligand density effect on NP-cell interactions *in vitro* but provide insight into designing renal clearable inorganic nanomedicine with minimized renal cytotoxicity.

4.1 Introduction

Physical and chemical characters of nanoparticles (NPs) have been demonstrated influential in the biological responses to the nanostructures.[1] To develop precision nanomedicine with maximized efficacy and minimized toxicity, fundamental investigations on the effects of physicochemical properties on cellular interaction of nanostructures are being conducted extensively and understandings have been obtained on the influence of size, shape and surface chemistry. For example, Chan et al. observed an optimal size, approximately 50 nm, in the passive targeting of gold nanoparticles (NPs) regardless of the surface materials.[2] Gratton et al. reported that the rod-shaped nanostructure exhibited highest cellular uptake efficiency vs. the spherical, cylindrical or cubical counterparts.[3] Ahemed and his coworkers discovered that polysaccharide coated silver NPs caused more severe DNA damage response than the uncoated silver NPs.[4] While these and many other studies have contributed remarkably to the design of precision nanomedicine, another structural factor, surface ligand density has not been given enough attention as the other factors, whose impact is significant on the efficacy of receptor-mediated interactions such as cell targeting and NP internalization. The obtained understanding of the ligand density effect was that the nanostructure with increased surface ligand density would display unchanged *in vitro* interaction while the efficacy or avidity would be dramatically increased.[1a, 5] However, some recent publications indicated an optimal surface ligand density existed and overly dense ligands might even alter the form of cellular response.[6] For example, Elias et al. reported the superparamagnetic iron oxide NPs coated with moderately dense HER2/neu antibody achieved maximal targeting efficiency to tumor cells and the observation was independent of particle size.[7] Moradi and her coworkers discovered highly dense folate on the surface switched the internalization of folate

coated polystyrene NPs from clathrin-mediated endocytosis to caveolin-mediated endocytosis.[8] These findings put the original understanding of ligand density effect in controversy and motivate more comprehensive exploration on this topic. Here we use our renal clearable glutathione-coated gold NPs (GS-AuNPs) as a model to investigate the effect of surface ligand density on the interactions between GS-AuNPs and renal cells. In addition to enriching the knowledge on ligand-density-dependent cellular reactions to nanostructures, the investigation on GS-AuNPs would advance our understanding on precise response of kidneys to renal clearable inorganic NPs, which is beneficial to optimize the biomedical potential and minimize the renal cytotoxicity of renal clearable inorganic nanomedicine.

In this report, we discovered that ligand density significantly affected the cytotoxicity induced by GS-AuNPs and its binding affinity to plasma membrane of human kidney proximal tubular (HK-2) cells. The number of bound GS-AuNPs with low ligand density ($AuSG_{183}$) was approximately four-time of that of GS-AuNPs with high ligand density ($AuSG_{385}$). The intense binding of $AuSG_{183}$ led to membrane breakage and necrosis of HK-2 cells while $AuSG_{385}$ activated cell apoptosis. Glutathione was found to mediate the binding activity of $AuSG_{183}$ while relatively inert in the interaction between $AuSG_{385}$ and HK-2 cells. These findings not only highlight how precisely the biological system responds to NPs with difference in ligand density but also provide insight into developing renal clearable nanomedicines with minimized renal cytotoxicity.

4.2 Materials and Methods

4.2.1 Materials and equipment

Hydrogen tetrachloroaurate ($HAuCl_4$), L-reduced glutathione (GSH), 3-(4,5-dimethylthiazol-2-yl)-2,5-diphenyltetrazolium bromide (MTT) and probenecid were purchased from Sigma-Aldrich. Alexa Fluor® 488 Annexin V/Dead Cell Apoptosis Kit and live cell imaging solution were purchased from Fisher Scientific. Cell membrane binding images were obtained by a BX-51 upright microscope (Olympus) with a 20X/0.46BD objective and an 18.2 Color Mosaic CCD camera (Diagnostic Instruments). Cellular gold amount was measured by an inductively coupled plasma mass spectrometry (ICP-MS, Angilent 7900). Cell viability was measured by an absorbance microplate reader (Emax® Plus). The hydrodynamic diameter and zeta potential of each particle were measured by a Zetasizer Nano ZS. Apoptosis assays were measured by a BD LSRFortessa™ flow cytometer.

4.2.2 Methods

Synthesis of $AuSG_{183}$, $AuSG_{211}$, $AuSG_{385}$

The three glutathione coated gold nanoparticles were synthesized with the approaches reported in one of our previously published literatures.[9] Basically, all the three particles were fabricated by the same thermal reduction method with only the different ratios of reacting agents. Briefly, 1M $HAuCl_4$ was mixed with L-glutathione solution under stirring. The mixture was further heated to and then kept at approximately 95ºC until the maximal fluorescence intensity was obtained. The ratio of glutathione to $HAuCl_4$ was 0.8:1 for $AuSG_{183}$, 1.2:1 for $AuSG_{211}$ and 1.6:1 for $AuSG_{385}$.

Cell culture

The human kidney proximal tubular cell line (HK-2) were obtained from Dr. Jer-Tsong Hsieh lab, UTSW. The cell line was cultured and maintained in Roswell Park Memorial Institute (RPMI) 1640 medium with 10% (v/v) fetal bovine serum and 1% (v/v) penicillin-streptomycin (PS) at 5% CO_2, 37 ^oC.

Cytotoxicity assay of $AuSG_{183}$, $AuSG_{211}$, $AuSG_{385}$

The human kidney proximal tubular cells (HK-2) were seeded in 96-well plates. The cells were allowed to adhere and grow for 36-48 h before $AuSG_{183}$/$AuSG_{211}$/$AuSG_{385}$ prepared in the culture medium was added into each well. After 6-h incubation at 37 ^oC, the solution containing particles was removed from each well completely followed by adding 0.5 mg/mL MTT in each well. After 3-h reaction with MTT, the solution was removed completely without disturbing the formed formazan at the bottom of the each well. 200 μL DMSO was added in each well to dissolve the formazan. The absorbance at 560 nm was further measured by a microplate reader to quantify the cell viability. The experiment was performed in triplicate.

Microscopic study on cell membrane binding of $AuSG_{183}$ and $AuSG_{385}$ experiment

The HK-2 cells were seeded in the petri dishes with 14 mm glass coverslips and allowed to adhere and grow for 36-48 h. $AuSG_{183}$ and $AuSG_{385}$ in culture medium were incubated with cells at 37 ^oC, respectively. Then the particle solution was removed completely followed by thorough washing with biological buffered solution. Live cell imaging solution was used to cover the cells

during the entire imaging period. The setting of fluorescent filters for observing the binding activity of $AuSG_{183}$ and $AuSG_{385}$, respectively, were listed as following:

Table 4.1. Filter settings of fluorescence microscope for observing $AuSG_{183}$ and $AuSG_{385}$

	Excitation filter	Emission filter	Dichromic mirror
$AuSG_{183}$	480/40	700LP + 780LP	560
$AuSG_{385}$	420/40	600/32	500

The numbers describing the filters are "emission center/band width"
LP: Long-pass

Cell uptake study of $AuSG_{183}$ and $AuSG_{385}$

The HK-2 WT cells were seeded in 6-well plates and allowed to adhere and grow for 36-48 h. $AuSG_{183}$ and $AuSG_{385}$ were prepared in culture media containing same amount of Au atoms and incubated with cells at 37 ^{o}C (N = 4 for each particle). Then particle solution was collected completely from each well and waited for centrifugation to collect the detached cells. 0.25% EDTA-trypsin was added into each well to detach the cells. Culture medium was used to neutralize trypsin and the detached cells were collected thoroughly. The cell suspension from each well and the previously collected particle solution were centrifuged at 1,300 rpm for 2 min. The supernatant was discard and the cell pellets were redissolved in biological buffered solution. The cells in the particle solution was mixed with the main population. The same centrifuging and redissolving process was repeated on the cell suspension for two times to wash the cells completely before they were prepared for Au quantification.

Quantification of membrane binding of $AuSG_{183}$ and $AuSG_{385}$

The procedure was same as the cell uptake study except for the incubation time was 1h and temperature was at 4^{o}C (N = 4 for each particle).

Quantification of GSH-inhibited membrane binding of $AuSG_{183}$ and $AuSG_{385}$

The HK-2 cells were seeded in 6-well plates and allowed to adhere and grow for 36-48 h. 10 mM GSH in culture medium whose pH was adjusted to 7.4 by 1M NaOH was incubated with cells for 1h at 37 ^{o}C. $AuSG_{183}$ in culture media was added into each well after GSH solution was completely removed. The cells were harvested and washed in the same procedure as that in the cell uptake study. The control group was the cells that went through the same process except preincubating with just culture medium. N=4 for each group.

The experiment on $AuSG_{385}$ followed the same procedure. $AuSG_{385}$ was prepared containing the same Au amount as that of $AuSG_{183}$.

Probenecid-inhibited membrane binding as a positive control for $AuSG_{183}$

The procedure was the same as the quantification of GSH-inhibited membrane binding except for the cells were preincubating with 1mM probenecid instead of 10 mM GSH.

Apoptosis assay on HK-2 cells incubated with $AuSG_{183}$ and $AuSG_{385}$

The HK-2 cells were seeded in 6-well plates and allowed to adhere and grow for 36-48 h. $AuSG_{183}$ were prepared in culture media and incubated with cells for 6 h at 37 ^{o}C. Then the particle solution was discarded and cells were harvested and washed in cold phosphate-buffered saline (PBS). The cells were centrifuged down and resuspended in 1X annexin-binding buffer and incubated with Alexa Fluor 488 annexin V and propidium iodide for 15 min before analyzed by flow cytometry. The study on GSH inhibition was conducted by preincubating the cells with 10 mM GSH before adding particles. 10,000-50,000 (SSC-W vs. SSC-A)-gated events per sample were collected using

a BD LSRFortessa™ flow cytometer. Fluorescence of Alexa Fluor 488 annexin V was detected using a 488 nm laser for excitation and emission was measured with 515/20 nm band-pass filter. Propidium iodide fluorescence was detected using a 561 nm laser for excitation and emission was measured with 610/20 nm band-pass filter. Raw data was processed and analyzed using FlowJo® software. The apoptosis assay was conducted with the same procedure as that of $AuSG_{183}$ except that the incubation time was 7 h.

4.3 Results and discussion

4.3.1 Cytotoxicity induced by $AuSG_{385}$ and $AuSG_{183}$

To explore the ligand-density effect on the NP-cell interactions *in vitro* without introducing other factors, we chose to use our previously reported two renal clearable glutathione-coated gold nanoparticles (GS-AuNPs) as they are with the same core size, same surface coating but different ligand densities. Based on the elemental analysis, the chemical formulas of the two GS-AuNPs are $AuSG_{385}$ and $AuSG_{183}$, respectively. Other characterizations of $AuSG_{385}$ and $AuSG_{183}$ are listed in Table 4.2.[9]

Table 4.2. Characterization of $AuSG_{183}$ and $AuSG_{385}$

	$AuSG_{183}$	$AuSG_{385}$
Core size	2.5 ± 0.3 nm	2.6 ± 0.3 nm
Hydrodynamic diameter (HD)	3.05 ± 0.78 nm	3.52 ± 0.70
Zeta potential	-40.63 ± 0.62 mV	$-38.53.7 \pm 0.48$ mV
Excitation/Emission center	350/810 nm	396/600 nm

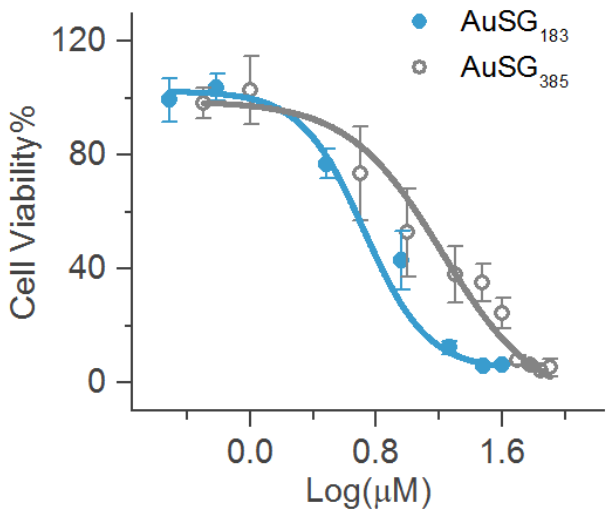

Figure 4.1. Cell viability after 6-h incubation with $AuSG_{385}$ and $AuSG_{183}$, respectively, determined by MTT assay.

We first assessed the cytotoxicity of $AuSG_{183}$ and $AuSG_{385}$ on human proximal tubular (HK-2) cells using MTT assay whose working mechanism lies on the proportional relationship between the amount of formazan, the reduced product of MTT by mitochondrial reductase, and the number of live cells. The half maximal inhibitory concentration (IC_{50}) was quantified and used to compare the cytotoxicity. The results suggested $AuSG_{183}$ induced higher cytotoxicity than $AuSG_{385}$ after 6-h incubation. The IC_{50} values of $AuSG_{183}$ was 5.26 ± 1.64 μM, only one-third of that of $AuSG_{385}$ (15.70 ± 0.71 μM) (Figure 4.1). This gap was considered significant as the core size and surface chemistry, two critical factors in nanostructure-generated cytotoxicity, were kept identical in the two particles. We hypothesized this difference was a possible reflection of two distinct cell death manners induced by $AuSG_{183}$ and $AuSG_{385}$, respectively.

4.3.2 Cell death pathways induced by $AuSG_{385}$ and $AuSG_{183}$

To test this hypothesis, we conducted the apoptosis assay on HK-2 cells incubated with $AuSG_{385}$ and $AuSG_{183}$, respectively. The assay works by detecting the fluorescent signals from two labelling agents, propidium iodide (PI) and Alexa-fluor Annexin V (AF), to identify the cell populations since normal, apoptotic and necrotic cells are labelled differently. PI is a non-permeable, DNA staining dye that only labels necrotic cells whose membrane integrity is lost; AF binds to phosphatidylserine (PS), an apoptotic marker on the inner layer of cell membrane that is only exposed to outer environment in early apoptotic and late apoptotic/necrotic cells. Therefore, normal cells would hardly give either signal, early apoptotic cells exhibit intense AF output and necrotic populations give signals from both PI and AF.[10]

Based on the working theory of the apoptosis assay, signal of cells measured by flow cytometer suggested that $AuSG_{183}$ directly caused cell necrosis while $AuSG_{385}$ activated the apoptosis pathway of HK-2 cells. Further analysis on the cell populations generated by $AuSG_{183}$ suggested the emergence of a unique group of cells characterized by high PI but low AF signals, whose profile could not be described as either necrotic or apoptotic population (Figure 4.2A). The exclusive PI penetration implied the membrane integrity of cells was probably compromised during $AuSG_{183}$ incubation. Moreover, the size of this unique population grew as the $AuSG_{183}$ concentration increased manifesting a concentration-dependent behavior (Figure 4.2B). These phenomena raised the assumption that there was possibly mechanical pressure imposed by $AuSG_{183}$ on the cell membrane which caused membrane leakage and the force became more intense as the particle concentration increased.

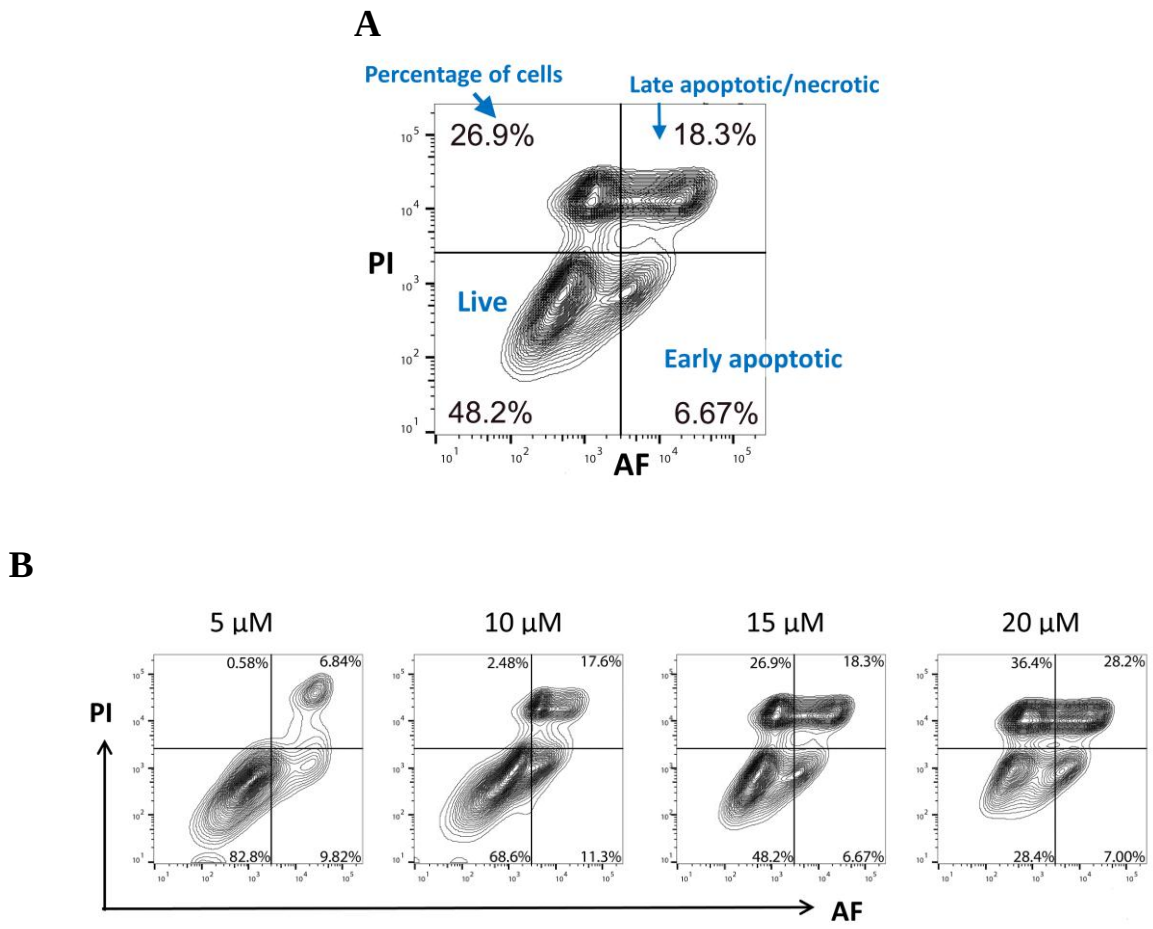

Figure 4.2. A) Cell populations characterized by apoptosis assay after incubating with $AuSG_{183}$. The cell population appeared in the first quadrant could not be described by the apoptosis assay B) Concentration-dependent emergence and growth of the cell population in the first quadrant.

In contrast, the cells incubated with $AuSG_{385}$ exhibited typical apoptotic characters. Noticeable early apoptotic cell group tightly bridged normal and necrotic populations demonstrating the apoptosis pathway. A portion of necrotic cells appeared in the very right of first quadrant suggesting they might share similar characters with the unique cell group created by $AuSG_{183}$, however, it could not be defined as an independent population as it heavily fused in the necrotic group (Figure 4.3). Therefore, compared to $AuSG_{183}$, $AuSG_{385}$ had a possibly weak tendency to

physically interact with the plasma membrane to induce extensive structural compromise, instead, altered the signaling pathway of the HK-2 cells.

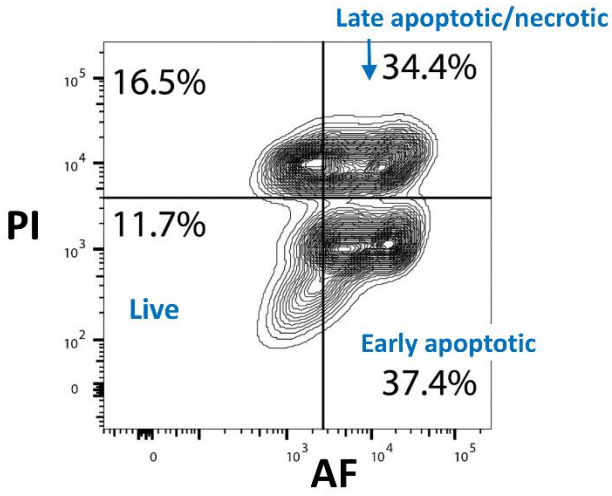

Figure 4.3. Cell populations characterized by apoptosis assay after incubation with $AuSG_{385}$

4.3.3 Compromise of membrane integrity of HK-2 cells induced by $AuSG_{183}$

The mechanical interplay between $AuSG_{183}$ and the cell membrane was further illuminated under fluorescence microscope. By taking advantage of the intrinsic near-infrared (NIR) emission of $AuSG_{183}$, we observed evident binding activity of $AuSG_{183}$ on the plasma membrane without fluorescent interference from the cells. In addition, intense PI signal from nuclei of some cells were also observed proving the enhanced membrane permeability after $AuSG_{183}$ treatment (Figure 4.4A&B). Due to the strong autofluorescence of the cells at 600 nm, signals from $AuSG_{385}$ was hard to detect using fluorescence-based techniques (Figure 4.4C). To compare the intenseness of binding activity between $AuSG_{183}$ and $AuSG_{385}$, we conducted quantitative analysis on number of bound particles based on gold amount using ICP-MS. The average number of $AuSG_{183}$ on the cell

membrane was measured to be approximately four-time of that of $AuSG_{385}$ suggesting much intense physical interaction imposed by $AuSG_{183}$ (Figure 4.4D).

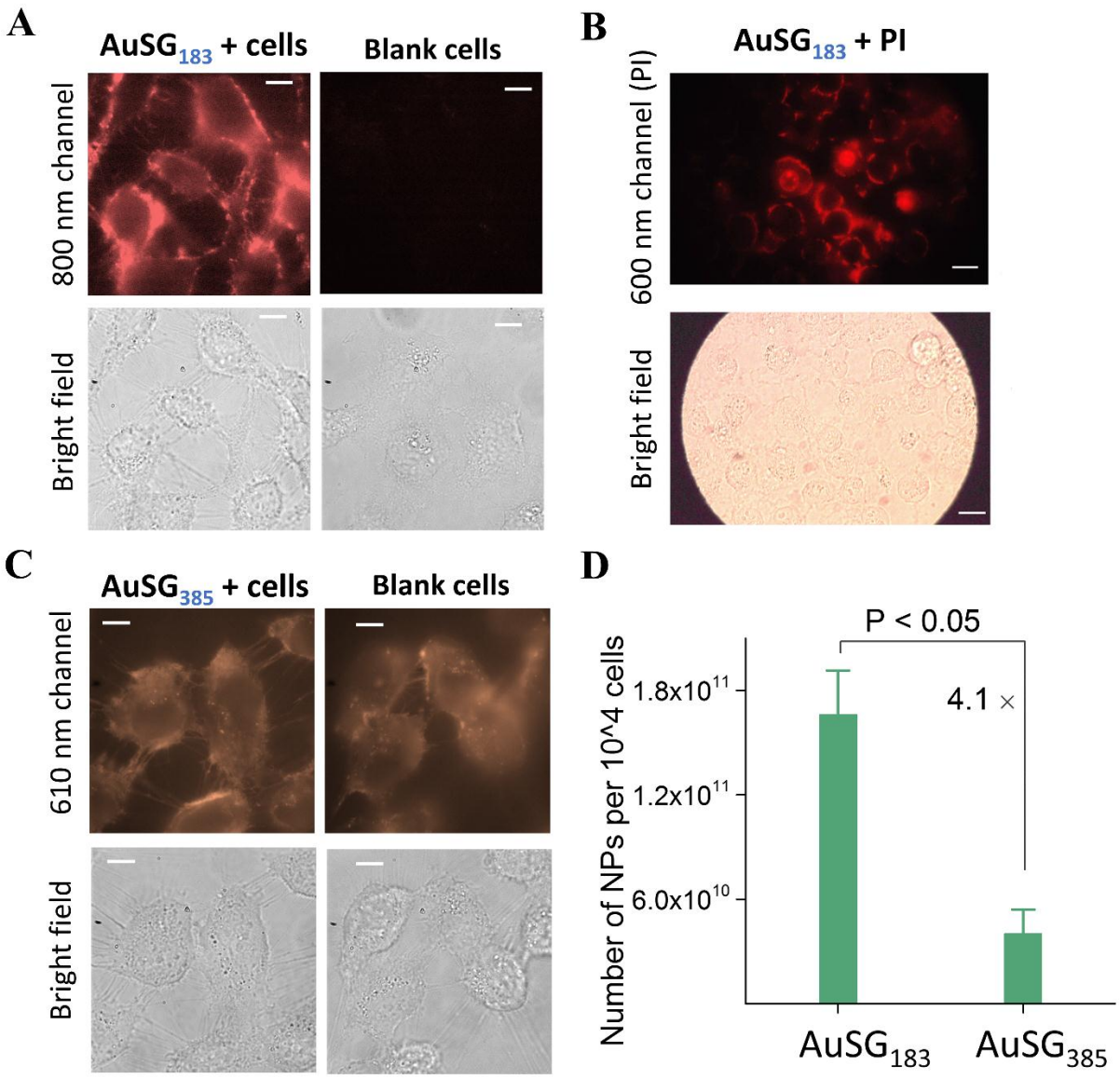

Figure 4.4. A) Binding activity of $AuSG_{183}$ to the plasma membrane of HK-2 cells illuminated under fluorescence microscope. B) PI stained HK-2 cells after $AuSG_{183}$ incubation showing PI penetrating into the nuclei of attached the cells. C) HK-2 cells illuminated at 600 nm after $AuSG_{385}$ incubation. D) Quantitative analysis of number of bound $AuSG_{183}$ and $AuSG_{385}$ on the plasma membrane of HK-2 cells, respectively, using ICP-MS. (Scale Bar in A and C is 10 μm, and in B is 20 μm)

To further understand the binding mechanism of $AuSG_{183}$, we incubated $AuSG_{183}$ with other cell lines and found out its membrane affinity was cell-line-specific (Figure 4.5). There was hardly signal detected after incubating $AuSG_{183}$ with MCF-7 cells or Hela cells. This specificity indicated the binding was probably mediated by surface GSH, of which the recognition and uptake process was dependent on cell types. According to the reported literatures, three transporters, organic anion transporter (OAT) 1 and 3 and sodium-dicarboxylate 2 exchanger (SDCT2), which are expressed on the basement membrane of renal proximal tubular cells are highly active in GSH uptake[11], while rare literatures reported their expression in cancer cell lines such as Hela and MCF-7. Therefore, it was possible the high binding affinity of $AuSG_{183}$ was a result of intense interaction between surface GSH and its membrane transporters on HK-2 cells.

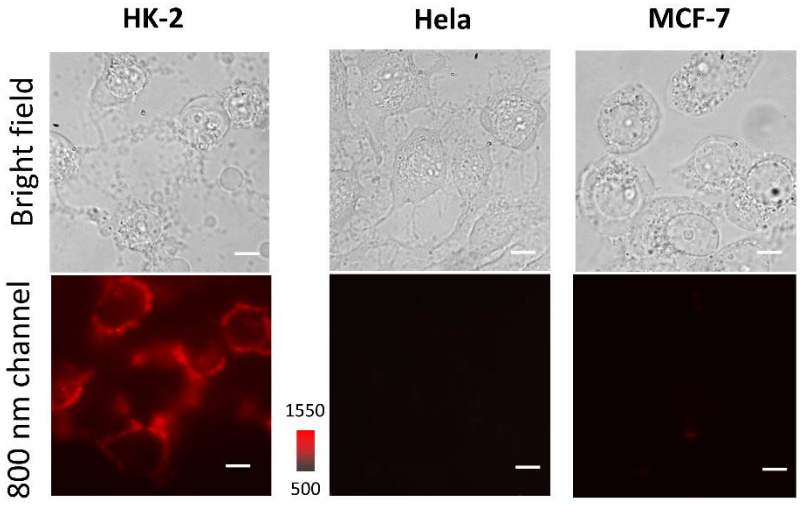

Figure 4.5. Binding activity of $AuSG_{183}$ to plasma membrane of HK-2, Hela and MCF-7 Cell lines, respectively, illuminated by the 810 nm emission of $AuSG_{183}$. Scare bar = 10 μm

4.3.4 Inhibition effect of glutathione (GSH) in membrane binding of $AuSG_{183}$

To test the role played by GSH in the physical attaching of $AuSG_{183}$ on the plasma membrane, we conducted a "block experiment" by pre-incubating free GSH molecules with the cells before adding

$AuSG_{183}$. The bound gold amount on the plasma membrane was reduced by 62% under this circumstance, suggesting the binding was indeed mediated by the surface GSH. A positive control using probenecid, a classic OAT inhibiting drug[11], was also tested and the measured bound $AuSG_{183}$ on HK-2 cells after probenecid inhibition was reduced by 23%, confirming that recognition between GSH and OATs were responsible for the binding activity of $AuSG_{183}$ (Figure 4.6A). The relatively weak inhibitory effect of probenecid compared to GSH was probably because there were multiple pathways involved in the uptake of GSH. Moreover, the "blocking" of GSH significantly reduced the incidents of enhanced membrane permeability. The unique cell population reflected by the apoptosis assays was considerably scaled down by over 90% (Figure 4.6B). This further confirmed our hypothesis that loss of the membrane integrity was a consequence of physical binding of $AuSG_{183}$. It was also noted that the unique population emerged like an extended group of the necrotic population, especially when the concentration of $AuSG_{183}$ was relatively low. This implied a direct transition from membrane breakage to necrosis which is consistent to the common knowledge that passive membrane rupture induced by external stress such as physical damage, toxin-induced pore formation, infection etc. is one major cause of cell necrosis.[12]

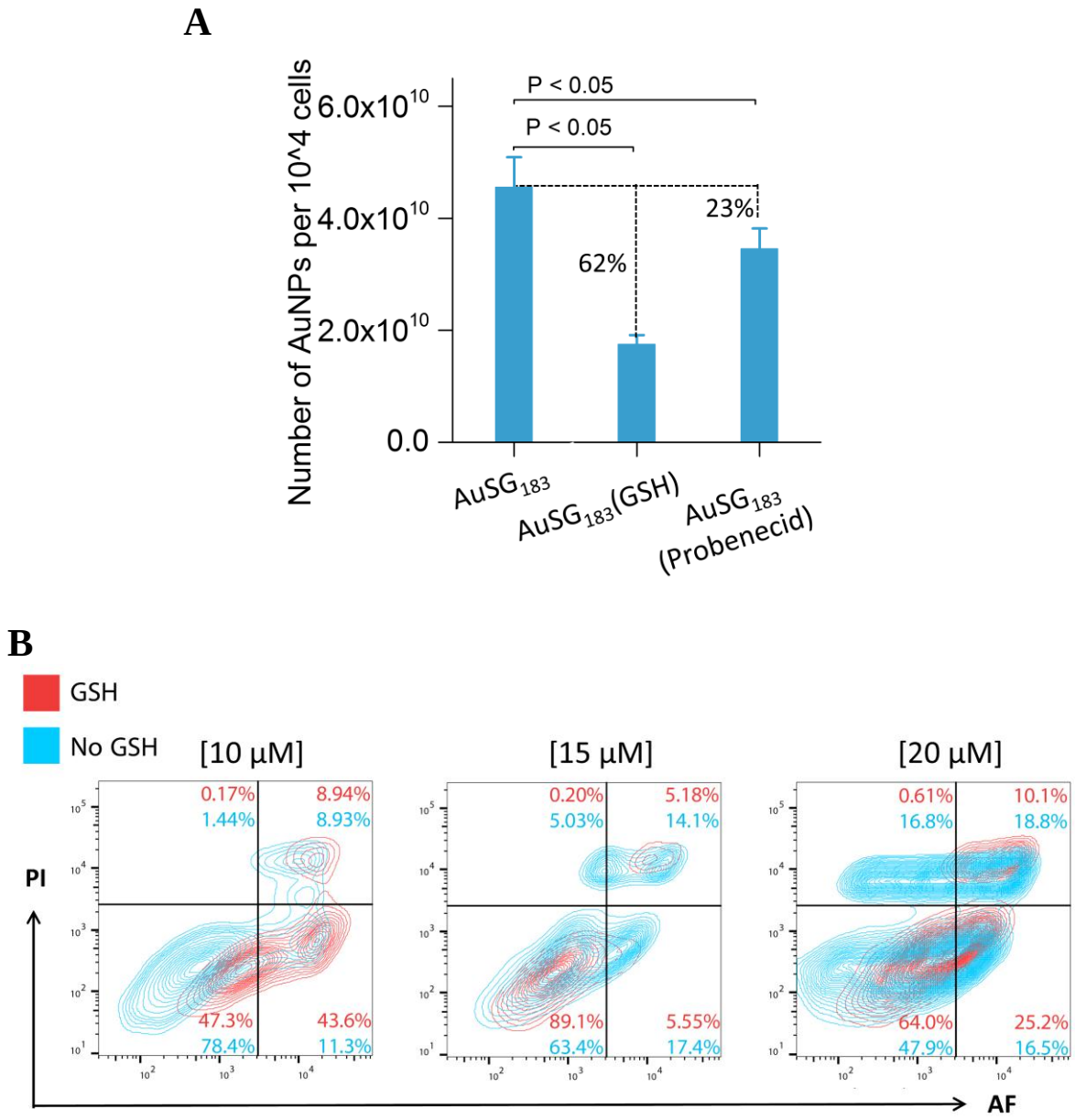

Figure 4.6. A) Number of bound $AuSG_{183}$ on the plasma membrane of HK-2 cells after preincubation of GSH and probenecid, respectively. B) Cell populations generated after incubating with a concentration series of $AuSG_{183}$ characterized by apoptosis assay with/ without preincubation with GSH.

On the other hand, GSH blocking hardly influenced on the binding of $AuSG_{385}$ on the plasma membrane. The number of bound particles was comparable with/without GSH preincubation

(Figure 4.7A). The percentage of cells in the first quadrant was reduced, however, they were hard to be defined from the necrotic group originally, leaving this quantitative change ambiguous. Most importantly, apoptotic characters of cells induced by $AuSG_{385}$ were still most pronounced and were not altered by GSH blocking (Figure 4.7B). These results indicated the physical stress on the membrane was not the major consequence induced by $AuSG_{385}$, herein, GSH blocking would not exert an inhibitory effect on the cellular interaction of $AuSG_{385}$. The contrasting GSH effect in the cell death pathways of $AuSG_{183}$ and $AuSG_{385}$ manifested that surface ligand density controlled the way that how GS-AuNPs communicated with the HK-2 cells that low ligand density tended to facilitate the physical interaction to the membrane while high ligand density exerted effect on molecular signaling pathway.

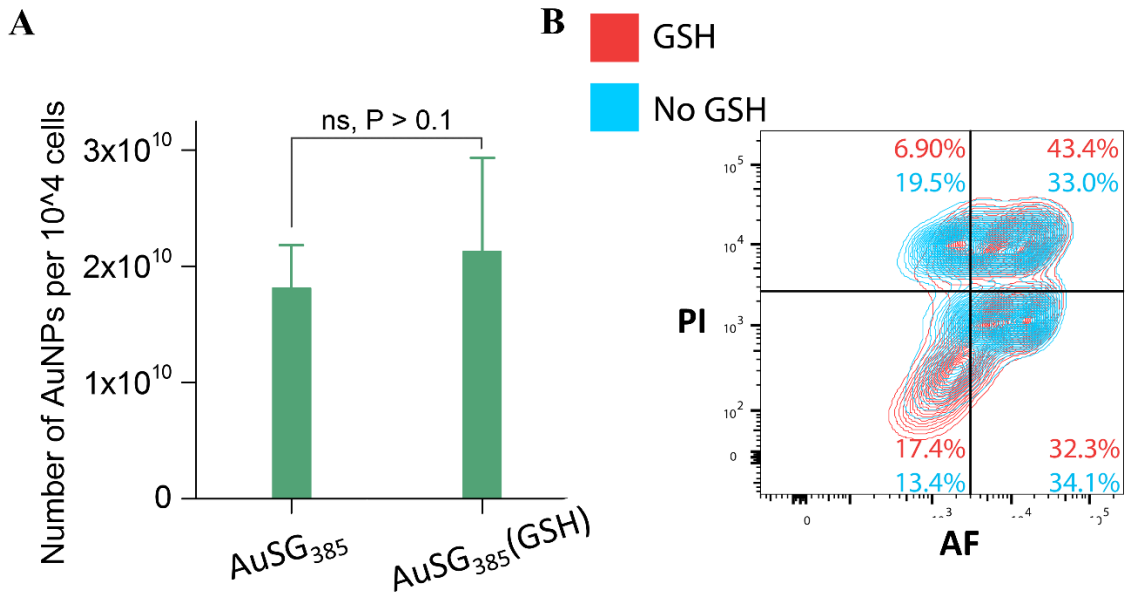

Figure 4.7. A) Number of bound $AuSG_{183}$ on the plasma membrane of HK-2 cells after preincubation of GSH. B) Cell populations generated after incubating with $AuSG_{385}$ characterized by apoptosis assay with/without preincubation with GSH.

4.3.5 Inhibition effect of glutathione (GSH) in cytotoxicity induced by GS-AuNPs

Furthermore, GSH inhibition exerted different role in the biocompatibility of HK2 cells to $AuSG_{183}$ and $AuSG_{385}$. A remarkable increase of cellular tolerance to $AuSG_{183}$ was achieved by GSH blocking reflected by escalated IC_{50} value from 5.26 ± 1.64 μM to 18.26 ± 1.29 μM (Figure 4.8A). This result also suggested our assumption on the causal relationship between membrane breakage and cell necrosis. The biocompatibility of $AuSG_{385}$ was slightly increased by 1.3-fold after GSH preincubation indicated by changed IC_{50} value from 16.47 ± 3.30 μM to 22.49 ± 2.07 μM (Figure 4.8C). This was attributed to weak GSH-mediated interaction. It was clear at this point that the effect of GSH in GS-AuNPs-induced cytotoxicity is dependent on the interaction manner between GS-AuNPs and plasma membrane which was related to the surface ligand density. Another GS-AuNPs, $AuSG_{211}$, whose ligand density fell in between was introduced as a control. The IC_{50} value of $AuSG_{211}$ was increased by 1.6-fold from 7.59 ± 3.02 μM to 12.29 ± 1.86 μM (Figure 4.8B). Therefore, the effect of GSH became more obvious as the surface ligand density decreased because the GSH-mediated physical interaction tended to happen more frequently as ligand density decreased.

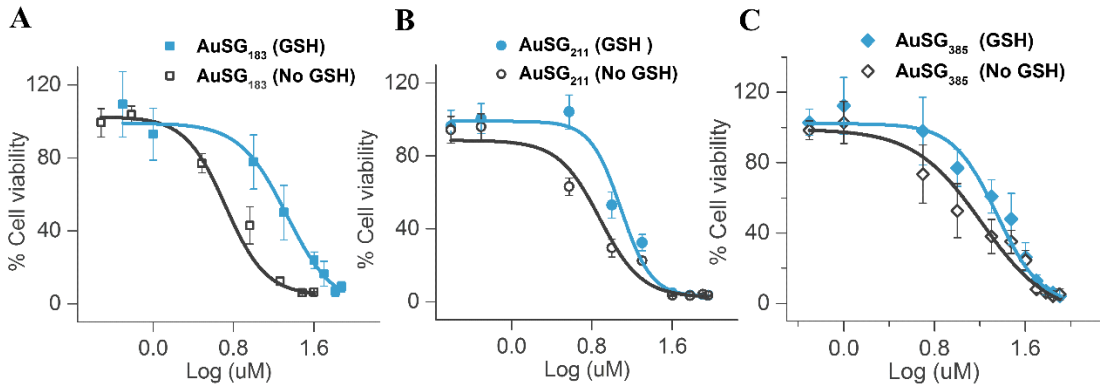

Figure 4.8. Cytotoxicity induced with/without GSH preincubation by $AuSG_{183}$ A) $AuSG_{211}$ B) and $AuSG_{385}$ C) after 6-h incubation quantified by MTT assay.

4.4 Conclusion

In summary, this study demonstrated the influence of surface ligand density in membrane binding affinity, cell death pathway and cytotoxicity of GS-AuNPs and constructed the complex relationship between these cellular interactions. Briefly, $AuSG_{183}$ exhibited high binding affinity to the plasma membrane of HK-2 cells which was proved mediated by surface glutathione. The binding activity induced loss of membrane integrity which further progressed into cell necrosis. Using free glutathione molecules as a "blocker" could reduce the binding affinity of $AuSG_{183}$ and further alleviate the membrane breakage. $AuSG_{385}$ was relatively inert to plasma membrane of HK-2 cells and somehow activated the apoptosis pathway. Surface glutathione was hardly involved in the interaction between $AuSG_{385}$ and HK-2 cells reflected by the rare "block" effect of free glutathione molecules. These results indicated that the difference in surface ligand density can induce dramatic change in the communication style between renal clearable inorganic NPs and renal cells. This might be attributed to the distinct ligand geometries at high and low density which make the ligands approach the cell membrane in different ways. Overall, this report unraveled the high sensitivity of biological system to nanostructure and offered a new strategy to develop low-toxic renal clearable inorganic nanomedicine.

4.5 Acknowledgements

This work was supported by the NIH (1R01DK103363) and a start-up fund from The University of Texas at Dallas.

4.6 Authors Contributions

Jing Xu, Linxi Shi and Chance Nowak conducted the *in vitro* experiments. Xuhui Ning synthesized the GS-AuNPs. Yingyu Huang measured the zeta potential of GS-AuNPs. Jing Xu, Linxi Shi, Chance Nowak, Mengxiao Yu, Jie Zheng and Leonidas Bleris reviewed, analyzed and interpreted the data.

4.7 References

[1] a) A. Albanese, P. S. Tang, W. C. W. Chan, *Annual Review of Biomedical Engineering* **2012**, *14*, 1-16; b) M. A. Gatoo, S. Naseem, M. Y. Arfat, A. Mahmood Dar, K. Qasim, S. Zubair, *BioMed Research International* **2014**, *2014*, 8.

[2] B. D. Chithrani, A. A. Ghazani, W. C. W. Chan, *Nano Letters* **2006**, *6*, 662-668.

[3] S. E. A. Gratton, P. A. Ropp, P. D. Pohlhaus, J. C. Luft, V. J. Madden, M. E. Napier, J. M. DeSimone, *Proceedings of the National Academy of Sciences* **2008**, *105*, 11613-11618.

[4] M. Ahamed, M. Karns, M. Goodson, J. Rowe, S. M. Hussain, J. J. Schlager, Y. Hong, *Toxicology and Applied Pharmacology* **2008**, *233*, 404-410.

[5] H. Lee, T. W. Odom, *Nanomedicine* **2015**, *10*, 177-180.

[6] a) A. Bandyopadhyay, R. L. Fine, S. Demento, L. K. Bockenstedt, T. M. Fahmy, *Biomaterials* **2011**, *32*, 3094-3105; b) H. Lee, A. K. R. Lytton-Jean, Y. Chen, K. T. Love, A. I. Park, E. D. Karagiannis, A. Sehgal, W. Querbes, C. S. Zurenko, M. Jayaraman, C. G. Peng, K. Charisse, A. Borodovsky, M. Manoharan, J. S. Donahoe, J. Truelove, M. Nahrendorf, R. Langer, D. G. Anderson, *Nature Nanotechnology* **2012**, *7*, 389; c) E. Phillips, O. Penate-Medina, P. B. Zanzonico, R. D. Carvajal, P. Mohan, Y. Ye, J. Humm, M. Gönen, H. Kalaigian, H. Schöder, H. W. Strauss, S. M. Larson, U. Wiesner, M. S. Bradbury, *Science Translational Medicine* **2014**, *6*, 260ra149-260ra149; d) H. Yuan, S. Zhang, *Applied Physics Letters* **2010**, *96*, 033704.

[7] D. R. Elias, A. Poloukhtine, V. Popik, A. Tsourkas, *Nanomedicine: Nanotechnology, Biology and Medicine* **2013**, *9*, 194-201.

[8] E. Moradi, D. Vllasaliu, M. Garnett, F. Falcone, S. Stolnik, *RSC Advances* **2012**, *2*, 3025-3033.

[9] J. Liu, P. N. Duchesne, M. Yu, X. Jiang, X. Ning, R. D. Vinluan, P. Zhang, J. Zheng, *Angewandte Chemie International Edition* **2016,** *55*, 8894-8898.

[10] v. E. Manon, L. J. Nieland, F. C. Ramaekers, B. Schutte, C. P. Reutelingsperger, *Cytometry* **1998**, *31*, 1-9.

[11] L. H. Lash, *Toxicology and Applied Pharmacology* **2005**, *204*, 329-342.

[12] S. L. Fink, B. T. Cookson, *Infection and Immunity* **2005**, *73*, 1907-1916.

CHAPTER 5

SUMMARY AND PERSPECTIVES

5.1 Summary

Starting from 2007, tremendous efforts have been devoted into developing renal clearable inorganic NPs to resolve the elimination issue of conventional inorganic nanomedicine. So far, plenty of renal clearable inorganic nanoparticles (NPs) have been created with remarkable biomedical potentials and efficient renal clearance. To further advance them into clinic translation, investigations on biointeractions of these NPs in the kidneys have been conducted. In this dissertation, we have presented our findings regarding this topic using renal clearable glutathione-coated gold NPs (GS-AuNPs) as a model. Our research aspects are transport behaviour, biocompatibility and NP-cell interactions of GS-AuNPs in the kidneys.

Owing to the high X-ray attenuation efficiency of gold atoms, we achieved to illuminate the transport process of GS-AuNPs in the kidney components using X-ray imaging. We observed that under normal condition GS-AuNPs were uninterruptedly transported from renal cortex, medulla to pelvis and eventually into ureter and bladder. In contrast, ureter-ligation induced nephropathy caused selective deposition of GS-AuNPs at the interface of medulla and pelvis where the injury of renal tubules occurred extensively. Our study on dose-dependencies and biocompatibility of GS-AuNPs unravelled the relationship among injection dose, blood transport and renal clearance efficiency. As dose increased, GS-AuNPs tended to retain in the blood flow more than extravasate into interstitial space which escalated the blood concentration and accelerated the renal clearance. The increased renal clearance reduced the exposure of the kidneys to GS-AuNPs leading to high biocompatibility. We also investigated the interactions between GS-AuNPs and renal cells *in vitro*

and found out the surface ligand density determined the communication style between GS-AuNPs and human kidney proximal tubular (HK-2) cells. GS-AuNPs with low ligand density exhibited high binding affinity to plasma membrane of HK-2 cells and caused cell necrosis while GS-AuNPs with high ligand density showed weak binding activity and activated the apoptosis pathway.

These findings have advanced our fundamental understanding on the biological fate of renal clearable GS-AuNPs and made it possible for us to precisely control its biointeractions in the future to fulfil the clinic requirements.

5.2 Perspectives

5.2.1 Transport and NP-cell interactions of GS-AuNPs in nephropathic kidneys

It was illustrated in Chapter 2 that unilateral ureteral obstruction (UUO) models displayed selective deposition of GS-AuNPs at the interface of renal medulla and pelvis. As the injury progressed, uptake of GS-AuNPs by the local tubular cells was also spotted. These observations indicate the altered transport process of clearable inorganic NPs and potential local injury could occur in diseased kidneys, which is particularly critical for clinical translation. Therefore, one future focus should be on investigating the transport of renal clearable inorganic NPs in the nephropathic kidneys. Compared to the UUO model, which is constructed by surgery operation, congenital or drug-induced disease models are preferred since they are closer to clinical cases. The transport study would probably provide insight on the tissue distribution of NPs, where NP-cell interactions, especially at pathological site, are important to explore.

5.2.2 Other factors in the clearance efficiency of GS-AuNPs

Clearance efficiency is closely related to the concentration of GS-AuNPs in blood and in kidneys which influence their biomedical applications such as cancer targeting and kidney functional imaging. As was discussed in Chapter 1, clearance efficiency is sensitive to multiple factors such as physicochemical properties (core density and size) and injection dose. These factors either alter the blood transport behavior of the NPs or induce interactions between NPs and the glomerulus. To maximize the biological potential, clearance efficiency of GS-AuNPs needs to be precisely controlled, which demands future efforts on investigating the effect of other factors, such as surface chemistry and surface charge of the NPs, in the blood transport and interactions with renal cells. Previously, we have observed that renal clearable PEG_{1000}-coated AuNPs (PEG-AuNPs) were gradually cleared out from the kidneys in contrast to rapid excretion of GS-AuNPs. This slow clearance resulted in high blood concentration and significant tumor targeting efficiency of PEG-AuNPs.[1] However, based on our observation on dose effect in renal clearance of GS-AuNPs, high blood concentration is paired with rapid and large renal clearance efficiency. The paradoxical phenomenon indicates specific interactions between PEG-AuNPs and glomerulus may occur. Since PEG-AuNPs demonstrated potential as a renal clearable nanomedicine for cancer therapy, fundamental understanding the NP-cell interaction in the kidneys is critical in its future application. It was discussed in Chapter 1 that anionic ultrasmall quantum dots are captured by mesangial cells with traceable amount being filtered while its cationic counterparts are rapidly passed into urine.[2] This work describes an extreme case of surface charge effect in renal clearance of inorganic NPs which makes us wonder if there exists a negative-charge threshold for a NP to be renal clearable and if the renal clearance efficiency is charge-dependent. Besides, the observation that anionic

quantum dots were taken by a specific group of renal cells inspires future study on the charge effect on cellular recognition of GS-AuNPs.

5.2.3 Reabsorption and secretion process of GS-AuNPs

Our previously reported work and Chapter 2 in this dissertation have validated the potential of GS-AuNPs as a contrast agent for both fluorescent and X-ray kidney functional imaging. Fundamentally, it is the filtration kinetics of GS-AuNPs under normal and pathological condition that are correlated with the actual kidney function. However, whether GS-AuNPs is involved in the other two processes of renal physiology, reabsorption and secretion, is unknown. Reabsorption and secretion happen at tubular epithelial cells and are generally referred as tubular transport of solutes in renal filtrates. Both processes rely on endocytic machinery in contrast to passive glomerular filtration. Basically, the filtered nutritional substances and vital ions are transported back to plasma through reabsorption; certain waste products and drug molecules are secreted from plasma into urine.[3] Reabsorption and secretion of a contrast agent would influence its blood concentration and circulation time which are related to its long-term biosafety. The approaches used to study reabsorption and secretion are limited and complicated. Micropuncturing the nephron and analyzing the filtrate collected at each tubular segment is the most reliable method, however, the technique requires specific training to master.[4] Though it seems hard to illustrate the reabsorption and secretion process of GS-AuNPs at this point, it should be considered as one of the future focuses since fully understanding mechanism of renal excretion process is critical to push GS-AuNPs into clinics eventually.

5.2.4 Renal therapy using GS-AuNPs

As the kidneys can excrete ~35-70% ID of GS-AuNPs within 2 h post intravenous injection, it would be favored if GS-AuNPs can be integrated with therapeutic function for treating nephropathy. Since the dominant renal excretion process of GS-AuNPs is glomerular filtration, GS-AuNPs might be suitable for coping with glomerulonephritis, especially the one induced by virus injection. By loading or conjugating antiviral drug molecules onto GS-AuNPs, the total amount of drug molecules delivered to glomerular area may be elevated due to massive filtration of GS-AuNPs. However, this goal could be accomplished provided the drug molecules would not induce significant size enlargement of GS-AuNPs in biological fluid. As illustrated in Chapter 4, membrane binding affinity of GS-AuNPs to proximal tubular cells can be tuned by the surface ligand density *in vitro*. If the same phenomenon occurs *in vivo*, targeting and delivering drug molecules to treat tubular abnormality may be achieved.

5.3 Conclusion

With great biomedical potential and high biocompatibility demonstrated, comprehensive understanding the transport and renal excretion process of GS-AuNPs have become the future directions, which would further facilitate us to precise control the biobehaviors of GS-AuNPs and expedite its clinical translation.

5.4 References

[1] J. Liu, M. Yu, X. Ning, C. Zhou, S. Yang, J. Zheng, *Angewandte Chemie International Edition* **2013**, *52*, 12572-12576

[2] X. Liang, H. Wang, Y. Zhu, R. Zhang, V. C. Cogger, X. Liu, Z. P. Xu, J. E. Grice, M. S. Roberts, *ACS Nano* **2016**, *10*, 387-395.

[3] C. Stanfield, *Principles of human physiology*, 12 ed., Pearson Higher Ed, **2012**.

[4] a) V. Vallon, *Pflugers Archiv : European journal of physiology* **2009**, *458*, 189-201; b) C. Zurth, *Invest Radiol* **1984**, *2*, 110-115.

BIOGRAPHICAL SKETCH

Jing Xu was born in Hohhot, Inner Mongolia, China. She received her BS in the Department of Pharmacy, China Pharmaceutical University, Nanjing, Jiangsu, China in 2011. She came to the US for her advanced education and joined the PhD program in Chemistry at The University of Texas at Dallas in fall 2013. She started her research on investigating nano-biointeractions of renal clearable gold nanoparticles under the supervision of Dr. Jie Zheng.

CURRICULUM VITAE

Jing Xu
Department of Chemistry and Biochemistry, NSERL 2.440,
The University of Texas at Dallas,
800 W Campbell Rd, Richardson, TX 75080
jxx131030@utdallas.edu

Education:

- **Ph.D. candidate in Chemistry**
  The University of Texas at Dallas, Richardson, Texas Aug 2013-Aug 2018
  Dissertation: Interactions of Renal Clearable Gold Nanoparticles with the Kidneys *In Vitro* and *In Vivo*
  Advisor: Prof. Jie Zheng
- **B. S. in Pharmaceutics**
  China Pharmaceutical University, Nanjing, China Sept 2007-Jun 2011

Teaching Experience:

- **Graduate Teaching Assistant** Aug 2013 – Dec 2017
  Department of Chemistry & Biochemistry, The University of Texas at Dallas

  Organic Chemistry Lab I Sept 2013 – Dec 2013
  - Prepared lab materials, delivered lectures on labs, instructed basic lab techniques, supervised and evaluated lab performance for 20-25 sophomore level undergraduates
  - Graded lab reports and exams and answered their questions during lab and office hour

  Physical Measurement Lab Jan 2014 – May 2014
  - Prepared lab materials, instructed instrument operation, worked with students one-on-one and evaluated lab performance for 15-20 junior or senior level undergraduates
  - Instructed on general writing and report writing, graded and commented on reports
  - Delivered a lecture on "Viscosity"

  Instrumental Analysis Lab Sept 2014 – May 2015/Sept 2017 – Dec 2017
  - Prepared lab materials, explained working theory of the involved instruments, instructed instrument operation, worked with students one-on-one and evaluated lab performance for 15-20 junior or senior level undergraduates
  - Instructed on data analysis and report writing, graded and commented on reports, discussed and answered students' questions during office hour
  - Delivered a lecture on "Fluorescence and its applications"

Research Experience:

Graduate Research Assistant
The University of Texas at Dallas Aug 2013 – Present

- Manage general supplies of lab; take charge of maintaining biohazard hood and cell incubator
- Mentor undergraduate students to develop their research interests, obtain lab skills and carry out independent projects

  Projects:
  In vivo X-ray imaging of transport of renal clearable gold nanoparticles (AuNPs) in kidneys
    - Synthesized, purified and characterized renal clearable AuNPs
    - Optimized the condition for *in vivo* small animal X-ray imaging and conducted *in vivo* kidney functional imaging under X-ray radiation
    - Analyzed kidney clearance kinetics to differentiate normal and compromised kidney function
    - *Ex vivo* tissue processing and staining for histological analysis

  Investigation on dose-dependencies and biocompatibility of renal clearable AuNPs
    - Measured renal clearance of AuNPs using inductively coupled plasma mass spectrometry (ICP-MS)
    - Evaluated biocompatibility of renal clearable AuNPs based on histological and biochemical analyses
    - Conducted transmission electron microscopic analysis to investigate the integrity of glomerular filtration membrane in kidneys after exposure to renal clearable AuNPs
    - Conducted pharmacokinetics measurement and analysis to unravel the plasma clearance behavior of renal clearable AuNPs

  Investigation on ligand-density-effect on transport of renal clearable AuNPs
    - Cultured and maintained kidney and cancer cell lines including HK-2, MDCK, NRK-52E, Hela and MCF-7
    - Evaluated cytotoxicity and measured cellular uptake of renal clearable AuNPs
    - Conducted fluorescence microscopic and transmission electron microscopic analyses on the binding affinity of AuNPs to cell membrane
    - Measured cellular uptake of renal clearable AuNPs using ICP-MS

Undergraduate Research Assistant
China Pharmaceutical University Aug 2009 – Jun 2011

- Conducted acylation of gelatin to avoid crosslinking and improve the stability of soft capsule

Publications:

1. **J. Xu**, L. Shi, C.M. Nowak, X. Ning, J. Zheng. "Ligand-density-effect on *In Vitro* Interactions of Renal Clearable Gold Nanoparticles with renal tubular cells" (*In preparation*)
2. **J. Xu**[+], M. Yu[+], C. Peng, P. Carter, J. Tian, X. Ning, Q. Zhou, Q. Tu, G. Zhang, A. Dao, X. Jiang, P. Kapur, J.-T. Hsieh, X. Zhao, P. Liu, J, Zheng. "Dose Dependencies and Biocompatibility of Renal Clearable Gold Nanoparticles", *Angew. Chem. Int. Ed*., 2018, 57, 266-271. ([+], these authors contributed equally) (Highlighted as **"VIP" paper** by *Angew. Chem. Int. Ed.*, and by *ChemViews Magazine, doi: 10.1002/chemv.20170010)*
3. **J. Xu**, M. Yu, P. Carter, E. Hernandez, A. Dang, P. Kapur, J.-T. Hsieh, J. Zheng. "*In Vivo* X-ray Imaging of Transport of Renal Clearable Gold Nanoparticles in the Kidneys", *Angew. Chem. Int. Ed*., 2017, 56, 13356-13360. (Highlighted as **"VIP" paper** by *Angew. Chem. Int. Ed.* and by *Nature Review Materials,* doi:10.1038/natrevmats.2017.69)
4. **J. Xu**, C. Peng, M. Yu, J. Zheng. "Renal Clearable Noble Metal Nanoparticles: Photoluminescence, Elimination, and Biomedical Applications." *WIREs Nanomed Nanobiotechnol.* 2017, 9, e1453. (Highlighted by *Advanced Science News* titled as *"Renal Clearable Noble Nanoparticles"* posted on January 28th, 2017)
5. X. Ning, C. Peng, E. S. Li, **J. Xu**, R.D. Vinluan, M. Yu, J. Zheng. "Physiological Stability and Renal Clearance of Ultrasmall Zwitterionic Gold Nanoparticles: Ligand Length Matters." *APL Mater.*, 2017, 5, 053406.
6. C. Peng, X. Gao, **J. Xu**, B. Du, X. Ning, S. Tang, R. M. Bachoo, M. Yu, W. P. Ge, J. Zheng "Targeting Orthotopic Gliomas with Renal-clearable Luminescent Gold Nanoparticles." *Nano Res.*, 2017, 4, 1366-1376
7. S. Tang, C. Peng, **J. Xu**, B. Du, Q. Wang, R. D. Vinluan, M. Yu, M. J. Kim, J. Zheng. "Tailoring Renal Clearance and Tumor Targeting of Ultrasmall Metal Nanoparticles with Particle Density." *Angew. Chem. Int. Ed.*, 2016, 55, 16039-16043 (Highlighted as **"VIP" paper** by *Angew. Chem. Int. Ed.)*
8. R. Vinluan, M. Yu, M. Gannaway, J. Sullins, **J. Xu**, J. Zheng. "Labeling monomeric insulin with renal clearable luminescent gold nanoparticles", *Bioconjug. Chem*, 2015, 26, 2435-2441.

Awards, Honors and Professional Membership:

American Chemical Society (ACS)	2017 – Present
ACS Division of Inorganic Chemistry Travel Award	2018
Research Small Grant	2018
Graduate Studies Scholarship, The University of Texas at Dallas	Aug 2013 – Present
People's Scholarship, China Pharmaceutical University	2007 – 2009